Probing nuclear density tails with antiprotons at PUMA: Detection and method

Untersuchung der Kerndichteperipherie mit Antiprotonen an PUMA: Detektion und Methodik
Zur Erlangung des Grades eines Doktors der Naturwissenschaften (Dr. rer. nat.)
Genehmigte Dissertation von Sabrina M. Zacarias aus Buenos Aires
Tag der Einreichung: Oktober 10, 2022, Tag der Prüfung: Oktober 26, 2022

1. Gutachten: Prof. Dr. Alexandre Obertelli
2. Gutachten: Prof. Dr. Wilfried Nörtershäuser
Darmstadt

TECHNISCHE UNIVERSITÄT DARMSTADT

Physics Department
Institut für Kernphysik
AG-Obertelli

Probing nuclear density tails with antiprotons at PUMA: Detection and method
Untersuchung der Kerndichteperipherie mit Antiprotonen an PUMA: Detektion und Methodik

Accepted doctoral thesis by Sabrina M. Zacarias

1. Review: Prof. Dr. Alexandre Obertelli
2. Review: Prof. Dr. Wilfried Nörtershäuser

Date of submission: Oktober 10, 2022
Date of thesis defense: Oktober 26, 2022

Darmstadt

Erklärungen laut Promotionsordnung

§8 Abs. 1 lit. c PromO

Ich versichere hiermit, dass die elektronische Version meiner Dissertation mit der schriftlichen Version übereinstimmt.

§8 Abs. 1 lit. d PromO

Ich versichere hiermit, dass zu einem vorherigen Zeitpunkt noch keine Promotion versucht wurde. In diesem Fall sind nähere Angaben über Zeitpunkt, Hochschule, Dissertationsthema und Ergebnis dieses Versuchs mitzuteilen.

§9 Abs. 1 PromO

Ich versichere hiermit, dass die vorliegende Dissertation selbstständig und nur unter Verwendung der angegebenen Quellen verfasst wurde.

§9 Abs. 2 PromO

Die Arbeit hat bisher noch nicht zu Prüfungszwecken gedient.

Darmstadt, Oktober 10, 2022

S. M. Zacarias

List of Figures

List of Tables

Abstract

Niederenergetische Antiprotonen können als Sonde verwendet werden, um den Protonen- und Neutronengehalt im Ausläufer der Kerndichteverteilung zu untersuchen. In Richtung der Neutronenabbruchkante ist dieser Bereich durch das Ausbilden von Neutronenhäuten und das Auftreten von Halos gekennzeichnet.

Bis heute gibt es keine Anlage, die eine Kollision von niederenergetischen Antiprotonen mit radioaktiven Kernen ermöglicht. Am CERN (Schweiz) gibt es jedoch sowohl eine Anlage zur Erzeugung radioaktiver Ionenstrahlen (ISOLDE) als auch eine Anlage für die Produktion von Antiprotonen (die Antimatter Factory), die die Voraussetzungen für die Erzeugung dieser Wechselwirkungen schaffen.

Das AntiProton Unstable Matter Annihilation Experiment (PUMA) zielt darauf ab, 10^9 Antiprotonen von der Antimatter Factory zu ISOLDE zu transportieren, um den Ausläufer der Kerndichteverteilung zu untersuchen, indem das Neutronen-zu-Protonen-Annihilationsverhältnis von sowohl stabilen als auch kurzlebigen Kernen gemessen wird. In dieser Arbeit wird die Entwicklung der Zeitprojektionskammer (Time Projection Chamber, TPC), der Hauptdetektionskomponente der geladenen Annihilationsprodukte, vorgestellt. Da der Detektor in die Öffnung des 4 T Magneten von PUMA eingesetzt werden soll, ist ein kompaktes und wartungsarmes Gerät erforderlich. Das geometrische Design basierte auf Monte-Carlo-Simulationen, die für die Detektionseffizienz und die Ladungsidentifikation optimiert wurden. Das elektrische Design wurde ebenfalls optimiert, um ein homogenes elektrisches Feld in der Driftregion des Detektors zu erzeugen. Abschließend wurde das mechanische Design entwickelt.

Die Empfindlichkeit der bei PUMA verwendeten Methode wird mit einem Atomkaskadencode untersucht, der auf antiprotonische Zinn- und Kalziumatome angewendet wird, um die Auswirkungen der unbekannten Einfangzustände zu untersuchen. Der Vergleich und die Validierung mit Röntgendaten liefern eine erste Schätzung der Einfangparameter, und die Kaskadenberechnungen zeigen, dass 70% der Annihilationen in den zirkulären Zuständen ($n, l = n - 1$) stattfinden, was das PUMA-Konzept bestätigt. Die Empfindlichkeit in Abhängigkeit der Isotopen des durch die Messung erhaltenen Annihilationsbreitenverhältnisses wird quantifiziert. Zusätzliche theoretische Entwicklungen, die den vollständigen Einfang und die Kaskade beschreiben, sind erforderlich, um die Auswirkungen von Annihilationen mit Antiprotonen, die einen niedrigem Drehimpuls besitzen, zu berücksichtigen. Diese haben sich hier als nicht vernachlässigbar erwiesen.

Abstract

Low-energy antiprotons can be used as a probe to study the proton and neutron content of the nuclear density tail. Towards the neutron drip line, this region is characterized by the development of neutron skins and the emergence of halos.

As of today, there is no facility that can provide a low-energy antiproton-radioactive ion collider. At CERN (Switzerland), however, the existence of both a Radioactive Ion Beam facility (ISOLDE) and a facility to produce antiprotons (the Antimatter Factory) provides a feasible ground to generate these interactions.

The antiProton Unstable Matter Annihilation experiment (PUMA) aims at transporting 10^9 antiprotons from the Antimatter Factory to ISOLDE to study the nuclear density tail by measuring the neutron-to-proton annihilation ratio of both stable and short-lived nuclei.

In this work, the development of the Time Projection Chamber (TPC), main detection component of the charged annihilation products, is presented. As the detector aims at being inserted into the bore of the 4 T solenoid of PUMA, a compact and low-maintenance device is required. The geometrical design was based on Monte-Carlo simulations optimized for detection efficiency and charge identification. The electrical design was also optimized to provide an homogeneous electric field in the drift region of the detector. Finally, the mechanical design was performed.

The sensitivity of the method used at PUMA is investigated with an atomic cascade code applied to antiprotonic tin and calcium atoms to study the impact of the unknown capture states. Benchmarks of the code with X-ray data provide an initial estimation of the capture parameters and the cascade calculations show that 70% of the annihilations occur at the circular states ($n, l = n-1$), validating the PUMA concept. The isotopic sensitivity of the annihilation width ratio obtained from the measurement is quantified. Additional theoretical developments that describe the full capture and cascade are needed to account for the impact of low-l annihilations which are here observed to be non-negligible.

Acknowledgements

Words could never suffice to properly acknowledge the large amount of people that contributed in one way or another to the culmination of this thesis, but here is an -inherently deficient- attempt.

First and foremost, I would like to warmly thank the PhD committee: Prof. Dr. Alexandre Obertelli, Prof. Dr. Wilfried Nörtershäuser, Prof. Dr. Robert Roth and Prof. Dr. Marco Durante for agreeing to be the examiners of this defence.

I would like to thank Prof. Dr. Alexandre Obertelli for his trust, guidance and constant support. Working under his supervision has been a true joy in both scientific and human levels. Merci pour le voyage à *Ithaque*.

I am grateful to the mastermind behind the detector, Lolly Pollacco. The person who can foresee a thousand problems and a thousand and one solutions. Having a close working relationship from a long distance is challenging but he kept up to the task stoically and with nothing but great patience and kindness.

I would also like to thank the invisible hand that puts out the little and massive fires everywhere, Frank Wienholtz. To Ella Wienholtz, as well, for challenging my german skills and keeping me humble.

The testing and commissioning of the detector will be in the hands of Clara Clink, to whom I would like to thank for taking over, and to both her and Christina Xanthopoulou for their support when I was overwhelmed with the writing of this manuscript.

Coming to the institute every day has been a pleasure due to the exceptional working environment provided by my colleagues. I would like to thank the AG-Obertelli present and former members for that, and in particular to the PUMA team on-site for the interesting exchanges and nice discussions: Alexander Schmidt, Jonas Fischer, Moritz Schlaich, Clara Klink, Christina Xanthopoulou and Frank Wienholtz. Special mention to my office-mate Simone Velardita, who contributed significantly to the fantastic working atmosphere and who would spill out the solution of all the LaTex bugs faster than Google.

I would like to thank Axel Frotscher, Hongna Liu, Yelei Sun and Yuki Kubota who shared many valuable resources at the beginning of my thesis that stayed with me until this day.

My family has shown nothing but full support despite the distance, and I deeply appreciate their trust and encouragement.

I am grateful to Rodrigo, for showing me the way every day since we met.

Thank you Alexandre, Lolly, Simone, Moritz, Alexander and Clara for proofreading my manuscript and your thoughtful and accurate comments that greatly improved the quality of this work.

Contents

1. Introduction and Motivation

1.1. The Size of the Nucleus

One could consider the beginning of the nuclear physics era with the experiment of E. Rutherford in 1911, in which he discovered that the atom was in fact composed of a positively charged nucleus surrounded by a negatively charged cloud of electrons [1]. A few years later, using similar scattering techniques with α particles, he identified a new particle emerging from the interactions, marking the discovery of the *proton* [2]. It was twenty years later, in 1932, that J. Chadwick discovered the existence of neutrons by shooting α particles in a beryllium target in which the emitted neutrons would collide and scatter protons from a paraffin block, subsequently detected in a ionisation chamber [3].

Since then, multiple experimental and theoretical efforts have been devoted to fully describe the nuclear structure. Electron scattering experiments, for instance, have offered a detailed description of the charge radii and charge distribution of stable nuclei [4, 5]. The density profile observed in various experiments indicates that there is a proportionality between the mass number A and the radius. This suggests that the nucleus has a constant *saturation* density, deduced to be $n_0 \sim 0.16$ fm^{-3}, regardless of its mass number. An example of this trend is shown in Fig. 1.1, which displays the charge density profile ρ_c of different stable isotopes across the nuclear chart. These profiles can be described to a good approximation by the two-parameter Fermi distribution, given by

$$\rho_c(r) = \frac{\rho_0}{1 + \exp(r - a)/c}, \tag{1.1}$$

where a is the half-density radius, c is the diffuseness parameter and ρ_0 is a normalisation constant. This evidence suggested that the nuclear force should be attractive at a short range, be stronger than the Coulomb repulsion among protons and have a repulsive core.

Similar evidence has been found when studying the neutron density profile of stable isotopes, although the measurements are generally hindered by uncertainties related to the hadronic reaction mechanisms (see Sec. 1.2) or low cross sections. Accordingly, the available data indicates that protons and neutrons are, in principle, uniformly distributed within the nucleus, as shown schematically on the lower side of Fig. 1.2. At the top side of the figure, the schematic neutron and proton potential wells are displayed, where the horizontal dashed line corresponds to the Fermi energy of the nucleons. The electromagnetic repulsion produces a shallower well for the protons with respect to that of the neutrons. Additionally, the β stability of the nucleus favours the occupation of the same Fermi levels in both potential wells. Assuming that the nuclear potential has a finite slope, one can deduce from these effects that the proton density lies within the neutron profile, shown on the lower side of Fig. 1.2 [7].

In light stable nuclei (Z$\lesssim$ 20), the neutron to proton ratio is roughly one. However, as the nuclear mass increases, the stability is obtained in nuclei containing larger amounts of neutrons. In Fig. 1.3, the nuclear chart displays the nuclei's half-lives, where the stable nuclei are shown in black and the line of Z=N nuclei is shown as reference.

From this figure, it is evident that the vast majority of known isotopes are neutron-rich and that most are not stable: there is rather an increasing instability towards the neutron and proton drip lines. Here, the measurements of proton and neutron density profiles is scarce in comparison due to

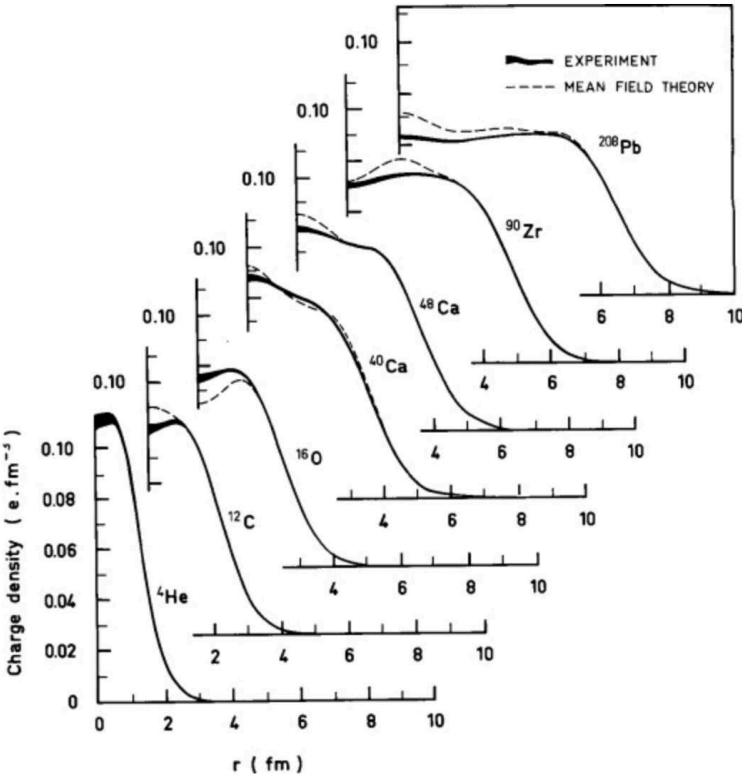

Figure 1.1.: Charge density distribution of a few stable isotopes, ranging from A=4 to A=208. This figure is reprinted with permission from [6] ©2022 by Springer Nature.

the technological challenges of studying short-lived nuclei. Nevertheless, data shows that the nuclear structure in this region displays unique features largely unexplored. As such, the rest of this chapter is devoted to explaining the physical background and existing techniques to tackle the proton and neutron densities at the edge of stability, as well as the methods and experiment proposed by the PUMA collaboration.

1.2. Nuclear Halos and Neutron Skins

An intuitive formulation that gives a rough estimation of the matter radius of stable isotopes R across the nuclear landscape is to assume the nucleus with N neutrons and Z protons as a hard sphere with a constant nucleon density. Then

$$R(A) = r_0 A^{1/3}, \tag{1.2}$$

where $A = N + Z$ is the mass number and $r_0 \sim 1.2$ fm.

However, as one approaches the limit of stability towards the neutron drip line, this picture starts to blur and the observed matter radius shows a non-negligible extension beyond the value calculated with Eq. (1.2).

The paradigmatic case is ^{11}Li, which was evidenced for the first time by I. Tanihata in 1985 [9]. In this experiment, the interaction cross sections σ_I of lithium isotopes ^{6}Li to ^{11}Li, beryllium isotopes ^{7}Be, ^{9}Be, ^{10}Be and helium isotopes ^{4}He, ^{6}He and ^{8}He on beryllium, carbon and aluminium targets were measured. The experimental results are shown in Fig. 1.4.

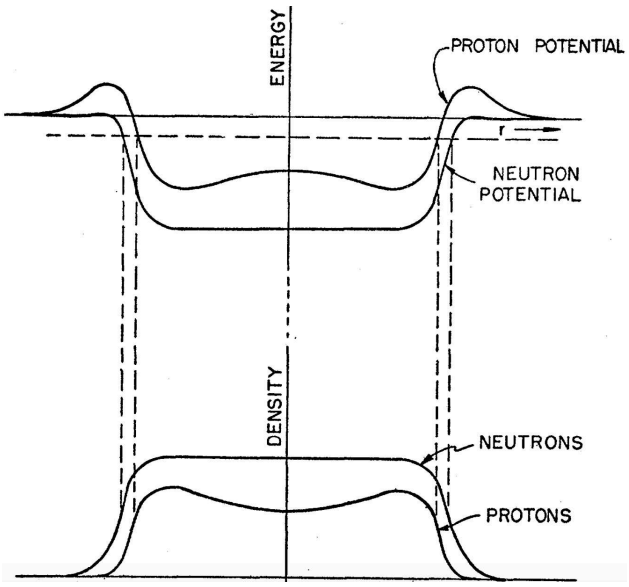

Figure 1.2.: Schematic view of the proton and neutron density distributions and the relationship with the nuclear well potential. See text for details. This figure is reprinted with permission from [7] ©2022 by the American Physical Society.

As one can observe for the case of lithium, the isotopic chain follows approximately the trend expected by Eq. (1.2) except for ^{11}Li, for which the matter radius was measured to be (3.27± 0.24) fm. Additionally, neutron-rich ^{6}He and ^{8}He also show an unexpected deviation.

This unusual extension of the nuclear density profile was later explained in terms of quantum mechanics [10]. The prominent feature is that - because near the neutron drip line, the one and two neutron separation energies are significantly reduced - the probability density distribution of the neutrons extends beyond the classically allowed region. Indeed, a neutron tunnels out and there is a non-negligible probability of finding it at large distances from the core, effectively creating a one or two neutron *halo*.

A simple way of illustrating this behaviour is by assuming a valence neutron decoupled from the internal degrees of freedom of the core nucleus, obtaining effectively a two-body system. It is also assumed that the neutron is bound by a short range potential $V(r)$.

In this case, the Schrödinger equation of the neutron reads

$$\left[-\frac{\hbar^2}{2\mu}\frac{1}{r}\frac{\partial^2}{\partial r^2}r + \frac{\hbar^2}{2\mu}\frac{\ell(\ell+1)}{r^2} + V(r)\right]\psi(\mathbf{r}) = E_s\psi(\mathbf{r}),$$

where μ is the reduced mass of the system and E_s is the separation energy.

Considering for simplicity a finite well potential, the wave function outside the well takes the form

$$\psi(r) = \left(\frac{2\pi}{\kappa}\right)\left(\frac{-\mathrm{e}^{\kappa r}}{r}\right)\left[\frac{\mathrm{e}^{kR}}{(1+kR)^{1/2}}\right],$$

where R is the width of the potential and $\kappa = \sqrt{2\mu E_s}/\hbar$. From this expression it can be observed that the separation energy drives the decay of the tail of the wave function through the variable κ.

The mean-square radius is, then,

$$\langle r^2\rangle = \frac{\int r^4\,\mathrm{d}r\,(e^{-\kappa r}/\kappa r)^2}{\int r^2\,\mathrm{d}r\,(e^{-\kappa r}/\kappa r)^2} = \frac{\hbar^2}{4\mu E_s},$$

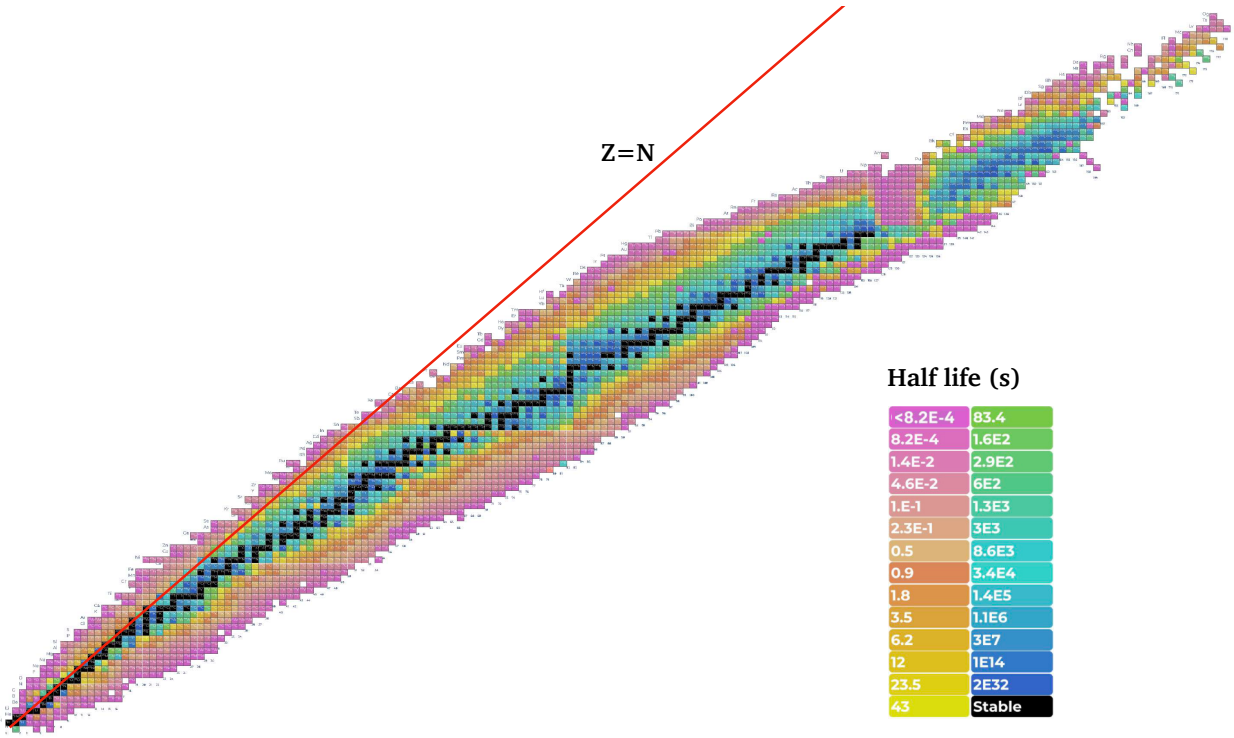

Figure 1.3.: Nuclear chart showing the nuclides half-lives and the Z=N slope in red. While black indicates stable nuclei, the half-life decreases from blue to pink. Chart from [8].

where the inverse relation between E_s and $\langle r^2 \rangle$ is manifest. In stable nuclei, the separation energy is roughly constant across the nuclear chart, in the order of $\sim 6 - 8$ MeV. On the other hand, the separation energy in neutron halos is approximately ≤ 1 MeV [11].

Additional evidence to support the notion of the halos was obtained by deducing the transverse momentum distribution of ^{11}Li from projectile fragmentations of ^{9}Li following a ^{11}Li +C reaction [12]. Considering Heisenberg's uncertainty principle

$$\Delta x \Delta p \geq \frac{\hbar}{2},$$

a narrow momentum distribution corresponds to a wide position distribution and vice versa. By looking at the transverse momentum distribution of ^{11}Li, one would expect to obtain a Gaussian-like distribution with two different widths: a more de-localized one, corresponding to the core nucleons and a narrower one related to the broader radial distribution of the halo neutrons. The observed distribution in this experiment is shown in Fig. 1.5.

The width of the wider component is $\sigma = (95 \pm 12)$ MeV/c. This value is consistent with the widths in the fragmentation of stable nuclei [13]. The other component shows a narrow width of $\sigma = (23 \pm 5)$ MeV/c, reflecting the large spread of the two outer neutrons in the ^{11}Li nucleus.

Proton-nucleus elastic scattering, a method commonly used to obtain nuclear matter distributions of stable nuclei, has also been applied by means of the inverse kinematics scheme with He and Li beams to investigate halos [14]. In this experiment, the exotic beams in the energy range of 700 to 1000 MeV would impinge in an active target Time Projection Chamber (TPC)[1], filled with hydrogen, and the momentum of the recoiled protons was measured. The scattering angle (or momentum transfer) is then deduced and the matter distributions are obtained from the best fit to the elastic

[1]An active target TPC serves as target and detector simultaneously.

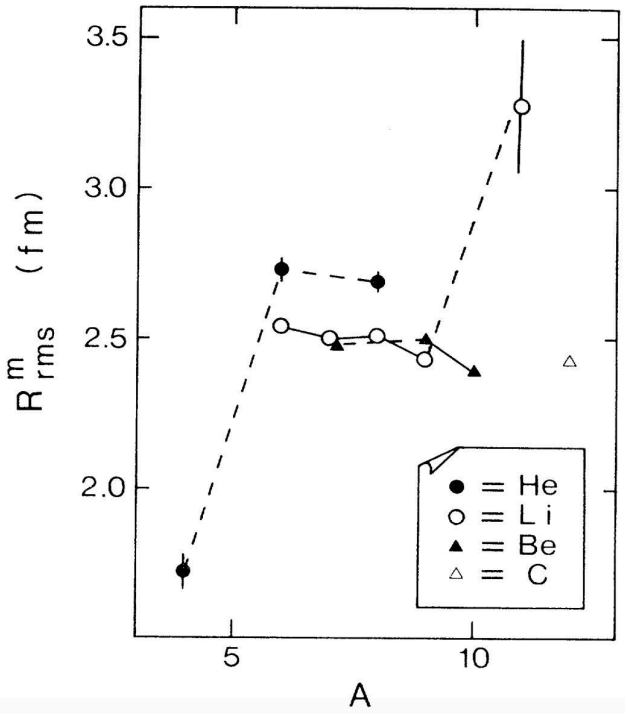

Figure 1.4.: Matter radius of Be, He, Li, C isotopes. This figure is reprinted with permission from [9] ©2022 by the American Physical Society.

scattering data. Figure 1.6 shows the differential cross sections as a function of the momentum transfer of different lithium isotopes, showing the sensitivity of the method. The results in this case are also consistent with the previous findings by I. Tanihata.

Other one- and two-neutron halos in medium-mass nuclei have been inferred from indirect measurements, such as $^{31}\mathrm{Ne}$ [16] and $^{37}\mathrm{Mg}$ [17].

Proton halos are also predicted to exist [18–20]. Unlike neutrons, protons are subject to the electromagnetic force and as such they are affected by the Coulomb barrier of the nuclei. As a consequence, their radial extension would not be as prominent as for the neutron halos. The first proton halo to be confirmed was $^{8}\mathrm{B}$ [21, 22]. Other proton halo candidates await proper experimental evidence, such as $^{13}\mathrm{N}$ [23], the two-proton halo $^{17}\mathrm{Ne}$ [24–26] and the excited state of $^{17}\mathrm{F}$ [27]. Figure 1.7 illustrates the observed or claimed neutron and proton halos.

Although halos are predicted to occur at the drip lines (for the ground state), the spatial extension of neutrons versus protons is expected to gradually change from stability towards this region. Indeed, the neutrons tend to accommodate at the surface of the density profile of neutron-rich nuclei, forming a *neutron skin*.

Neutron skins are usually characterised by the so-called neutron skin thickness, defined as the difference between the neutron and proton rms radius:

$$\Delta r_{np} = \sqrt{\langle r_n^2 \rangle} - \sqrt{\langle r_p^2 \rangle}.$$

A schematic view of the difference between a normal nucleus, a nucleus with a neutron skin and a nucleus with a neutron halo is depicted in Fig. 1.8.

Neutron skins are already observed in stable nuclei, and they are predicted to develop in neutron-rich isotopes [31–35]. Multiple theoretical models based on Hartree-Fock methods, that describe the nucleon density profile of the nuclei, predict different values for the skin thickness, ranging from

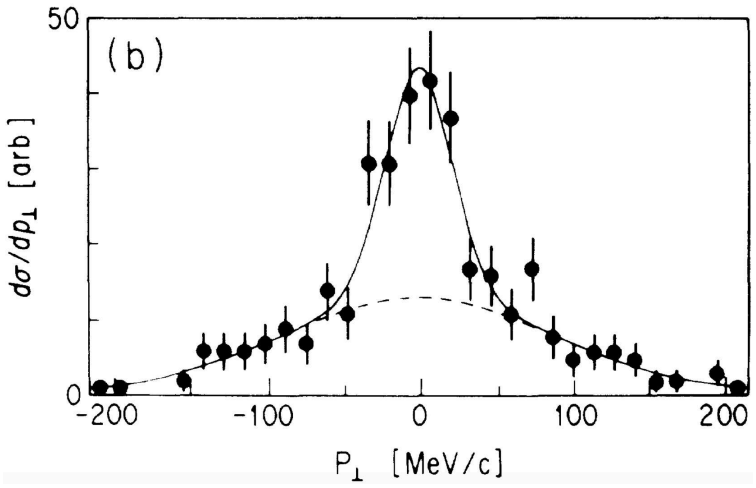

Figure 1.5.: Transverse momentum distribution of $^{9}\mathrm{Li}$ fragments. This figure is reprinted with permission from [12] ©2022 by the American Physical Society.

zero for stable isotopes with similar number of protons and neutrons, to ∼0.3 fm for ^{208}Pb with 44 excess neutrons. Figure 1.9 shows the prediction of 23 different Skyrme interactions used within the Hartree-Fock-Bogoliubov theory for tin isotopes. There are experimental methods developed to measure the neutron skin thickness, briefly explained in the following: Parity-violating electron scattering provides an approach but it is challenging since the statistical and systematic errors need to be controlled better than 1 part per billion [36]. A recent example of a neutron skin measurement with this method is the experiment performed by the PREX collaboration, that measured the neutron skin thickness of ^{208}Pb to be (0.283±0.071) fm [37].

Another way to measure the neutron skin thickness is by using hadrons as probes, such as proton-nucleus scattering [38, 39], α scattering [40], π scattering [41], coherent π^0 photoproduction [42] and nucleon removal reactions [43]. However, all these methods feature model-dependencies and a lack of proper treatment of the uncertainties which translate into large discrepancies for the extraction of neutron skins [40, 44–46]. For instance, the proton scattering method has suffered from a systematic energy dependence of the proton beam, giving values of neutron skin in ^{208}Pb ranging from negative values up to 1.5 fm [47]. Another limitation is that the determination of matter radius of radioactive ion beams with hadronic probes require intensities of about 10^4 pps at intermediate energies ($\geq$ 200 MeV/nucleon). A precision down to 0.1 fm can be achieved when the statistics are high enough [30].

The measurement of neutron skins can also be used as a tool to obtain information about neutrons stars [36, 49, 50]. Nowadays, radius of neutron stars remains poorly constrained [49]. The Neutron Star Interior Composition Explorer (NICER) telescope, installed aboard the International Space Station, has measured the mass and radius of the PSR J0030+0451 pulsar [51] via spectroscopy of low-band (0.2-12 keV) X-ray flux modulations due to rotating hot spots on the surface of a neutron star [52]. Its finding of M= $1.44^{+0.15}_{-0.14} M_\odot$ and $\mathrm{R}_e = 13.02^{+1.24}_{-1.06}$ km remains the most precise measurement performed so far. The radius, in particular, serves as a probe to describe their interior [53]. One way to infer some of these properties on earth is by measuring neutron skins.

The equation of state (EoS) describes the energy per nucleon and it can be decomposed onto powers of the proton and neutron densities or, equally, as a function of total density ρ and asymmetry α

$$\epsilon(\rho,\alpha) \equiv -\frac{B}{A} \equiv \epsilon(\rho,\alpha=0) + S(\rho)\alpha^2, \tag{1.3}$$

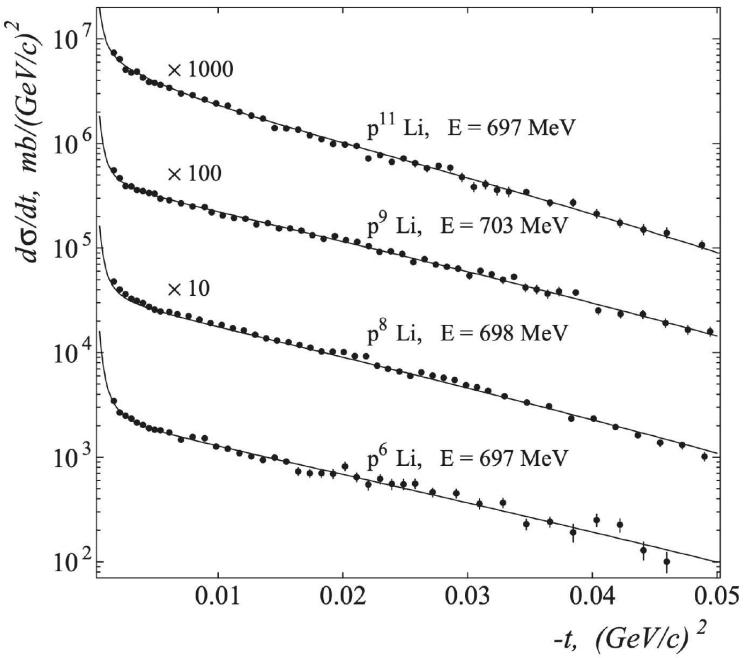

Figure 1.6.: Proton scattering amplitude as a function of the momentum transfer for lithium isotopes. This figure is reprinted with permission from [15] ©2022 by the American Physical Society.

where the first term corresponds to the EoS of symmetric matter, with

$$\alpha \equiv (\rho_N - \rho_P)/(\rho_N + \rho_P)$$

describing the symmetry between protons and neutrons. Furthermore, the symmetry energy term, $S(\rho)$, describes how the energy of nuclear matter is modified by an isospin asymmetry. There is currently a lack of understanding of the density dependence of the symmetry energy in the vicinity of the saturation density [54]. Expanding the symmetry energy at this density, one gets

$$S(\rho) = J + L(\rho - \rho_0) + \frac{K(\rho - \rho_0)^2}{2} + \ldots,$$

where the slope parameter L is the slope of the symmetry energy at saturation density. Additionally, this term is directly proportional to the pressure in neutron stars

$$P \sim \frac{1}{3}\rho_0 L x,$$

and consequently to their radius [36, 55].

On the other hand, a wide range of nuclear density functionals predict a linear relation between the neutron skins and the slope parameter, shown in Fig. 1.10. This relation implies that the measurement of neutrons skins is essential to unravel unknown features of neutron stars.

Beyond the mean field treatment of nucleons, correlations at the nuclear surface (where the nuclear density is lower than the saturation density) including the formation of clusters of deuterons, tritons and alpha particles [57–59] in the ground state of heavy neutron-rich nuclei are predicted [60]. In this case, there is a competition between the formation of clusters and neutron skins, suggesting a reduction in the neutron skin thickness with respect to the models that do not take clusters into account [61]. Experimental evidence is needed to confirm the existence of these correlations, which would then modify our understanding of the symmetry energy of the EoS.

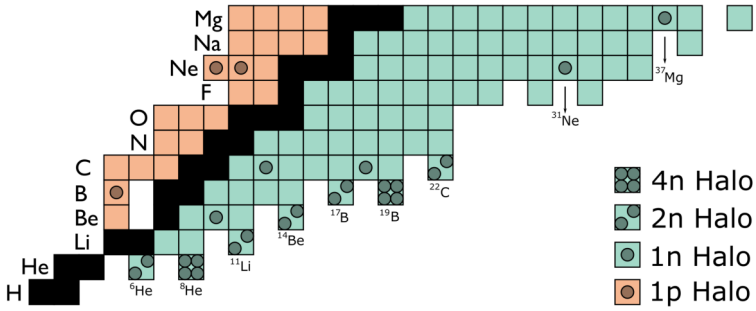

Figure 1.7.: Nuclear chart showing the existing and predicted neutron and proton halos in the light-mass region. Figure from [28], adapted from [29].

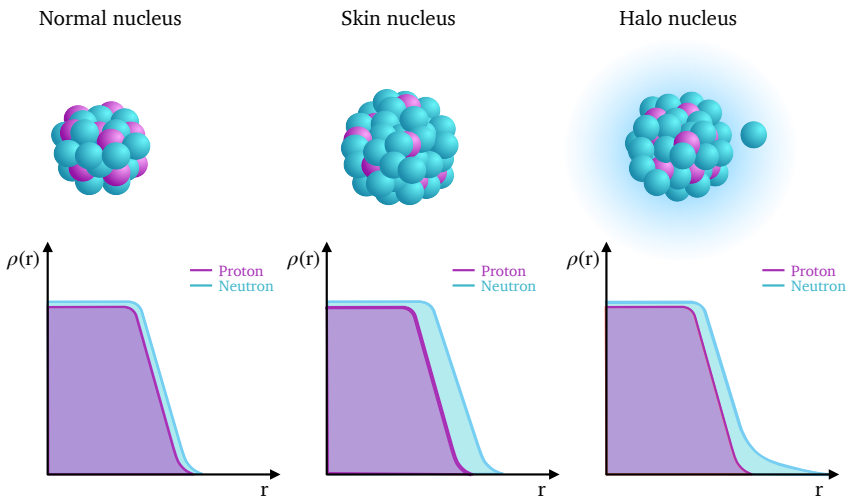

Figure 1.8.: Top: Pictorical representation of the difference between normal nuclei, skin nuclei and halo nuclei. Bottom: Schematic proton and neutron density distributions. Figure inspired by [30].

1.3. Antiprotons as a Probe

An additional tool available to investigate the structure of nuclei is the use of low-energy antiprotons. The general idea is to produce antiprotonic atoms with the ion of interest: In this process, the antiproton is captured in a highly excited state and it subsequently decays emitting auger electrons and x-rays, until it annihilates with either a proton or a neutron situated in the tail of the nucleus' density profile. As a consequence, charged and neutral pions are produced. In the following, details on the experimental techniques are given.

1.3.1. Radial Position of Annihilation

The main feature of antiprotons as probes of nuclei is that the mean radius of annihilation is estimated to take place at 2 to 2.5 fm away from the nuclear half-density radius [35].

To illustrate the sensitivity to the nuclear radial distribution, Fig. 1.11 shows the matter density distribution of ^{132}Sn (in green) together with the antiproton's annihilation probability density distribution (in blue) and a (p,2p) nucleon removal distribution with an incident energy of 250 MeV per nucleon (in red). The light blue dashed line indicates the mean radius where the annihilation

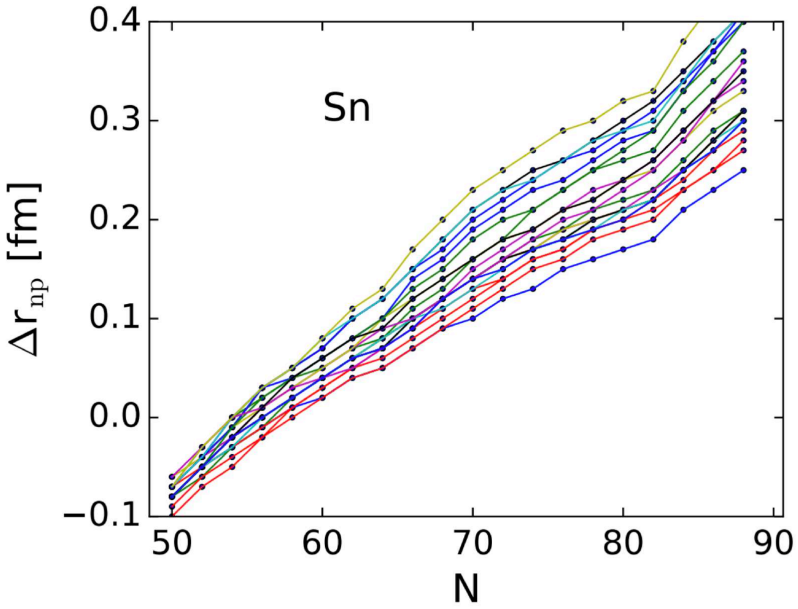

Figure 1.9.: Neutron skin of tin isotopes, calculated with 23 Skyrme forces. This figure is reprinted with permission from [48] ©2022 by the American Physical Society.

would occur, while the red dashed line shows the mean radius at which a nucleon removal following a knockout reaction at high beam energies would take place.

The annihilation distribution in this figure is a combination of the wave functions where the antiproton absorption is most probable: 45% $|n = 7, l = 6\rangle$ and 35% $|n = 8, l = 7\rangle$, while the less contributing states are not included.

1.3.2. The X-ray Method

The key aspect of this method is the measurement of the X-ray spectra produced by the de-excitation of the antiproton as it transitions towards the nucleus. This spectrum encodes information about the antiproton-nucleon strong interaction: the characteristic fingerprint is a broadening of the width Γ and a shift of the mean energy ε of the lower populated antiprotonic levels with respect to the pure electromagnetic interaction, below which no further transitions are observed due to the antiproton-nucleon's annihilation [62, 63]. As an example, Fig. 1.12 shows the x-ray spectrum of antiprotonic ^{176}Yb, where a broader width is observed in the transition 9→8. Additionally, a reduction of the yield in the same transition due to the absorption of the antiproton is manifest (see details in Ch. 6).

One of the main drawbacks of this method is that the information that can be extracted is somewhat limited: The widths and shifts of only one transition affected by the strong interaction (the last before absorption) can be deduced. Additionally, this measurement is possible as long as the width Γ is in the range of the detector resolution, in the order of a few keV [65].

1.3.3. The Pion Method

The annihilation of the antiproton with a nucleon produces multiple channels consisting of a combination of charged and neutral particles, mostly pions [66, 67] (see Sec. 3.1 for a compilation of the main channels and their branching ratios)[2]. Because the total charge of the reaction is conserved, by

[2]About 5% of the annihilations can also produce kaons [68], which are neglected at this stage but should be considered during the analysis of the data.

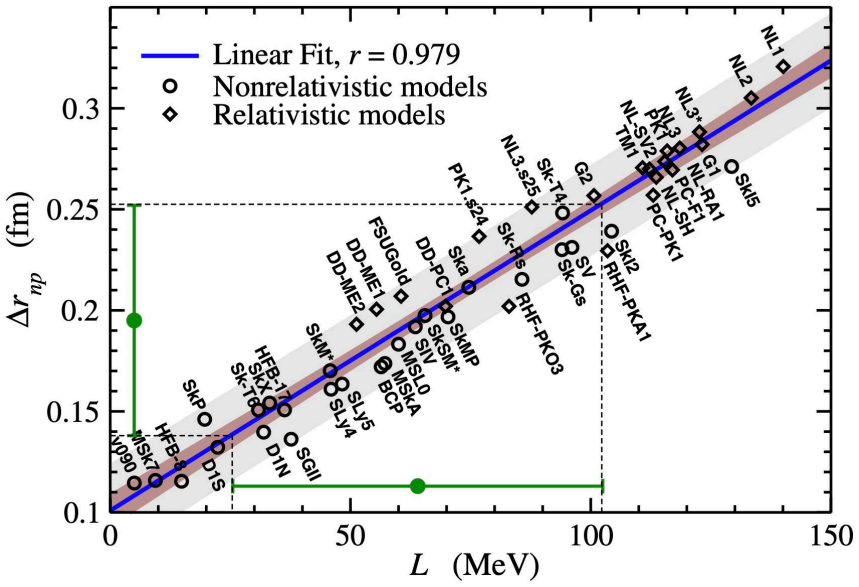

Figure 1.10.: Neutron skin thickness of ^{208}Pb as a function of the slope parameter L. This figure is reprinted with permission from [56] ©2022 by the American Physical Society.

measuring the charge of the pions it is possible to retrieve the identity of the initial nucleon:

$$\sum \pi^+ + \sum \pi^- = 0 \qquad \text{for} \quad p\bar{p},$$
$$\sum \pi^+ + \sum \pi^- = -1 \qquad \text{for} \quad n\bar{p}.$$

However, the mesons produced during the annihilation may undergo Final State Interactions (FSI) by interacting with the residual nucleus before being detected. During FSI, a pion may suffer charge-exchange or absorption [69, 70], preventing the annihilated nucleon to be accurately identified. According to intra-nuclear cascade calculations, FSI occur in 80% to 90% of the annihilations while in the rest the pions effectively "miss" the residual nucleus.

The study of the periphery of the nuclear structure with antiprotons was performed for the first time in 1973, at Brookhaven National Laboratory (USA), using this method [71]. In this experiment, a beam of low-energy antiprotons impinging on four different targets (C, Ti, Ta and Pb) was used. The detection of the charge of the pions was done with a bubble chamber, inside which the targets were placed. Their result showed a neutron excess for the Pb and Ta isotopes, although the analysis of the data with respect of FSI were considered in a schematic way (renormalised to ^{12}C). To describe their outcome they defined a "halo factor" given by

$$f_{\text{halo}} := \frac{N(\bar{p},n)}{N(\bar{p},p)} \frac{Z}{N} \frac{\text{Im}\,(a_{p\bar{p}})}{\text{Im}\,(a_{n\bar{p}})},$$

where $\frac{N(\bar{p},n)}{N(\bar{p},p)}$ corresponds to the neutron-to-proton annihilation ratio and $\frac{\text{Im}(a_{p\bar{p}})}{\text{Im}(a_{n\bar{p}})}$ is the ratio of the annihilation probability of a proton over that of a neutron. At the time, this term was found to be 0.63, in agreement with an experiment performed three years later by M. Wade [72].

1.3.4. The Radiochemical Method

The PS209 experiment, at the Low Energy Antiproton Ring (LEAR) facility at CERN provided, in 1998, additional evidence of the neutron excess in the nuclear periphery of multiple stable isotopes

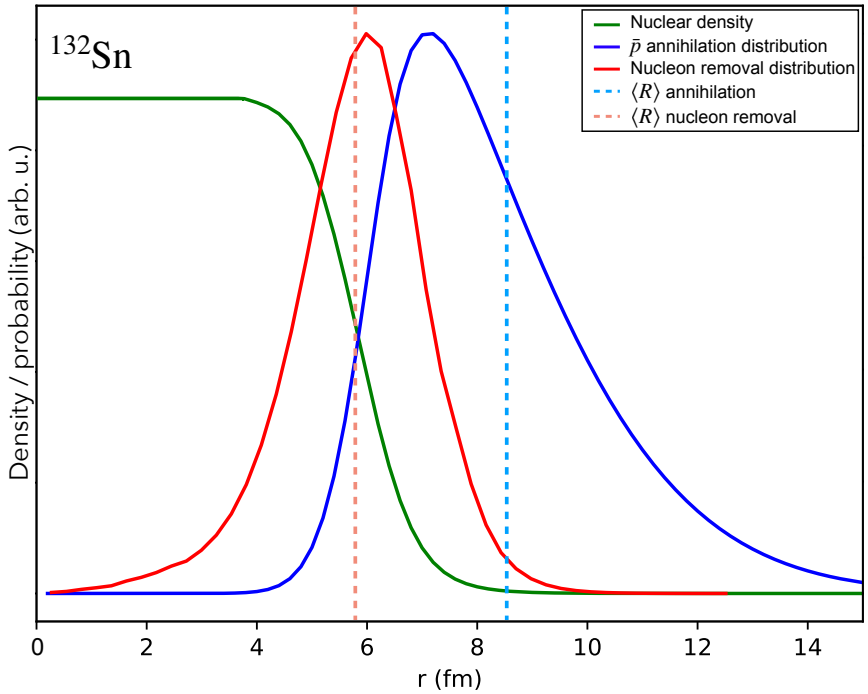

Figure 1.11.: Matter density distribution of ^{132}Sn (green curve), antiproton annihilation probability (blue curve) and (p,2p) nucleon-removal distribution with 250 MeV/nucleon incident energy. The pink dashed line shows the typical position of nucleon removal, while the light blue dashed line shows the mean annihilation radius. (p,2p) data provided by M. R. Gomez.

by measuring the yield of the radioactive products using gamma-ray spectroscopy techniques [73, 74]: When a low-energy antiproton annihilates with a target ion of mass number A_t, the residual ion has a mass $A_r = A_t$-1 with either a proton number $Z_r = Z_t$-1 and a neutron number $N_r = N_t$ or a proton number $Z_r = Z_t$ and a neutron number $N_r = N_t$-1. If both of these possible residual ions are radioactive, then the emitted γ-rays can be detected with standard spectroscopic methods, allowing to identify them. In this way, a proton to neutron annihilation ratio in the nuclear periphery can be deduced. A clear limitation of this method is that it works as long as the residual ions are radioactive.

The FSI can influence the output of these measurements as well. Indeed, as a result of this reaction, the residual nucleus can emit charged particles, neutrons or be induced into fission [69]. According to this, the method works as long as no pion re-interacts with the residual nucleus. It has been predicted that there is a geometrical dependence on the effect of FSI [75]: The missing probability, defined as the probability of no pion re-interacting with the residual nucleus, depends on the location of the annihilation and it increases with distance from the residual nucleus.Thus, a correlation between the γ yields and the annihilation site is expected. Calculations claim that this method is sensitive to the density distribution at about 3 fm away from the half-density radius, a region complementary to that probed via the two other methods, which is calculated to be between 2 to 2.5 fm away [65].

1.3.5. The PUMA Concept

The primary goal of the antiProton-Unstable Matter Annihilation (PUMA) experiment is to provide a new observable that describes the proton and neutron probability density distributions in the periphery of stable and radioactive nuclei.

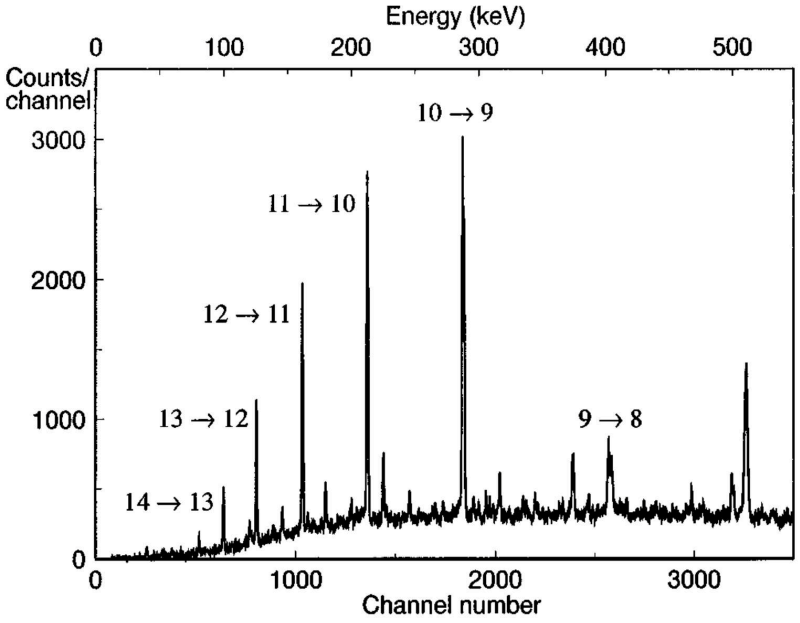

Figure 1.12.: X-ray spectrum of antiprotonic ^{176}Yb. This figure is reprinted with permission from [64] ©2022 by the American Physical Society.

The method proposed in the PUMA experiment is to calculate the neutron-to-proton annihilation ratio from the reconstruction of the charge of the emitted pions.

To provide a reliable observable, a comprehensive study of the full process that leads to the annihilation until the pions are detected needs to be considered. This process can be divided into four sequential steps, which are detailed in Ch. 6:

- The capture of the antiproton in a state with quantum numbers $|n, l\rangle$.
- The de-excitation of the antiprotonic atom through Auger and radiative emissions.
- The annihilation of the antiproton with a nucleon.
- The Final State Interactions (FSI), namely the re-interaction of the pions with the residual nuclei.

In this way, PUMA could be able to provide a way to characterise the asymmetry between protons and neutrons in the density tail of radioactive nuclei. As a consequence, new proton and neutron halos will be evidenced, and a further understanding of the neutron skin development along isotopic chains will be possible.

1.4. The PUMA Experiment in Brief

The last few decades saw an increasing interest in fundamental nuclear physics research, since the on-line production and separation of radioactive isotopes has been made possible. Nowadays there are multiple facilities [76] dedicated to the production of Radioactive Ion Beams (RIBs), such as ISOLDE at CERN (Switzerland), RIBF at RIKEN (Japan), TRIUMF (Canada), FRIB (USA), Spiral (Caen), SPES (Italy), HIAF (China) and FAIR at GSI (Germany) which will start operations in 2026.

On the other hand, the production of antiprotons "on-demand" is currently only possible at two locations worldwide: Fermilab (USA) and CERN. In the latter, antiprotons are produced by the

collision of 26 GeV protons with an iridium target. The antiprotons are decelerated to 5.3 MeV in the Antiproton Decelerator (AD) within the Antimatter Factory hall [77], and are then fed into the ELENA storage ring for further deceleration to an energy of 100 keV using RF and electron cooling [78]. Since 2021, ELENA is in full-fledge operation, delivering bunches of $\sim 4 \times 10^6$ antiprotons every 110 s to up to four experiments simultaneously.

As of today there is no facility that produces antiprotons and RIBs at the same location. To overcome this difficulty, PUMA aims at trapping 10^9 antiprotons produced in the Antimatter Factory at CERN, and transport them to the ISOLDE facility [79]. The RIBs produced there are then introduced into the PUMA trap where the annihilations occur. Figure 1.13 shows a Computer-Aided Design (CAD) of the portable setup.

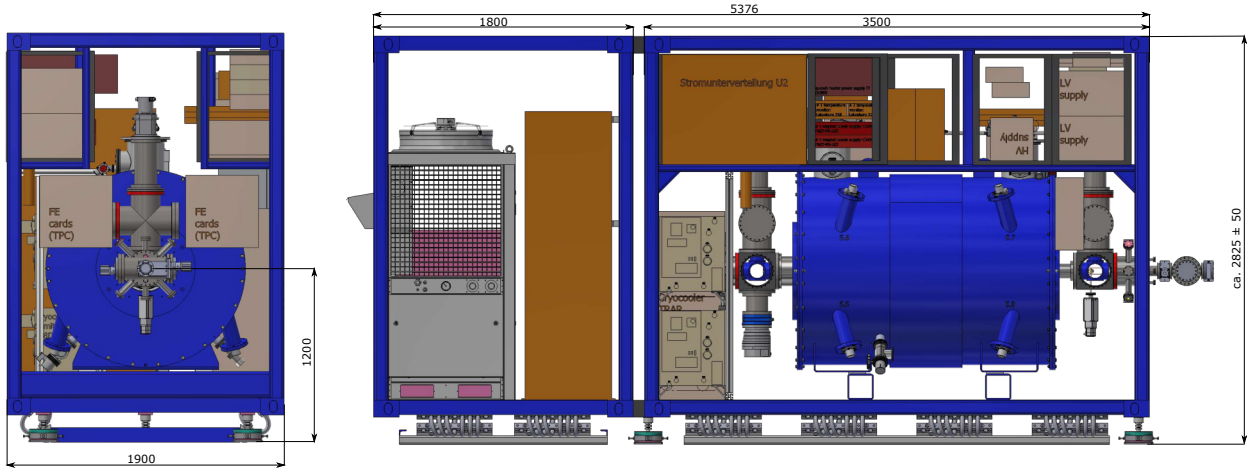

Figure 1.13.: CAD design of the PUMA setup. The dimensions are in mm. See text for details. Figure from [28].

The trapping will be achieved by means of a double Penning trap [80], which combines a region for storing the antiprotons (the *storage zone*) and a region to produce the reactions with a non-neutron plasma of 10^7 antiprotons (the *reaction zone*). The main components consist of a superconducting 4 T magnet, uniform along the beam axis (blue cylinder in the Fig. 1.13) and a set of axially symmetric electrodes that provide an electrostatic field (see Fig. 1.14). In this way, the charged particles are confined axially by the electrostatic potential and radially by the magnetic field.

Some of the technical challenges faced by PUMA have been successfully deployed in the past, albeit never performed simultaneously. The transportation of charged particles, for instance, was achieved in 1993. Indeed, $6{\times}10^4$ electrons were trapped in a Penning trap within a 4.7 T magnet and brought for over 5000 km from Massachusetts to California in the USA, to demonstrate the feasibility of antiprotons' transportation [81].

The lifetime of the antiproton plasma depends on the amount of residual gas present in the trap. To target a storage of 30 days, a pressure of 10^{-16} mbar would be needed [28]. In this case, a system cooled at ~ 4 K is necessary, as the walls then adsorb the residual gas molecules on the surface. At least two experiments at the antimatter factory have successfully reached a vacuum level $< 10^{-17}$ mbar: BASE [82], that has continuously stored antiprotons in a sealed trap for more than 7 years [83] and ATRAP [84], which has stored non-neutron plasma of 10^7 antiprotons to produce antihydrogen [85].

The effective mixing of the low-energy positive ions at ISOLDE with the antiproton plasma has been performed for antihydrogen at the the Antimatter Factory [86, 87]. At PUMA, this is achieved with a nested potential by means of a multi-ring Penning trap, as both species have opposite charges.

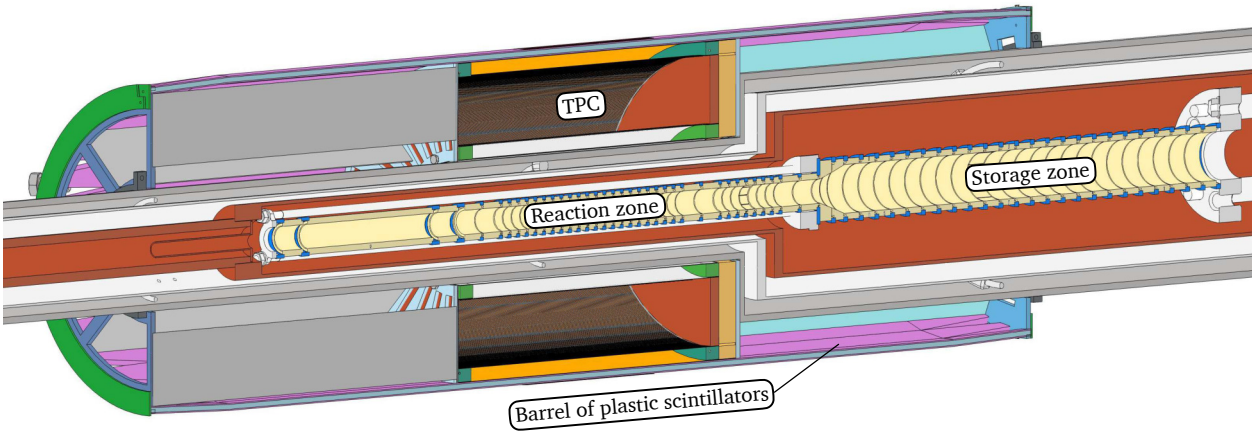

Figure 1.14.: CAD render of the cross sectional view of the trap and detectors designed for the PUMA experiment.

The production of antihydrogen has, as well, motivated the use of these kind of cylindrical traps at the Antimatter Factory in different experiments, such as Alpha [88] and AEgIS [89].

The detection of the pions, main subject of the first part of this thesis, is explained extensively throughout Ch. 2 to 5.

In the following, Ch. 2 is dedicated to the physical principles driving the interaction of charged particles and subsequent detection with gas chambers, particularly with TPCs. Afterwards, Ch. 3 specifies the simulations performed for the optimisation of the pion's detection. In Ch. 4, the simulations concerning the field cage design and performance are explained. Finally, in Ch. 5, the TPC construction and mechanical structure are detailed.

On the second part of the thesis, the antiprotonic decay and annihilation is described. In Ch. 6 the cascade code is used to benchmark existing measured antiprotonic x-ray yields and in Ch. 7 a study of the sensitivity of PUMA with Sn and Ca isotopes is presented.

Part I.

Annihilation Detection

2. Physics Background and Operation Principles of a TPC

The Time Projection Chamber (TPC) was initially developed by D. Nygren at the Lawrence Berkeley Laboratory in 1978 to study electron-positron collisions in the PEP (Positron-Electron Project) at the SLAC National Accelerator Laboratory in the USA [90]. One of its main features is the capability of providing a full 3D spatial reconstruction of a charged particle's track. The detector consists of a chamber filled with an ionizing gas in addition to two conductive endcaps on each side and a field cage that provides a uniform electric field. The anode is segmented to obtain 2D spatial information: when a charged particle traverses the chamber, the gas is ionized along its track, producing free electrons that drift towards the anode due to the electric field. Once near the anode, the electrons undergo an avalanche process as a product of a multiplication region, included to amplify the signal. The signal is subsequently induced and eventually collected in the segmented plane and the 2D projected track is obtained.

Additionally, with known transport parameters (namely the electrons' drift velocity) and the timing information (given by an external timing signal correlated to the charged-particle production time) the third coordinate of the track is extracted. Figure 2.1 shows the basic working principle of a TPC.

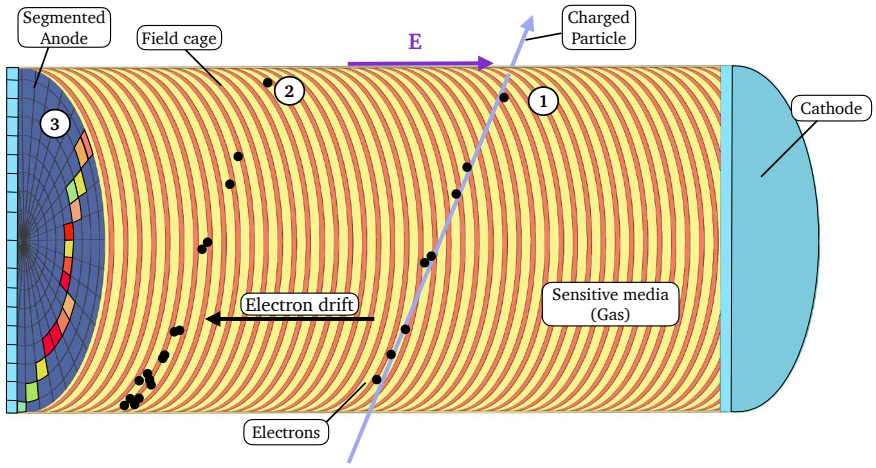

Figure 2.1.: Diagram of the working principle of a TPC: 1) A charged particle traverses the chamber, ionizing the gas. 2) The electrons drift towards the segmented anode due to the external electric field and are multiplied before collection. 3) The signal is induced in the anode, obtaining a 2D projection of the track.

In the following sections, details of the salient physics of charged particles through matter will be given, followed by the principles of motion in gases for particle detection. In addition, a section dedicated to the multiplication region is presented.

2.1. Interaction of charged particles with matter

2.1.1. Energy deposit in a medium

There are two dominant processes[1] driven by the electromagnetic interaction of heavy charged particles with matter: the excitation and the ionization of the material's constituent atoms, as the passing charged particle deposits energy in it. The latter process can be quantified mathematically with the Bethe-Bloch formula [91] for the particle energies treated herein: considering a particle with velocity v and charge z interacting with a material of density ρ, atomic number Z and mass number A, the mean energy loss rate is given by

$$-\left\langle \frac{dE}{dx} \right\rangle = 4\pi \mathrm{N_A} r_e^2 \mathrm{m_e c^2} \rho z^2 \frac{Z}{A} \frac{1}{\beta^2} \left[\frac{1}{2} \ln \frac{2 m_e c^2 \beta^2 \gamma^2 T_{\max}}{I^2} - \beta^2 - \frac{\delta(\beta\gamma)}{2} \right], \tag{2.1}$$

where c is the speed of light, γ is the Lorentz factor defined by $\gamma = 1/\sqrt{1-\beta^2}$, $\beta = \mathrm{v/c}$, $\mathrm{N_A}$ is Avogadro's constant, I is the mean ionization potential of the medium considered, r_e and m_e are the electron's classical radius and rest mass, respectively and T_{max} the maximum ionization energy that can be transferred to one electron. Figure 2.2 shows the energy deposit (also referred to as the mass stopping power of the material) for different materials and charged particles as a function of their momentum.

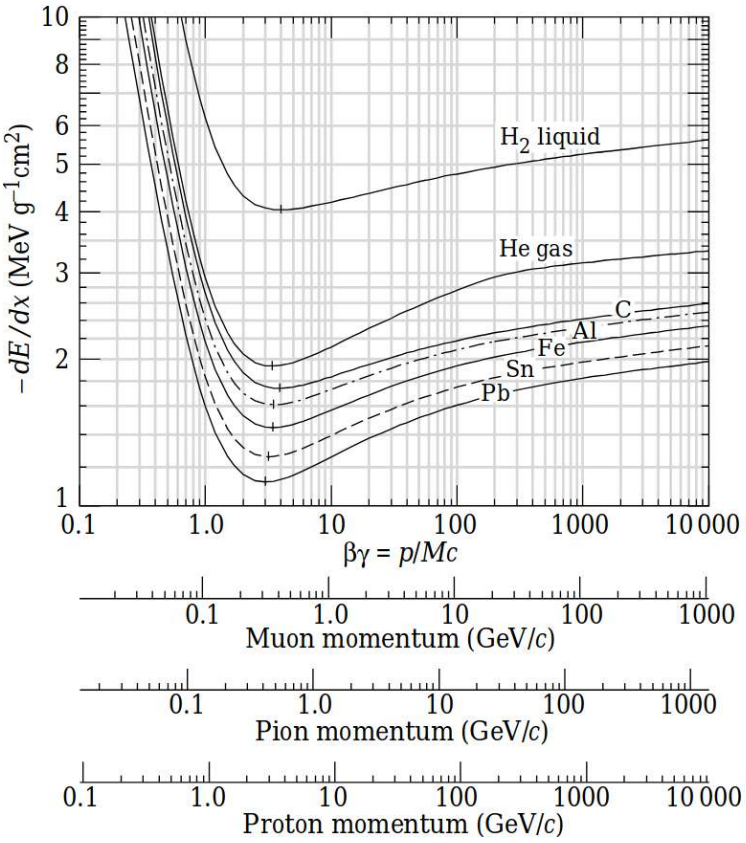

Figure 2.2.: Mass stopping power of copper, as a function of charged particle's (muon, pion and proton) momentum. Figure from [92].

In the lower energy domain, the energy deposit is driven by the $1/\beta^2$ factor up to a speed of about

[1] Another important process is the *Bremsstrahlung radiation*, dominant for electrons in the energy range E > 10 MeV.

0.9c, where a global minimum is reached. For larger values of $\beta\gamma$, the relativistic extension of the transverse electric field is observed and the logarithmic term starts to dominate (damped by the correction factor δ). The particles with a momentum such that they deposit energy in the range that corresponds to this minimum ($\sim$1GeV/c) are called the Minimum Ionizing Particles (MIPs). This minimum ionization is very similar across different materials for particles of the same charge, as evidenced in Fig 2.2.

It is often the case, particularly in gas detectors, that the sensitive material is a mixture or compound of substances. In that case, a good approximation of the mean energy deposit is to use the *Bragg's rule* [93]

$$\left\langle \frac{dE}{dx} \right\rangle = \sum_j w_j \left\langle \frac{dE}{dx} \right\rangle_j ,$$

where the average energy deposit for each compound j is weighted by the fraction w_j of that element in the mixture.

In the case of PUMA, the typical momentum of charged pions after the annihilation is 100 MeV/c. Considering the medium to be pure Ar at one atmosphere, and following Fig. 2.2, the pions will be close to MIPs and their energy loss in the gas is $\sim$200 keV/cm.

2.1.2. Creation of electron-ion pairs

The ionization probability of a charged particle traversing a gas is related to the mean free path of the charged particle $\lambda = 1/(\sigma_i n)$, where σ_i is the ionization cross-section and n the number density of electrons. Because the ionization probability is a random process and each encounter is independent, a particle with a track length L has a poissonian probability of ionizing k particles

$$P(L/\lambda, k) = \frac{(L/\lambda)^k}{k!} \exp(-L/\lambda),$$

where the mean number of *primary ionizations* is L/λ. The number of primary ionizations per cm for different gases is shown in Fig. 2.3.

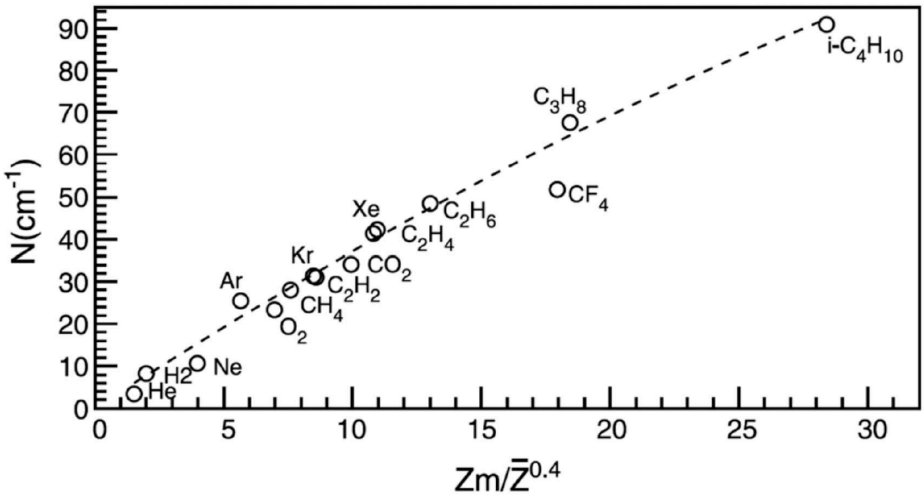

Figure 2.3.: Primary ionizing collisions per cm as a function of the atomic number of gases at standard conditions of temperature and pressure. This figure is reprinted with permission from [94] ©2022 by Springer Nature.

If an electron acquires sufficient kinetic energy, it might produce secondary ionizations by further ionizing atoms, creating a cluster. However, the probability of this process is usually low [95] and these high-energy electrons (called $\delta-$electrons) are rapidly stopped by the quenching gas of the mixture (see Sec. 2.2).

Considering the above, the mean energy needed to produce an electron-ion pair is

$$w = \left\langle \frac{dE}{dx} \right\rangle L.$$

However, it should be noted that w is not equal to the ionization potential of a gas, since only some energy is lost by ionization, while interactions also lead to the excitation of the atoms. As an example, the ionization potential of Ar is 15.8 eV while the mean energy needed for pair creation is 26 eV [95]. Following the estimation for PUMA in Sec. 2.1.1, it is deduced that the mean number of electron-ion pairs created by the pions in an argon gas at normal temperature and pressure (20 and 1 atm) is $\sim$ 650/cm.

2.2. Principles of Gas Detectors

Gaseous detectors are widely used in particle and nuclear physics experiments [96–99] since they offer excellent particle identification and tracking capabilities with large solid angle acceptance, together with a low material budget and a large dimension range from a volume of a few cubic decimetres, such as the MINOS TPC [100] to several cubic meters, as the ALICE TPC, at CERN [96].

The behaviour of produced electrons in a gas detector depends strongly on the electric field applied across the detector volume. As a consequence, the charge collection varies as shown in Fig. 2.4.

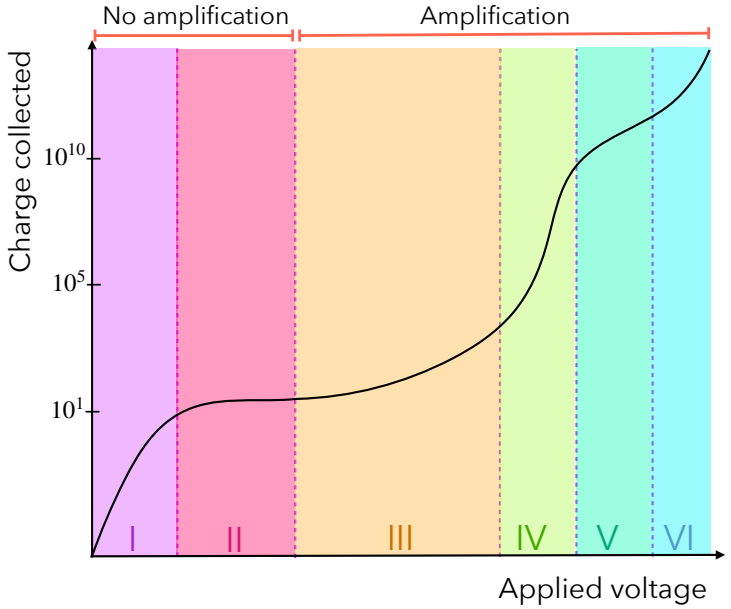

Figure 2.4.: Qualitative division of the gas operation modes as a function of the applied voltage (See text for description).

In Region 1 Electron-ion recombination is dominant: when there is no or a too small electric field applied, all electrons eventually recombine and no charge is collected. As the applied voltage increases (region II), the ionized electrons feel a force due to the field and do not have time to recombine, as they end up being collected. In this "ionization chamber region", the charge collected

corresponds to the energy deposited by the charged particle. In region III, the intensity of the field is enough to accelerate the electrons such that secondary ionizations are produced, and the signal collected is proportional to the primary one. For an even higher voltage (region IV), the number of electrons produced is such that space charge effects start to take place, UV photons above the ionization energy are emitted and the proportionality is lost, until eventually a discharge occurs (region V). In this phase (Geiger-Müller) a chain reaction develops. Above this stage (in region VI) the electric field generates a continuous discharge, and hence the chamber is no longer capable of detecting any incident ionization.

In an ideal gas, the ionization electrons should have a low probability of recombining with the ions so that they can drift across the volume and be collected. On the other hand, uncontrolled creation of secondary electrons and UV photons that render the detector non-operational should be avoided. These seemingly conflicting properties can coexists by using an adequate combination of gases with distinctive properties. A relevant parameter to consider is the *electron attachment*, which quantifies the probability of an electron to recombine with an ion of a certain gas. For an electron with velocity v, the attachment rate R is proportional to the attachment cross section σ_a and the number density n: $R = v\sigma_a n$.

Because of their closed shell structure, the attachment rate of noble gases is among the lowest across the periodic table of elements. For the same reason, their first ionization energy (which varies between 22 eV for Xe to 46 for He [101]) is higher than the average, which poses a limit to the gain of the gas (see Sec. 2.2.4). However, an effect that one can take advantage of is the *Penning effect*: When the excitation energy of a gas A is higher than the ionization energy of a gas B, the molecules of B can be ionized by collisional transfer of the de-excitation energy of A.

$$A^* + B \rightarrow A + B^+ + e^-$$

This effect can significantly increase the gain of the gas mixture. For instance, it was observed that adding 0.13% of Ar to pure He changed its ionization energy from 41.3 eV to 29.7 eV [102].

To prevent discharges, the primary gas is usually mixed with a *quencher*. These types of gases absorb the UV photons and de-excite mostly through rotational and vibrational transitions. An example are polyatomic gases, such as CH_4. Inorganic gases such as CO_2 can also be used [96]. The addition of a small percentage of a quencher is paramount to allow a stable operation with higher gains that could reach values up to 10^6 [103]. A very common mixture for gas detectors is the so-called "P-10", used for instance in the STAR TPC [104]. The primary gas is Argon (90%) and a small amount of CH_4 (10%) is added to quench the secondary electrons and UV creation.

2.2.1. Drift of electrons in a gas

One of A. Einstein's realisations during his *Annus mirabilis*[2] (or "Miracle year") was that the random motion of a dust particle in water, observed by R. Brown in 1827 [109], was due to the thermal movement of the molecules of the liquid [106]. Indeed, any particle of mass m immersed in a "bath" of atoms at temperature T is in a thermodynamical equilibrium by collisions, therefore acquiring a mean kinetic energy

$$v = \frac{\lambda}{\tau} = \sqrt{\frac{3\mathrm{k_B}T}{m}},$$

where $\mathrm{k_B} = 1.38 \times 10^{-23}\ JK^{-1}$ is Boltzmann's constant, and λ and τ are the mean free path and mean free time between collisions, respectively.

[2]This expression refers to the year 1905, where Einstein published four ground-breaking papers in which he explained: the photoelectric effect [105], the brownian motion [106], special relativity [107] and the mass-energy equivalence [108].

The consequence of this random motion is that, for a localized cluster of N particles (say, electrons in a gas) in absence of external forces, there is an isotropical spatial diffusion over time t, described by a Gaussian distribution

$$\frac{dN}{N} = \frac{1}{\sqrt{4\pi Dt}} \mathrm{e}^{-\frac{\vec{x}^2}{4Dt}} \, \mathrm{d}\vec{x},$$

with a spread in 3D defined by the diffusion coefficient D:

$$\sigma(\vec{x}) = \sqrt{6Dt},$$

where $D = \frac{v\lambda}{3}$.

Using the definition of the mean free path $\lambda = \frac{1}{\sigma_i n}$, where σ_i is the interaction cross section and n is the number density, the diffusion coefficient becomes

$$D = \frac{2}{3P\sigma_i} \sqrt{\frac{(\mathrm{k_B}T)^3}{\pi m}},$$

where the ideal gas law $P = nk_BT$ is used to obtain an expression that only depends on the gas parameters P, T and the interaction cross section σ_i. Because of their large mass difference, the diffusion of electrons is much more gas dependent than the ions. Indeed, the diffusion of an electron cloud can vary from 100 µm to 1 mm after 1 ms, depending on the gas, while the diffusion of an ion cloud is roughly 140 µm in the same time period, independently of the gas used.

2.2.2. Drift in the presence of an external electric field

When an external electric field $\vec{E}$ is applied, the electrons are accelerated between collisions in the direction of the field in superposition with the random scattering explained in Subsec. 2.2.1. As a consequence, there is a net velocity - so-called drift velocity $\vec{v}_d$ - that emerges and can be described by

$$\vec{v}_d = \frac{e\vec{E}}{m}\tau,$$

where e is the charge of the electrons, τ the average time between collisions and $\vec{E}$ is the electric field. The term $\frac{e\tau}{m}$ is usually referred to as the mobility μ of the electrons. It should be noted that $\vec{v}_d$ is a mean value which describes the collective motion of electrons in a medium with an electric field, an it is not the instantaneous velocity that the electrons acquire between collisions.

Because of the drift velocity's mass dependence, ions are $\sim$1000 times slower than electrons.

In addition to the electric field, the drift velocity depends greatly on the gas composition and its macroscopic physical properties (pressure, temperature). An increased pressure P increases the probability of collisions and reduces the mean free path of the electrons, decreasing the drift velocity. To pull out this effect, a *reduced field* E/P is often used. Figure 2.5 shows the dependency of the electron drift velocity with respect to the electric field for different gas mixtures. A global maximum is reached in the range of 100–300 V/(cm atm), which implies that small variations in E/P will not affect the drift velocity, making it the preferred range of operation.

At low electric fields, the drift velocity increases sharply due to the decrease in the interaction cross section, as the electrons acquire more energy. However, C. Ramsauer [110] observed that the scattering cross section of electrons in a gas had a minimum value for certain kinetic energies instead of decreasing monotonically, as expected by the classical explanation.

Because the electrons start drifting in a privileged direction, the diffusion is not isotropic anymore. In this case, one can distinguish between a transverse and longitudinal (along the drift direction)

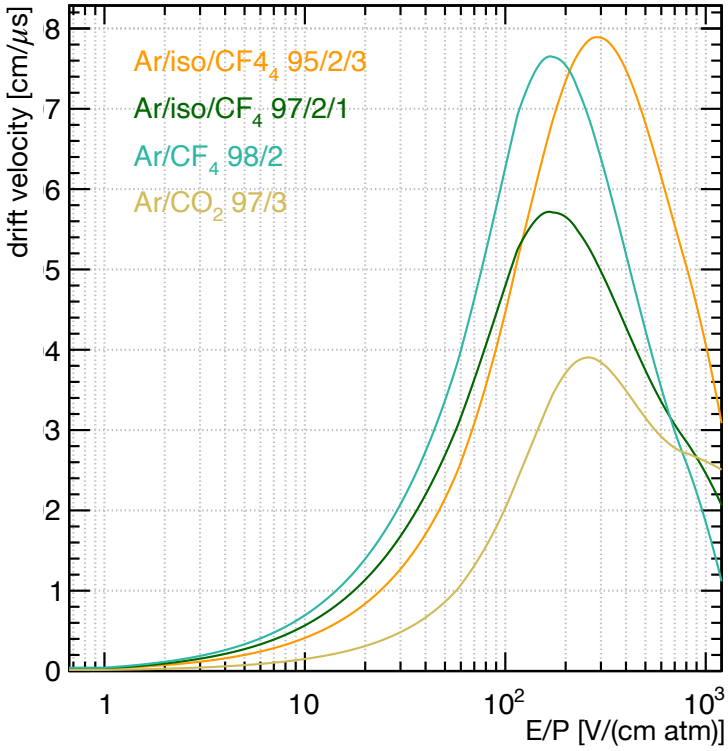

Figure 2.5.: Drift velocity for different Argon based gases as a function of the applied electric field and pressure.

diffusion coefficients, D_T and D_L, respectively. After a drift distance L, the spread in the transverse and longitudinal directions, σ_T and σ_L, of an electron cloud is

$$\sigma_T^2 = 4D_T L/v_d,$$
$$\sigma_L^2 = 2D_L L/v_d.$$

As shown in Fig. 2.6, when the electric field is high enough, the additional energy of the electrons in the drift direction produces a decrease in the longitudinal diffusion with respect to the transverse diffusion.

2.2.3. Drift in the presence of an external magnetic field

The presence of a magnetic field modifies both the drift properties and the diffusion of the electrons. A more general description of the motion of an electron is given by the Langevin equation

$$m\frac{d\vec{v}_d}{dt} = e\vec{E} + e\vec{v}_d \times \vec{B} - K\vec{v}_d, \tag{2.2}$$

where the right hand side is nothing but the Lorentz force with an additional "viscosity" term which describes a frictional force proportional to $\vec{v}_d$, caused by the interaction of the particle with the gas.

Defining $\tau = m/K$ and the electron's cyclotron frequency $\omega = eB/m$, there is a stable solution for $t \gg \tau$, in which $\frac{d\vec{v}_d}{dt} = 0$:

$$\vec{v}_d = \frac{e}{m}\tau|\vec{E}|\frac{1}{1+(\omega\tau)^2}\left(\hat{E} + \omega\tau\left[\hat{E}\times\hat{B}\right] + (\omega\tau)^2\left(\hat{E}\cdot\hat{B}\right)\hat{B}\right). \tag{2.3}$$

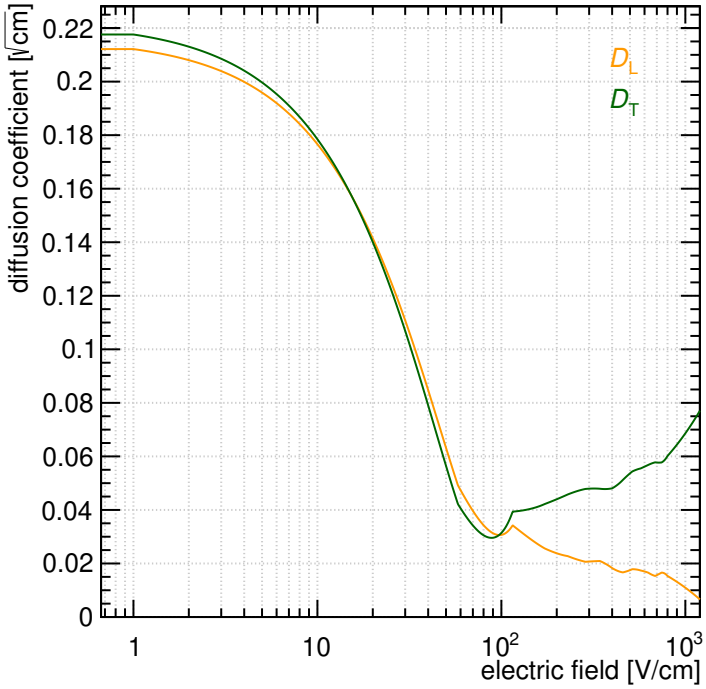

Figure 2.6.: Transverse and longitudinal diffusion for Argon gas as a function of the applied electric field.

In the particular case where $\vec{E} \parallel \vec{B}$, which is the usual case for TPCs, the drift velocity contains only one non-zero component (in the direction of the field lines) and takes the form

$$v_d = \frac{e/m}{1+(\omega\tau)^2}\left[E + (\omega\tau)^2 \frac{E\cdot B}{\vec{B}^2} B\right].$$

Note that if $\vec{B} = 0$, the expression obtained in Sec. 2.2.2 is recovered. As an example, $\omega\tau \sim$0.3 for the ALICE TPC gas mixture (Ne:CO_2:N_2/85:10:5), while the same factor is approximately 2 for the P10 gas mixture. In small magnetic fields or short time between collisions, $\omega\tau \sim$0, and the electrons tend to follow the E lines. On the contrary case, they will tend to curl around the magnetic field lines. This effect is much less prominent for ions due to their mass difference ($\omega\tau \sim 1/m$).

The diffusion is also modified in the presence of a magnetic field. Considering again the case where $\vec{E} \parallel \vec{B}$, the Lorentz force causes a circular motion in the transverse trajectory, effectively reducing the transverse diffusion

$$D_T(\omega) = \frac{D_T(0)}{1+\omega^2\tau^2}.$$

This effect is clearly observed in Fig. 2.7, where the transverse diffusion of drifting electrons in an Ar based gas mixture was measured.

2.2.4. Amplification

Considering that only a few number of electrons are created by primary ionization, well below the nominal electronic noise of the readout used in gaseous detectors [112], it is therefore necessary to amplify the signal before collection.

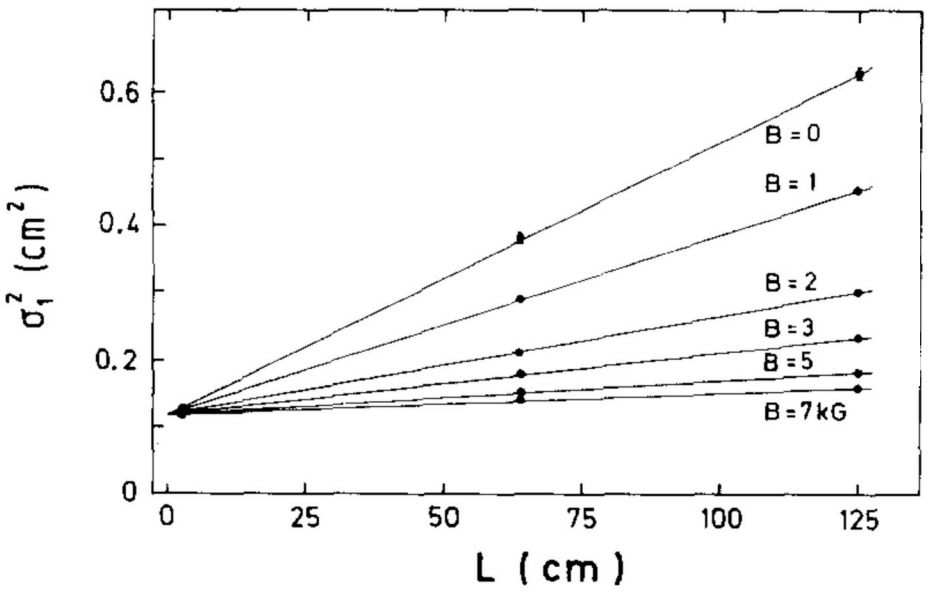

Figure 2.7.: Transverse diffusion in the presence of magnetic fields for Ar/CH_4:91/9 at 1 atm and a drift field of 115 V/cm. This figure is reprinted with permission from [111] ©2022 by Springer Nature.

The way this is achieved is based on the principle of the avalanche effect: Immersed in a strong electric field (typically some kV/cm), a free electron with a mean free path λ is accelerated, increasing the ionization cross section of the gas [113]. Secondary electrons are produced and a multiplication process begins, usually stopped by electrons being captured or absorbed by the detector. The amount of electrons created in this process (typically $>10^4$) was quantified by J. Townsend [114]. For an initial cloud of N_0 electrons in a uniform electric field, the number of electrons created by the avalanche effect in a path of distance x is

$$\mathrm{N} = \mathrm{N}_0 e^{\alpha x}$$

where $\alpha = \lambda^{-1}$ is the so-called *Townsend coefficient*. The multiplication factor, or *gain*, is then given by

$$\mathrm{G} = \frac{\mathrm{N}}{\mathrm{N}_0} = e^{\alpha x}.$$

In the general case where the electric field is non-uniform, the Townsend coefficient might not be constant

$$\mathrm{G} = \exp\left[\int_{x_1}^{x_2} \alpha(x) dx\right].$$

This value depends on the strength of the electric field and the gas composition and its determination with existing software is valuable to assess the expected current and improve the signal-to noise-ratio. It is important to note that even though the mathematical expression describes an exponential increase, in reality the gain is limited by the electrical breakdown at which point discharges occur (see Sec. 2.2), at $\mathrm{G} < 10^8$, called the Raether limit [115].

One (trivial) negative consequence of the multiplication of electrons is that also ions are multiplied. Because of their positive charge, the ions drift in the opposite direction of that of electrons at a rate ~ 1000 times slower, due to their mass. In general, a small percentage $< 15\%$ [103] of the ions will drift back into the main volume of the detector after amplification, while most of them will be absorbed by the detector (see below). The fractional Ion Back Flow (IBF), defined as the ratio

between the current measured in the cathode (due to ions) over the one measured in the anode (due to electrons) has been extensively studied [116–118] since it induces strong field distortions in the otherwise uniform electric field, compromising the tracking of the electrons. In addition, an ion current can create discharges and potentially damage the detector.

In modern TPCs, there are two technologies which are used for electron amplification: the Gas Electron Multiplier [119] and the Micromegas [120] detectors. Both technologies provide a strong focusing effect: since the field in this region is typically ten times stronger than in the drift region, the field lines are compressed in the transition interface, allowing for a high percentage of electron transmission. Details of their working principle are given in the following.

GEM

The standard configuration in this type of technology consists of etching holes of 50 μm radius (with a typical pitch of ~ 140 μm) into a 50 μm Kapton foil, coated in copper on both sides. The amplification of the charge is achieved by applying a voltage difference of a few hundred volts between the top and the bottom sides, creating a strong electric field inside the holes. The electrons are then amplified, with a typical gain of $\sim 10^3$ and most of the ions (that slowly drift towards the direction of the incoming tracks) are absorbed by the foil, where the IBF is in the order of ∼15% [116]. A sketch of the device is shown in Fig. 2.8.

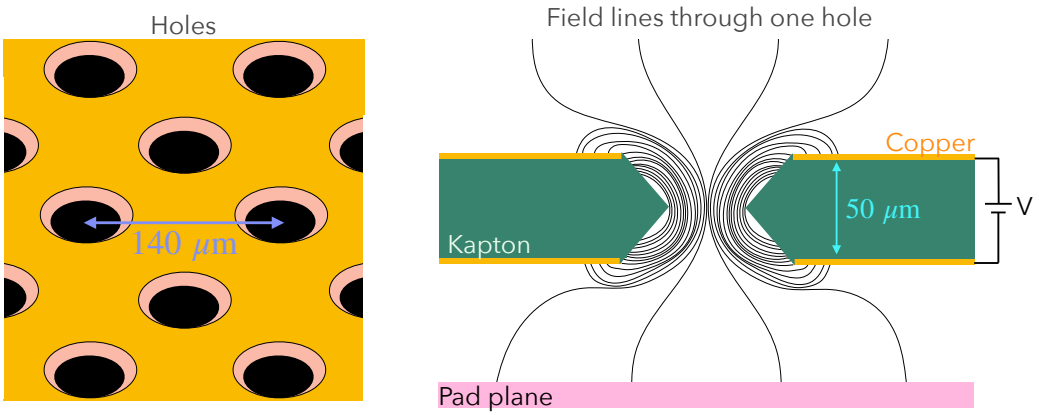

Figure 2.8.: Sketch of the working principle of a GEM.

Multiple GEMs stacked on top of each other is a common configuration used to obtain an even higher amplification and additionally reduce the ion back flow [121–123]. For a stack of four GEMs, an IBF lower than 3.8% was achieved for Ar-CO_2 based mixtures [116]. In this type of configuration, the operation voltage to produce a detectable signal can be reduced while the overall gain is kept or even improved. Another key advantage is minimization of discharges that can damage or degrade the lifetime of the detector and the readout electronics [124].

Micromegas

Even though both technologies are widely used in nuclear and particle physics experiments and offer similar advantages, the expertise acquired by past experiences is the main reason why in the case of the PUMA experiment, the Micro-MEsh GAseous Structure (Micromegas) is used to amplify the charge collection.

Developed by G. Charpak and I. Giomataris at Saclay, France in 1994 [120], the Micromegas consists of a metallic grid (micro-mesh) with 17 μm openings every 25 μm, placed at typically 128 μm

from the pad plane. By applying a strong electric field of a few kV/cm to the gap, the avalanche process can take place. The mesh has an ∼80% transparency to allow an efficient penetration of the primary electrons into the amplification region. The micro-mesh also contributes to the IBF mitigation by absorbing the majority of the ions created during the avalanche [125, 126]. An illustration of the concept is shown in Fig. 2.9.

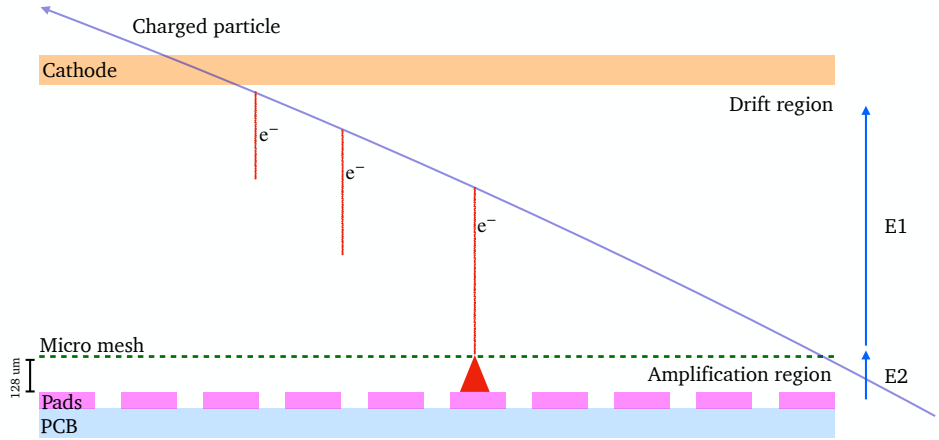

Figure 2.9.: Sketch of the working principle of the Micromegas detector.

The main advantage of the micromegas detector is that it can withstand sparks without compromising the performance of the full instrument, even if certain regions might be damaged [127]. Furthermore, it is easily produced in a large range of dimensions. A critical aspect, however, is the need to maintain a uniform gap between the mesh and the pads in order to achieve an even gain throughout the pad plane. This is accomplished by the stretching of the mesh together with the implementation of regular pillars across the mesh-to-anode gap. A convenient manufacturing method using photolithographic techniques, called bulk micromegas, allows for an integrated anode-mesh structure. In this way, large-area micromegas with a simpler and more reliable structure is achieved. [128]

In the simplest scenario where the charge is induced in only one pad (details about signal induction are given in Sec. 2.3.1), the spatial resolution is roughly the size of the pad. However, one way to improve the position resolution of the detector without raising the number of channels and additionally protecting the electronics from sparks, is by using the resistive-Micromegas technology. In this case, a foil with high surface resistivity - typically a Diamond Like Carbon (DLC) foil - is glued on top of the pad plane. By doing so, the cluster of electrons produced in the avalanche is spread over the DLC following the 2D-Telegraph equation [129]:

$$\frac{\partial \rho}{\partial t} = \frac{1}{RC}\left[\frac{\partial^2 \rho}{\partial r^2} + \frac{1}{r}\frac{\partial \rho}{\partial r}\right]. \tag{2.4}$$

Assuming an infinite plane and a delta function point charge, the charge density ρ is

$$\rho(r,t) = \frac{RC}{2t} e^{-r^2 RC/(4t)}, \tag{2.5}$$

where RC is the time constant determined by the DLC resistance R and the capacitance C created by the pad plane and the DLC, where the dielectric constant of the glue has to be considered.

Realistically, the charge is not point-like but a gaussian-shaped cloud of n_e electrons of charge q with a width w, proportional to the transverse diffusion. In this case, the solution is given by

$$\rho(x,y,t) = \frac{qn_e}{2\pi\left(\frac{2t}{RC}+w^2\right)} e^{-r^2/\left[2\left(\frac{2t}{RC}+w^2\right)\right]}. \tag{2.6}$$

Integrating eq. (2.6) constrained to a pad's boundaries x_{high} , y_{high}, x_{low} and y_{low}, it is then straightforward to obtain the charge on a single pad [130]:

$$Q_{\text{pad}}(t) = \frac{qn_e}{4}\left[\text{erf}\left(\frac{x_{\text{high}}}{\sqrt{2}\sigma_r}\right) - \text{erf}\left(\frac{x_{\text{low}}}{\sqrt{2}\sigma_r}\right)\right]\left[\text{erf}\left(\frac{y_{\text{high}}}{\sqrt{2}\sigma_r}\right) - \text{erf}\left(\frac{y_{\text{low}}}{\sqrt{2}\sigma_r}\right)\right],$$

where $\sigma_r = \sqrt{\frac{2t}{RC}+w^2}$.

As an example, for a fixed gain of 6000, a 50 μm foil of Kapton with a resistance R=1kΩ/□ on top of a 100 μm layer of glue and an electronics shaping time of 500 ns (with a negligible transverse diffusion), a spread of ~ 1.5 mm is created. A sketch of the cross-sectional view of its working principle is shown in Fig. 2.10

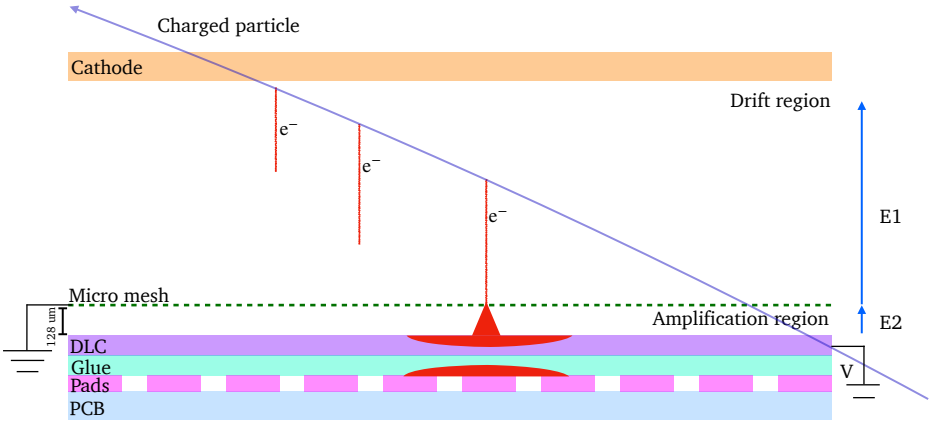

Figure 2.10.: Sketch of the working principle of the resistive Micromegas detector.

With the high suppression of the transverse diffusion in strong magnetic fields, as explained in Sec. 2.2.1, the ionization charge clusters arriving at the pad plane would be confined to a single pad, resulting in a loss of resolution. However, the spread of the signal over several pads perpendicular to the track yields a more accurate centroid determination.

A disadvantage of the DLC method is that the uniformity of the resistivity and capacitance across the anode surface is technically challenging, leading to inaccuracies of up to 30% [131]. An innovative method to produce a spread of the charge among neighbouring pads is the capacitive sharing [132]. This method consists of a stack of layers of pads, arranged in such a way as to make the size of the pads in a given layer half the size of the pads below, as seen in Fig. 2.11. The induced signal from the micromegas amplification is then transferred by capacitive coupling from one layer to the next. The use of the DLC becomes purely protective, as one is therefore able to increase the foil resistivity to 10–20 MΩ. In addition to being simple to produce, the main advantage of the technology is that the spatial resolution is kept in the order of ∼100 μm with a lower number of readout channels needed.

2.3. Signal acquisition

2.3.1. Signal induction: The Ramo theorem

The signal usually consists of a short current pulse since a static charge is not measurable. Ramo's theorem [133] provides a method to calculate the current i induced in the readout pads by the movement of the charge:

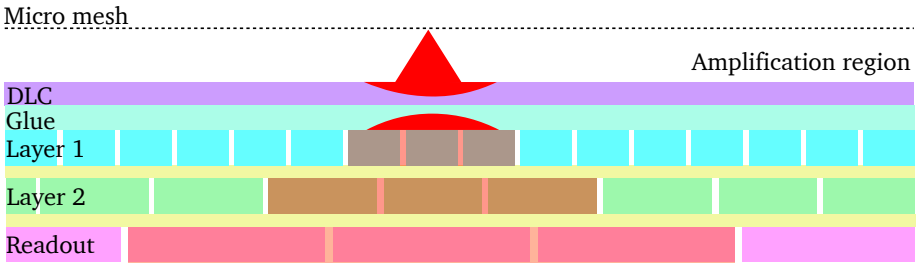

Figure 2.11.: Charge sharing with the capacitive coupling method.

$$i(t) = q\vec{E}_w\vec{v},$$

where q is the charge of the carrier, $\vec{v}$ is the instantaneous velocity and $\vec{E}_w$ is the *weighting field*. The weighting field is the component of the electric field which would exist in the direction of $\vec{v}$ at the charge's instantaneous position fulfilling the following requirements:

- The voltage in the electrode of interest is set to 1V.
- The rest of the electrodes are set to ground.

If the position of the carrier is determined following the field lines of the real field $\vec{E}$, then the time profile of the induced current (or charge) can also be traced out to determine the shape of the pulse.

As an illustration of the theorem, let us consider the simple scenario of an electron-ion pair immersed in a uniform electric field $\vec{E}$ produced by parallel plates (see Fig. 2.12).

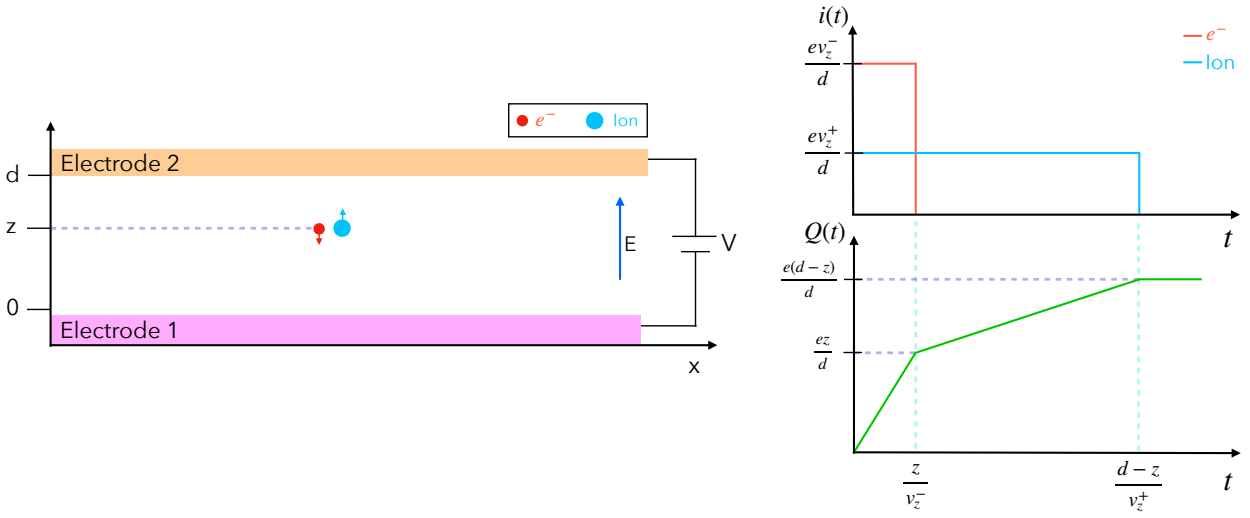

Figure 2.12.: Left: Electron-ion pair in a uniform electric field. Right: Current (top) and charge (bottom) induced in *Electrode 1* by an electron-ion pair.

The weighting field for Electrode 1 would be

$$\vec{E}_w^{(1)} = \frac{\hat{e}_z}{d},$$

and therefore, the total induced current is

$$i_1(t) = \begin{cases} e\frac{v_z^-}{d} & \text{if} \quad t \leq \frac{z}{v_z^-} \\ \\ e\frac{v_z^+}{d} & \text{if} \quad \frac{z}{v_z^-} < t \leq \frac{d-z}{v_z^+} \end{cases} \tag{2.7}$$

where v_z^+ and v_z^- are the drift velocities of the ion and the electron, respectively. Similarly, the charge collected is given by

$$Q(t) = \frac{e(d-z)}{d} + \frac{ez}{d}.$$

Because of their mass difference, the signal induced by electrons is $\times 1000$ faster than that of the ions (see right side of Fig. 2.12). In the first case, it corresponds to a short pulse of large amplitude, while the ions produce a long and lower signal. In fast detectors, the signal detected in gas detectors is typically induced by the electrons. However, if the integration time of the electronics is >150 ns, both contributions are integrated and the ions contribute equally to the amplitude of the signal.

2.3.2. Readout electronics

The electronic components for the extraction and acquisition of the signal follows a general scheme that can be tuned to optimize the observables desired. Figure 2.13 shows the minimal scheme required to readout a physical signal.

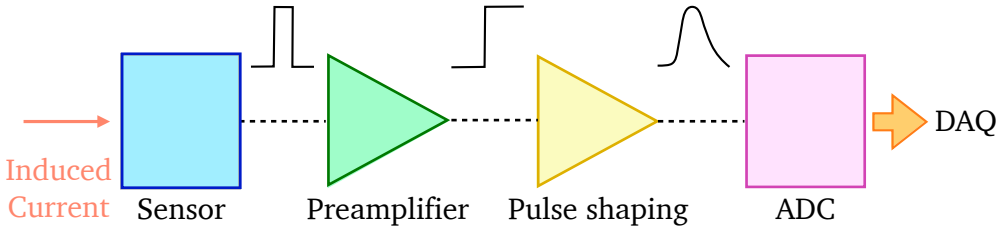

Figure 2.13.: Typical components used for the readout of the signal. See text for details. Figure inspired from [134].

The induced signal on an electrode (a pad of the TPC) is usually fed into a preamplifier since the amount of charge created is small with respect to the electronic noise (which is often the case in gas detectors, see Sec. 2.2.4). Next, a pulse shaper is used. Its main purpose is to set the bandwidth of the system and limit the duration of the pulse which sets the maximum signal rate allowed by the system. The shaping time must be matched to the duration of the signals: Otherwise a portion of the signal might be lost (if it's too short) or degraded (if it's too long). Finally, the shaped signal is digitized by a sampling in an analog-to-digital converter (ADC) for subsequent storage and analysis. The analog to digital conversion time is what drives the dead time of the readout. A commonly used front-end readout in TPCs, the STAGE chips integrated into the ARC card [135], converts the analog signal into digital format using a 4 channel, 25 MHz 12-bit multi-channel analog-to-digital converter, meaning a dead time in the order of microseconds. Once the digital conversion is finished, the signal is sent to a Data Acquisition system (DAQ) in a computer, where it is stored and analysed.

2.3.3. Noise

The acquired signal is superimposed with noise. Understanding the nature of the random fluctuations in a signal and tune the setup to minimize it, determines the quality of the signal and accuracy of the measurements.

If one considers the current induced in an electrode by n electrons, as defined in eq. (2.7), its fluctuation is given by

$$\langle \Delta i \rangle^2 = \left(\frac{ne}{d} \langle \Delta v_z^- \rangle \right)^2 + \left(\frac{ev_z^-}{d} \langle \Delta n \rangle \right)^2 .$$

The first term corresponds to the drift velocity fluctuations due to thermal excitations, that define the *thermal noise* (see Sec. 2.2.1).

The second term is the *shot noise*, which describes the fluctuation of the number of electrons through the readout electronics system. Since none of these processes have a frequency dependence, they are white noise sources.

The noise of the preamplifier is particularly important as it affects the ultimate resolution of the detector [95]. In particular, to optimize the counting rate, the thresholds should be set above the noise (3-5 sigmas). If the noise is too high, one might cut the signal on some pads and therefore lose resolution. The electronics noise is usually quantified in terms of its equivalent noise charge (ENC). The ENC is defined as the signal amplitude after the preamplifier that makes the signal-to-noise ratio equal to one [112].

In a simplistic manner, one can think of the detector as a capacitor C_d in which the induced charge is modified as the electrons and ions drift through the gas. For an input resistance R_i and capacitance C_i, the time constant for discharging the sensor is $\tau = R_i(C_d + C_i)$. If τ is large compared to the signal pulse time, the charge will be integrated on the input capacitance and the signal voltage V_s. In this case, $V_s = \frac{Q_s}{C_i + C_d}$. Therefore, the signal-to-noise ratio of the detector, assuming a noise voltage V_n is

$$\frac{V_s}{V_n} = \frac{Q_s}{V_n(C_d + C_i)}. \tag{2.8}$$

Relation 2.8 evidences the inverse proportionality of the signal with the system's capacitance. Since the transportation of the signal from the detector to the preamplifier is carried through coaxial cables which introduce an additional capacitance that increases linearly with length, it is good practice to place them as close as possible as to improve the signal-to noise-ratio. In the case of PUMA, where 1.3 m long cables are used, a capacitance of 80pF is expected to produce a noise level of 1200 electrons rms (see Ch. 5).

3. Simulations

3.1. Overview of the simulation package

The geometrical acceptance as well as the detection efficiency of the TPC was optimised. To that end, simulations of the setup with realistic annihilation events have been carried out using the Geant4 toolkit [136], followed by the analysis of the simulated data with the ROOT framework [137]. The overall procedure can be divided into four main stages:

- The generation of realistic events following experimental branching ratios of the possible decay channels of a nucleon / antiproton annihilation.
- The implementation of the realistic setup and detector components.
- The electrons' drift, amplification and collection of the signal in the pad plane.
- The identification of the charge of the pions by the bending of the tracks in the magnetic field. The tracking algorithm is based on the method validated by the MINOS collaboration [100, 138].

Each of these stages are further detailed in the following subsections.

Setup and Event Generation

Each event produced in the simulation consists of a set of pions randomly generated according to the measured branching ratios of antiproton–neutron [66] and antiproton–proton [67] annihilations. A typical event is composed of three charged pions in average, where the most probable branching ratios are $1\pi^+1\pi^-3\pi^0$ (23.3%), $2\pi^+2\pi^-1\pi^0$ (19.6%) and $2\pi^+2\pi^-2\pi^0$ (16.6%) for a $\bar{p}p$ reaction, and $2\pi^-1\pi^+k\pi^0(k>1)$ (39.7%), $2\pi^-1\pi^+1\pi^0$ (17%) and $3\pi^-2\pi^+1\pi^0$ (12%) for a $\bar{p}n$ annihilation (see Tab. 3.1). The reaction channels in which only π^0 particles are produced, that amount to 3% of the total branching ratios of the antiproton-proton annihilations, have not been taken into account.

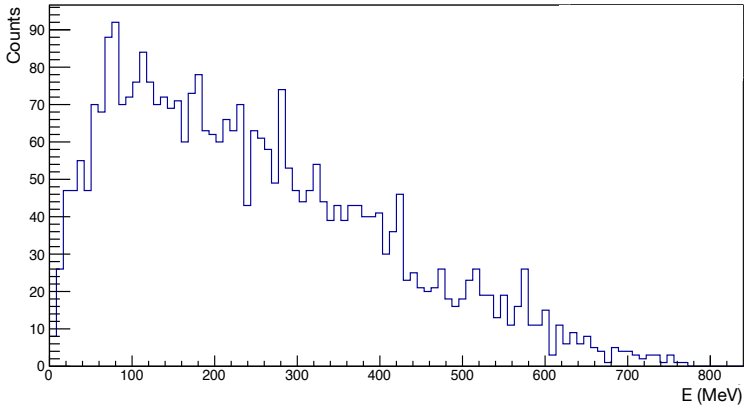

Figure 3.1.: Kinetic energy distribution of charged pions at the vertex before final state interactions.

Table 3.1.: Pion final states for antiproton-neutron [66] and antiproton-proton [67] annihilations. Not all decay channels are shown and the total sums of the above branching ratios do not reach 100%.

antiproton-proton		antiproton-neutron	
Pion final state	Branching	Pion final state	Branching
$\pi^+\pi^-$	0.0032	$\pi^-\pi^-\pi^+\pi^0$	0.17
$\pi^+\pi^-\pi^0$	0.069	$\pi^-\pi^-\pi^+k\pi^0(k>1)$	0.397
$\pi^+\pi^-\pi^0\pi^0$	0.093	$\pi^-\pi^-\pi^-\pi^+\pi^+$	0.042
$\pi^+\pi^-\pi^0\pi^0\pi^0$	0.233	$\pi^-\pi^-\pi^-\pi^+\pi^+\pi^0$	0.12
$\pi^+\pi^-\pi^0\pi^0\pi^0\pi^0$	0.028	$\pi^-\pi^-\pi^-\pi^+\pi^+k\pi^0(k>1)$	0.066
$\pi^+\pi^-\pi^+\pi^-$	0.069	$\pi^-\pi^-\pi^-\pi^-\pi^+\pi^+\pi^+k\pi^0(k\geq 0)$	0.0035
$\pi^+\pi^-\pi^+\pi^-\pi^0$	0.196		
$\pi^+\pi^-\pi^+\pi^-\pi^0\pi^0$	0.166		
$\pi^+\pi^-\pi^+\pi^-\pi^0\pi^0\pi^0$	0.042		
$\pi^+\pi^-\pi^+\pi^-\pi^+\pi^-$	0.021		
$\pi^+\pi^-\pi^+\pi^-\pi^+\pi^-\pi^0$	0.019		

The total kinetic energy that satisfies energy conservation is isotropically shared among final–state pions. The energy distribution of the pions at the creation vertex, obtained from the simulation, is shown in Fig 3.1. The most energetic pions reach up to 800 MeV while the most probable kinetic energy is in the 100-200 MeV range. The final state interaction with the residual nucleus is not considered in these simulations.

To accurately reproduce the experimental conditions, the different components of the setup in the collision zone are simulated following the properties detailed in Tab. 3.2.

Table 3.2.: Material budget of the inner tube, the TPC and the plastic scintillators.

Piece	Material	Density [g/cm^3]	Thickness [mm]	Rad. len. [mm]	Rad. len. [%X0]
Trap	Cu	8.96	4	14.3	27.9
Cryostat	Cu	8.96	0.75	14.3	5.2
70 K shield	Al	2.50	1	88.9	1.12
300 K vacuum pipe	Al	2.50	5	88.9	5.62
Insulator	Polyimide	1.42	4×0.02	285	0.02
Field cage outer structure	PCB	1.8	1.5	280	0.53
Field cage inner structure	PCB	1.8	0.3	280	0.1
Field Cage Air gap	Air	1	11	3.039×10^5	0.003
Gas mixture	$ArCF_4Iso$	0.0019	53 - 55	1.07×10^5	0.05
Insulator	Mylar	1.4	0.02	285	0.007
Scintillator wrap	Teflon	0.38	1	158	0.63
Scintillator	PVT	1.032	4	425	0.9

Fig. 3.2 shows the kinetic energies of the detected pions at the first interaction point with the gas mixture in the TPC (blue curve) compared to that at the creation vertex (red curve).

As opposed to Fig. 3.1, the pions that contribute to the vertex counts in this case are only those that are later detected in the TPC. In this way it is possible to compare directly the influence of the setup on the pions energy. The sharp energy rise of the pions at $\sim$40 MeV at the vertex gives a notion of the minimum energy required to reach the detector in the first place. Lower energy pions are

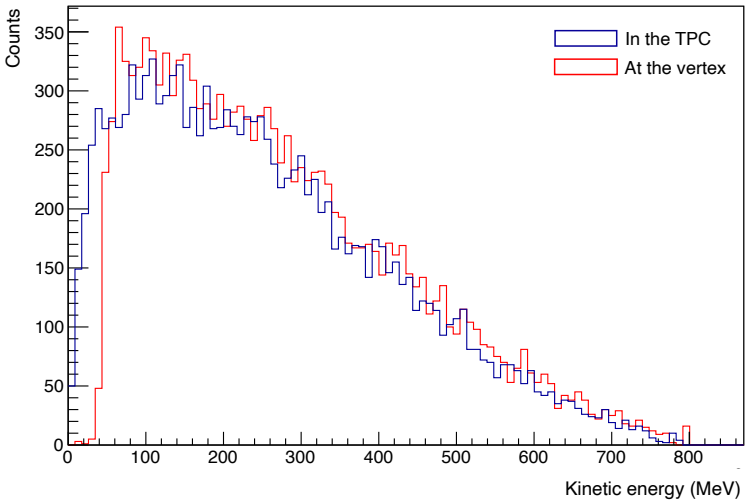

Figure 3.2.: Kinetic energy distribution of charged pions at the vertex before final state interactions, compared to the kinetic energy at the first interaction point with the gas in the TPC.

either stopped in the setup or their curvature radius due to the Lorentz force is smaller than the internal radius of the TPC. The inner tube in which the TPC is inserted has a radius of 50 mm. This means that any pion with a kinetic energy $\leq$6.8 MeV does not exit the tube, which accounts for 1.5% of the pions. In addition, the sensitive gas begins only 12 mm (radially) afterwards. This additional length increases the minimum kinetic energy to reach the gas to 12.4 MeV, corresponding to 3.2% of the total charged pions produced.

Upon reaching the sensitive gas, the pions suffer an energy loss. This is observed in the low energy shift between both curves, of the order of 30 MeV, although the most probable energy remains in the 100 MeV range.

After an event is generated in the trap, the energy loss of the pions within the sensitive gas (10–15 keV with a track-length of $\sim$15 cm, as calculated with Geant4) and the interaction points of the particles in the gas are saved. A production cut of 0.01 mm inside the TPC was chosen to smooth the energy loss and avoid clusters. This information is then used as input to implement the primary electron generation and drift. Fig. 3.3 presents a typical event in the collision trap surrounded by the TPC and the plastic barrel.

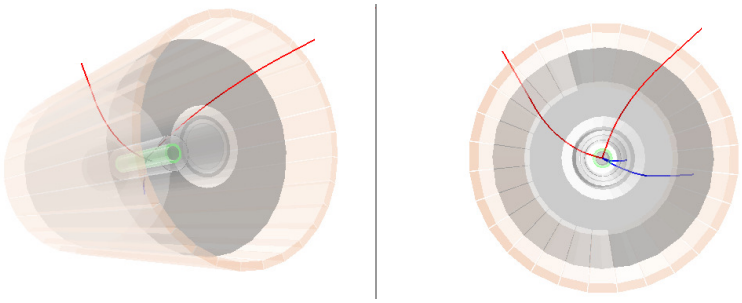

Figure 3.3.: Typical event simulated with the Geant4 toolkit, where the green region corresponds to the annihilation region and the pink bars are the plastic barrels. The blue curve corresponds to a π^+ and the red ones to π^-.

3.1.1. Generation and drift of electrons

The number of primary electrons created in a given interaction point (x_0, y_0) is randomly generated following a Gaussian distribution centered at $\mathrm{N_e} = \Delta\mathrm{E}/w$, where $\Delta\mathrm{E}$ is the computed energy loss and w is the average energy needed to produce one electron-ion pair.

The drift of the electrons throughout the gas, from the creation point (x_0, y_0, z_0) to the anode plane, is influenced by the gas properties, electric field and magnetic field, as described in Sec. 2.2.

In the plane transversal to the drift (x, y plane) the final position of the electrons follows a gaussian distribution given by

$$P_i = \frac{1}{\sqrt{2\pi}\sigma_T} e^{-\frac{(i-i_0)^2}{2\sigma_T^2}},$$

where the index i corresponds to the x and y axis and the dispersion is $\sigma_\mathrm{T} = D_T\sqrt{z_0}$, where D_T is the transverse diffusion coefficient. Similarly, along the drift direction (z axis):

$$P_z = \frac{1}{\sqrt{2\pi}\sigma_L} e^{-\frac{(z-z_0)^2}{2\sigma_L^2}},$$

where the probability distribution contains, instead, the longitudinal diffusion coefficient D_L, with the corresponding dispersion $\sigma_\mathrm{L} = D_L\sqrt{z_0}$.

The transport parameters used in this simulation (namely the drift velocity, D_T and D_L) were calculated beforehand with Magboltz [139] in the conditions of the experiment for different gas mixtures (see Sec. 3.3)).

After simulating the drift, the amplification of the signal is implemented. The avalanche effect is a statistical process in nature, meaning that the gain produced in the amplification stage fluctuates around a mean gain $\bar{G}$. The distribution that describes this process is the Polya distribution [140], given by

$$P_G(G/\bar{G};\theta) = \frac{(\theta+1)^{\theta+1}}{\Gamma(\theta+1)} \left(\frac{G}{\bar{G}}\right)^{\theta} \exp\left(-(\theta+1)\left(\frac{G}{\bar{G}}\right)\right),$$

where Γ is the Gamma function and θ a parameter usually set to $\theta \sim 1$. In the simulation, a gain with a mean value corresponding to the expected gain for each gas mixture considered was included (see Sec. 3.3). These values are calculated with Magboltz and vary in the range of $10^3 - 10^4$, depending on the gas.

For these simulations, the anode plane is segmented into rectangular pads of constant area (see Sec. 5.2) in which the response of the electronics system is simulated. The model used was developed and validated in the MINOS experiment [100]. White noise corresponding to the electronics intrinsic noise as well as the noise produced by a cable length of 1 m was added (see Sec. 2.3.2), with a detection threshold five times larger, estimated in 2500 electrons. An example of the waveform in a pad as a function of time is shown in Fig. 3.4.

3.1.2. Tracking method

The correct determination of the charge of the pions is key to determine which type of nucleon was annihilated on the surface of the nuclei ($\bar{p}p$ or $\bar{p}n$). Charged particles in an electromagnetic field have a curved trajectory following the Lorentz force

$$\mathbf{F} = q(\mathbf{E} + \mathbf{v} \times \mathbf{B}).$$

If a uniform magnetic field $\mathbf{B}$ perpendicular to the velocity $\mathbf{v}$ of the particle is applied, then the force $\mathbf{F}$ will be orthogonal to both quantities at each instant, making its trajectory circular in the

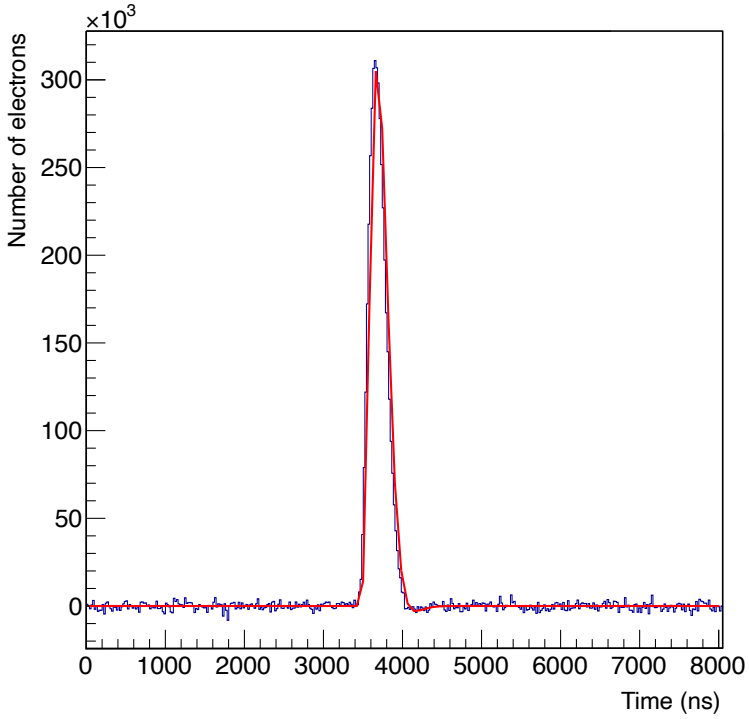

Figure 3.4.: Simulated signal waveform in a pad.

plane perpendicular to the **B** field. The direction of motion will only depend on the charge q of the particle, making it possible to differentiate π^+ from π^-. The assumption of a constant 4 T B field parallel to the E field is justified by the requirements and measured values of the PUMA solenoid (homogeneity better than few percent in the drift region - see [28]).

For this reason, a track reconstruction software to determine the direction of the particle's trajectory in the XY plane is implemented. To that end, each track is fitted with the circle equation using the MINUIT tool with the MIGRAD minimizer [141]: The data points considered are the center of each pad that was hit weighted by the charge it collected. An additional constraint for the minimization is that the track should arrive from the center of the trap, meaning that the XY origin is an extra point added to every track as initial guess.

To determine the charge, a straight line between the fired pads of closest and farthest distance from the inner radius of the TPC is created (see left side of Fig. 3.5). Thereafter, a vector perpendicular to the line pointing towards the farthest fired pad is produced. The direction of this vector (to either side of the straight line) determines the charge of the track.

Figure 3.6 shows an example of a fitted track in 2D. In this simulation, the gain is 10^4, corresponding to a field strength of 45 kV with Ar:CF_4:C_4H_{10} / 82:15:3 gas mixture.

With this approach, it is possible to obtain 95% of charge identification efficiency (see Sec. 3.2). There are three types of tracks in which this method does not work: on the one hand, energetic pions that produce straight tracks. In the second case, pions that fire less than four pads, therefore not having enough points to determine a direction of curvature. In the third case, a small percentage of low-energy pions do not exit the detector and instead return back to the trap. In these case the 2D charge reconstruction becomes unreliable (see left-hand side of Fig. 3.7). These correspond to 2.2% of the charged pions that reach the detector's sensitive gas, with a maximum kinetic energy of 21 MeV at this stage. The timing information was therefore used to determine the charge of the tracks, where the position in the axial direction (Z) was extracted using the known drift velocity (4.38 mm/μs). The same track is shown in the right-hand side of Fig. 3.7, where the trap (in green)

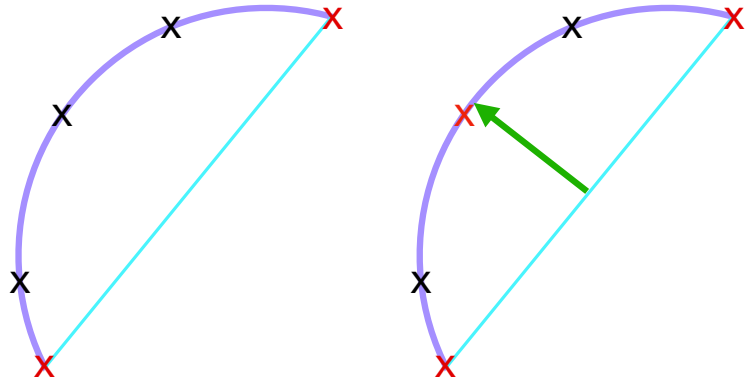

Figure 3.5.: Procedure to determine the charge of the pions. Left: Circular fit of fired pads (crosses) and straight line creation from both ends of the track. Right: vector perpendicular to the line pointing to the farthest pad from the line. The direction of the vector determines the charge of the pions.

was included to facilitate the visualization.

With this method in place, the three-steps Monte-Carlo simulation is run systematically to optimize different parameters of the Time Projection Chamber, as detailed in the following.

3.2. Dimensioning of TPC

The TPC external radius R, its length L and the pads shape and size were studied to optimize the detector geometry.

The total detection efficiency is defined as

$$\varepsilon_{\mathrm{tot}} = \varepsilon_{\mathrm{TPC}} \cdot \varepsilon_{\mathrm{ID}}$$

where $\varepsilon_{\mathrm{TPC}}$ corresponds to the ratio of pions that are within the TPC's geometrical acceptance and not absorbed by the surrounding materials over the total number of charged pions generated after an annihilation. The charge identification efficiency, $\varepsilon_{\mathrm{ID}}$, is the ratio of charged pions whose charge is correctly identified by the analysis software over the total number of charged pions detected by the TPC.

3.2.1. TPC length

Figure 3.8 displays the efficiencies $\varepsilon_{\mathrm{tot}}$ (triangles), $\varepsilon_{\mathrm{TPC}}$ (squares) and $\varepsilon_{\mathrm{ID}}$ (circles) obtained as a function of the length of the TPC after the simulation of 1500 events, corresponding to roughly 3500 charged pions. The material from which the trap is made of as well as the rest of the components surrounding the trap, described in Tab. 3.2 were simulated. The external radius of the TPC used for this simulation was R=120 mm and a point-like plasma cloud was used. At this stage, the pads were simulated with a rectangular shape of 3 mm of height and 2 mm of width.

In this case, the acceptance of the TPC (depicted by the blue curve) increases sharply up to an efficiency of 0.75 at 300 mm - the chosen length for the detector - and remains stable afterwards. The accurate identification of the charge (green curve) is not affected by this parameter, as the length of the tracks remains constant.

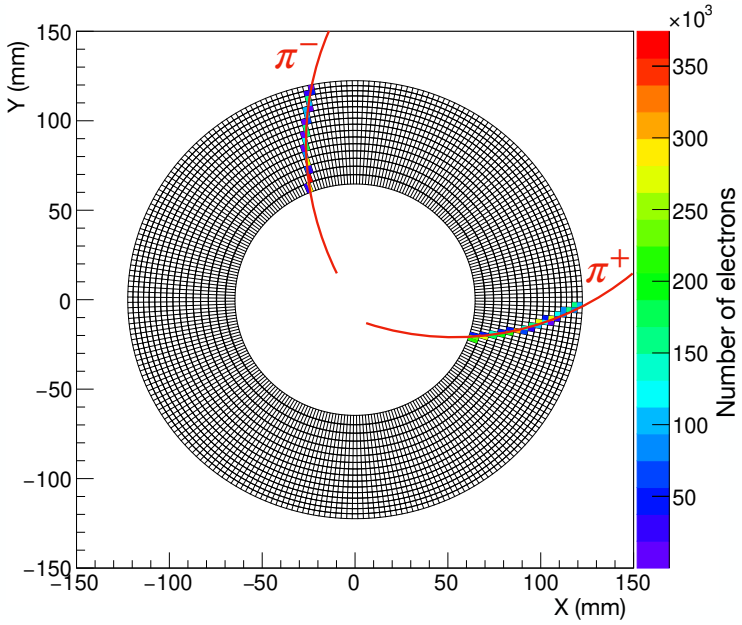

Figure 3.6.: Two-dimensional charge collection distribution of two tracks after the drift of electrons following an event. The red lines represent the fitted curves (a section of a circle) of the tracks. See text for details.

3.2.2. TPC external radius

The TPC's internal radius is fixed by the dimensions of the trap, thermal screens and vacuum tube at $R_{int} = 51$ mm. Additionally, another 13 mm are needed to accommodate the TPC's field cage (see Ch. 4), placing the inner radius of the TPC's sensitive volume at $r_{int} = 64$ mm. Optimising the detection efficiency as a function of its external radius is relevant for the determination of the magnet's bore radius and the thickness of the plastic barrel.

Figure 3.9 shows the efficiencies obtained in the same conditions as for the length study, fixing the TPC's length at L=300 mm. The blue curve (squares) corresponds to the aforementioned $\varepsilon_{\mathrm{TPC}}$ which, as expected, remains constant: The absorption probability of a pion depends only on the materials the particle traverses during its path towards the TPC sensitive gas, and the geometrical acceptance only depends on its length.

An increase is observed in the charge identification efficiency $\varepsilon_{\mathrm{ID}}$ (circles) due to the increase of the track's length as the radius enlarges. A plateau is reached at R$\sim$120 mm, which determines the minimum radius that ensures the maximum efficiency. Considering the additional space needed for the mechanics, electronics and the plastic scintillators, the magnet's bore was then set to 140 mm radius.

3.3. Gas Choice

The selection of the gas is a defining feature of the detector's performance and several aspects need to be considered. Three candidates are compared (Fig. 3.10 and Fig. 3.11). All the mixtures are Argon based because of its low ionization energy ($\sim$25 eV) and low cost. One of the mixtures contains Carbon tetrafluoride (CF_4) (usually used to attain a higher drift velocity [100, 142]) and isobutane as a quencher, while the other two use carbon dioxide, instead. In addition, one of the mixtures include a small percentage of methane (CH_4) which modifies slightly the drift velocity and electron

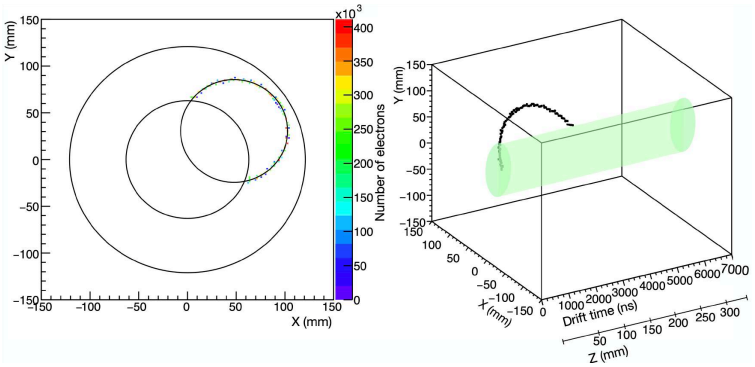

Figure 3.7.: Left: 2D projection of a track fitted with a circle, whose charge cannot be determined on the basis of the 2D projection information only. Right: The extraction of the drift time is used to reconstruct the track, allowing to disentangle the charge of the pion.

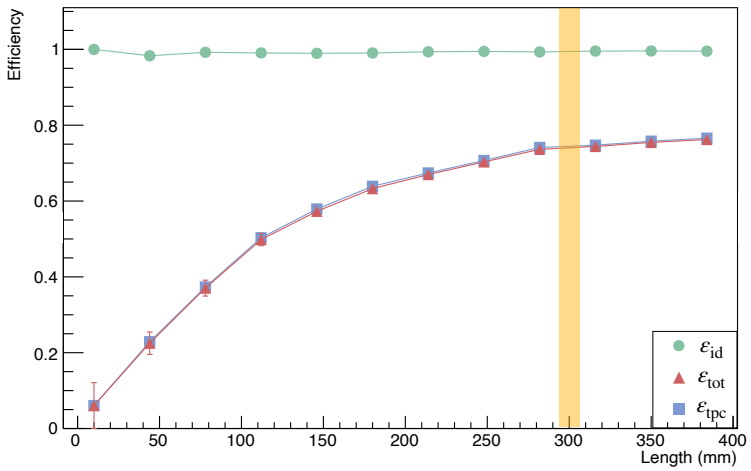

Figure 3.8.: Efficiencies $\varepsilon_{\mathrm{tot}}$ (triangles), $\varepsilon_{\mathrm{TPC}}$ (squares) and $\varepsilon_{\mathrm{ID}}$ (circles) as a function of the length of the TPC. The error bars correspond to statistical uncertainty from the simulation.

attachment, as observed in Fig. 3.10. The simulations shown in this figure were produced with MAGBOLTZ considering a temperature of 295 K and a pressure of 1 atm.

The drift velocity need to comply with the detector's drift length, electronic's readout frequency and the rate of events. In the case of PUMA, the drift velocity is not a defining factor since a maximum rate of events of 100 Hz is expected when stable isotopes are studied (and it will decrease in the case of exotic ions). This low rate and the compact size of the TPC (300 mm of maximum drift length) allows to optimize other properties of the gas. Importantly, the nominal field at which the detector operates would ideally be set such that the drift velocity remains stable within small pressure fluctuations. This condition is met at the local maxima of each curve (left side of Fig. 3.10), obtained at 200-300 V/cm in the CO_2 mixtures while a field of 1000 V/cm would be needed in the third gas. Due to the constrained space and proximity to ground of the PUMA field cage (see Ch. 4), a lower operation field is preferred. Moreover, the gain in the three cases, given by $G=e^{\alpha x}$ is comparable although the CO_2 mixtures show a slight higher Townsend coefficient in the 10^4-10^5 V/cm region.

The electron attachment probability per unit length η is also highly suppressed in the CO_2 mixtures. This is also a desirable feature as the loss of electrons due to attachment reduces the signal.

The diffusion coefficients are considered in Fig. 3.11. Due to the high magnetic field of 4 T present in the TPC, the transverse diffusion coefficient D_T is suppressed in all cases. The charge is indeed

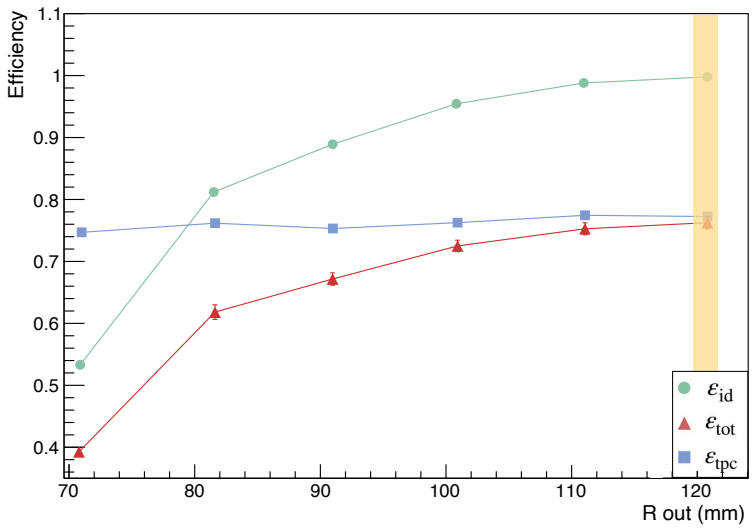

Figure 3.9.: Efficiencies $\varepsilon_{\mathrm{tot}}$ (triangles), $\varepsilon_{\mathrm{TPC}}$ (squares) and $\varepsilon_{\mathrm{ID}}$ (circles) as a function of the external radius of the TPC. The error bars correspond to statistical uncertainty from the simulation.

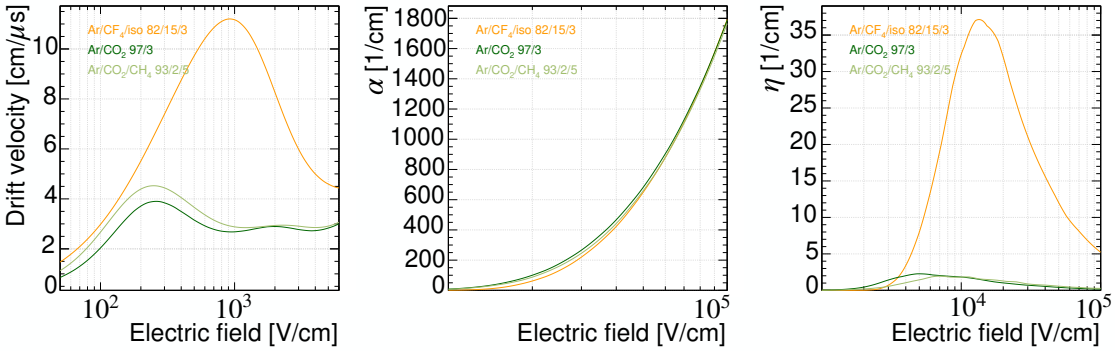

Figure 3.10.: Drift velocity, first Townsend coefficient and electron attachment as a function of the electric field of candidate's gas mixtures for the PUMA TPC.

foreseen to be diffused by the capacitive coupling method (see Sec. 2.2.4) before collection so as to improve the spatial resolution with a centroid determination. The longitudinal diffusion coefficient D_L impacts the TPC resolution in the drift direction. In the case of PUMA, however, its influence would be negligible due to the small size of the TPC (between 0.3 to 0.7 mm for half the drift distance -where the pions are produced-, depending on the gas).

The safety and environmental regulations are in place at CERN constrain the choices to gases that are non-flammable and that do not contribute to the greenhouse effect. This last regulation in particular requires the forbids the use of fluorine. In terms of flammability, Ar-CO_2 is non-flammable while CH_4 is non-flammable as long as it's present in less than 5% of the proportion [143].

It is therefore concluded that both gas mixtures based in Ar and CO_2 are adequate options for the PUMA TPC.

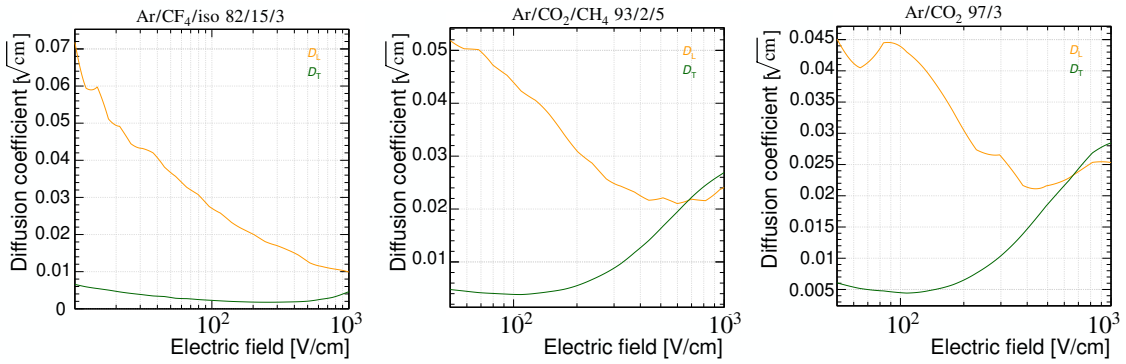

Figure 3.11.: Diffusion coefficients D_L and D_T of candidate gas mixtures for the PUMA TPC.

3.4. Background rejection

The influence of atmospheric muons in the experiment, product of cosmic ray showers in the atmosphere, is investigated. The PUMA concept is based on solely the detection of pions with no coincidence with recoil nuclei. Therefore, cosmic rays can in principle be a source of background which we wish to quantify with the chosen geometry. To this end, simulations with Geant4 are produced to determine their rate and the rejection capabilities of PUMA.

Event generator

The simulation of atmospheric muons is done integrating into Geant4 the Cosmic Ray Shower library (CRY) [144], in which cosmic ray showers are generated from data tables and show good agreement with cosmic rays measurements [145]. The library allows to choose a set of parameters (altitude, latitude and date -to account for the eleven year, sunspot cycle-) to adjust the particle distributions to the conditions in which the experiment will take place. Cosmic particles are generated in an area of 5×5 m^2 on top of the detector to allow a large angular acceptance. The cosmic muons arriving from the other side of the world are not considered since they are largely suppressed by the planet.

The latitude is set to Geneva (CERN location) and the year to adjust the Sun cycle is set to 2023.

Rate of atmospheric muons

The package needs the number of cosmic muons to be simulated as input, and the output includes their rate, angular distribution and energy.

From the simulations, the rate of muons expected to cross the TPC is $\sim$2 sec^{-1}. However, $\sim$90 $\%$ of them are rejected by adding the constraint that their track should also pass through the collision zone of the trap: In this case, after a simulation of 3 million muons, the expected rate is 8 ± 0.5 min^{-1}.

The total energy deposit per particle in the TPC is shown in Fig. 3.12, assuming a rate of 10 min^{-1} real events. Only the muons that cross the trap are considered for the comparison. In this case, the energy deposit of the muons is larger than that of the pions since their track is about twice as large.

A clear cut can be seen at $\sim$30 keV and only less than 1% of the pions will have an energy deposit in the TPC similar to the muons. In addition, muons will only pollute the channels of multiplicity M $= 1$ and 2, which represent 30% of the total branching ratios. Considering all of these factors, it is estimated that at least 99.7% of the muons will be rejected. The PUMA magnet is added to the simulation to investigate if the rates of muons are modified. Figure 3.13 shows the energy deposit in the TPC in the conditions where the magnet is present and when it is not. Additionally, the energy

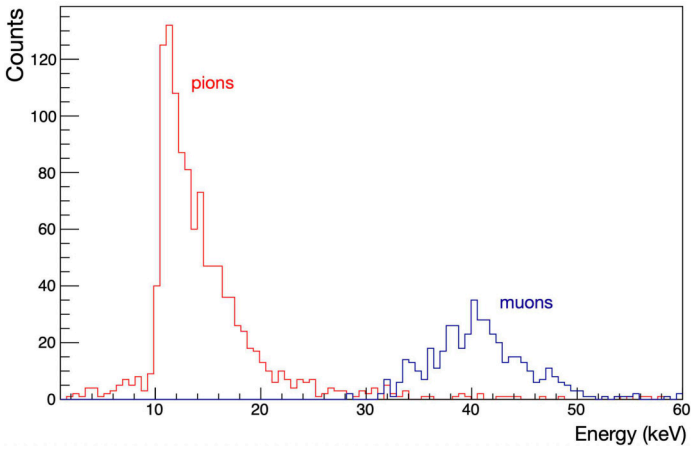

Figure 3.12.: Comparison of the energy deposit in the TPC by pions (red histogram) with respect to muons (blue histogram) traversing the trap.

deposit in the TPC of the proportion of muons that also traverse the trap is included. The result indicates that the magnet shows no effect in the rate of muons observed.

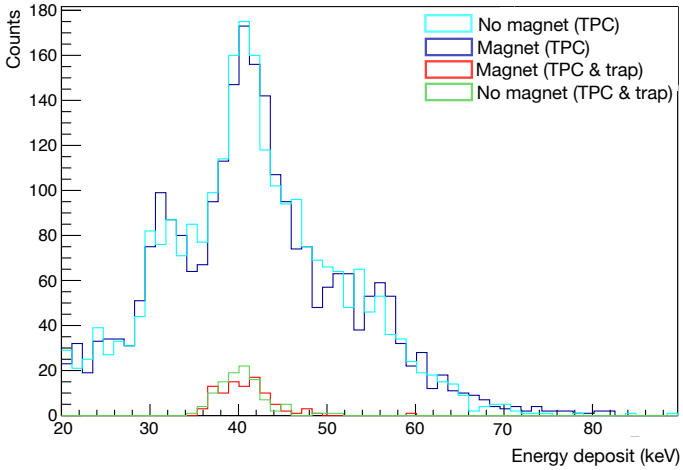

Figure 3.13.: Energy deposit in the TPC by muons. The red and green histograms correspond to the fraction of muons that traverse the trap.

4. Design of the Field Cage

The path of the primary electrons in the drift region can be altered by changes in the uniformity of the electric and magnetic fields, as well as variations in the gas properties (such as temperature, pressure, impurities). As such, not only a minimisation of these effects during the design phase of the TPC is required, but also a comprehensive understanding of these distortions, which introduce a systematic offset that will need to be corrected during the data analysis.

4.1. Uniformity of the fields

One of the main sources of distortions of the electric field uniformity is given by edge effects produced by the cathode and anode plates. The standard way of mitigating this effect to a first approximation is by introducing a field cage, which is nothing but a set of conductive rings, centred along the drift direction and connected to one another through a resistor chain. As a consequence, a linearly decreasing potential is created within which the electrostatic field lines show an overall straight path from anode to cathode in the active volume of the TPC.

To visualise this effect, Fig. 4.1 displays an electrostatic simulation of parallel plates in 2D, in which the difference in the potential contours created by adding and removing the field cage is evidenced.

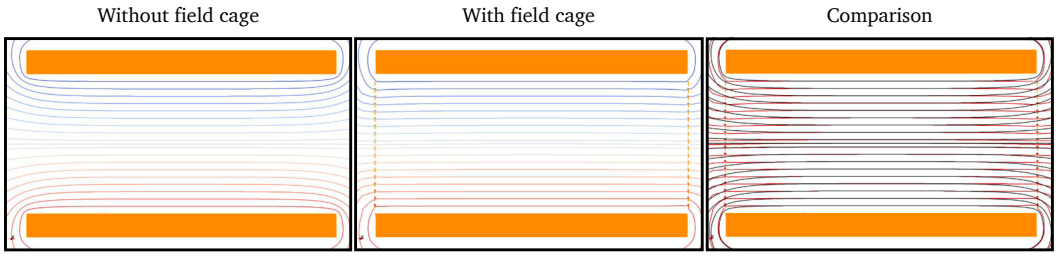

Figure 4.1.: Left: Potential lines in an electrostatics 2D-parallel plate simulation. Middle: A field cage is added to the setup. The contour lines are less distorted within the cage area. Right: Comparison of contour lines. The red contour lines correspond to the ones produced with the field cage while the black ones without it.

Because of the finite size of the strips and inter-strip distance, it is expected to see non-uniformities close to their boundaries. In order to avoid dead channels at the edges of the pad plane, product of these distortions, the design of the field cage, consisting mainly of the strips, the cathode and the anode is optimised.

The study of the field homogeneity is performed with the Finite Element Method (FEM), which consists of solving numerically a set of differential equations with given boundary conditions. To do that, the space where the solution is expected is subdivided in discrete elements, effectively forming a mesh interconnected at points common to two or more elements or boundaries. It is at these nodes that the field is explicitly calculated, and the solution of the full system is interpolated.

Because of the cylindrical symmetry of the PUMA TPC and to avoid large computation times, a 2-dimensional mesh consisting of the main components of the field cage is produced with the finite element mesh generator software, Gmsh [146]. To solve the Poisson equation, the mesh is introduced into Elmer FEM [147], an open source multi-physics solver. At this stage, the input consists of the boundary conditions (fixed potential of each electrode, the cathode, the anode and the grounds), together with the dielectric constants of the media where the field is to be solved.

The accuracy of the simulation depends significantly on the quality of the mesh [148]. One of the metrics used to evaluate the mesh elements is the aspect ratio, defined as the ratio of the shortest length to the longest length of one element. An aspect ratio closer to one implies a better quality element. Figure 4.2 shows the quality of the mesh elements produced for the simulation of the PUMA field cage, according to this metric. As it can be observed, the most frequent value corresponds to 1.1, while 90% of the elements are within the range <1.4, well below the typical "limit" of 4-5 to consider an element still acceptable [149].

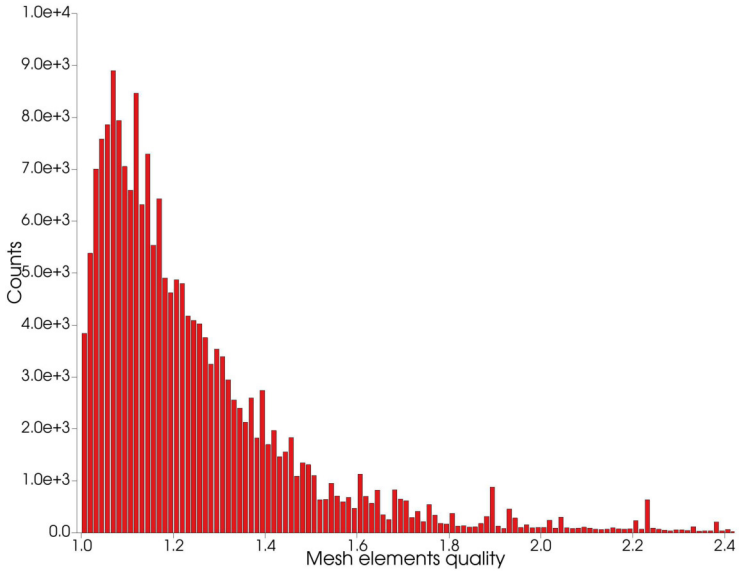

Figure 4.2.: Quality of the mesh elements according to the aspect ratio metric [150].

The output of the mesh generator and the electrostatic solver is shown in Fig. 4.3. The elements are refined in the regions where the field is expected to change abruptly and particularly in the vicinity of the strips, where the most accurate solution is desired.

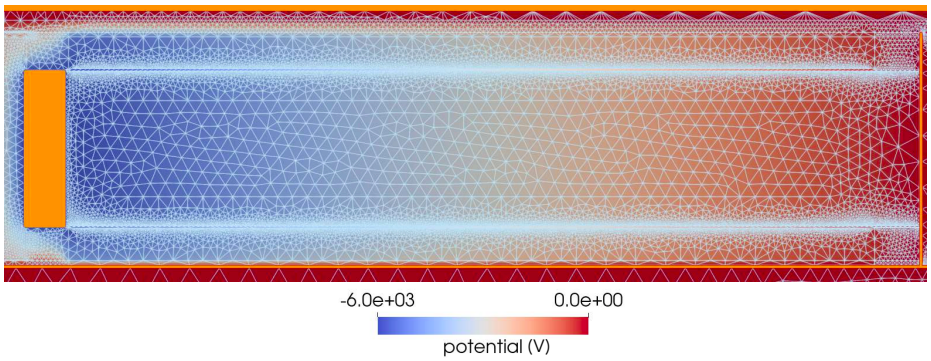

Figure 4.3.: Field cage mesh calculated with the Gmsh software using FEM and electrostatic field solved with ElmerFEM.

4.1.1. Field cage structure

As shown in Fig. 4.4, the structure of the field cage consists of a flexible PCB substrate, in which two layers of strips (one at each side of the PCB with an offset of half a pitch) of 1 mm long with a 0.5 mm separation are interconnected by a chain of 1 MΩ resistors. The strips are made of gold-plated copper and have a thickness of 50-80 μm with rounded edges to minimise edge effects. Two flexible PCBs (one for the internal radius of the TPC and another for the external radius) with the same disposition are used. An additional two PCBs separated by an 11 mm gap of air from the internal ones, provide the external structure of the TPC. The external structure is shaped in a 32-sided polygon in which the barrel of plastic scintillators sit.

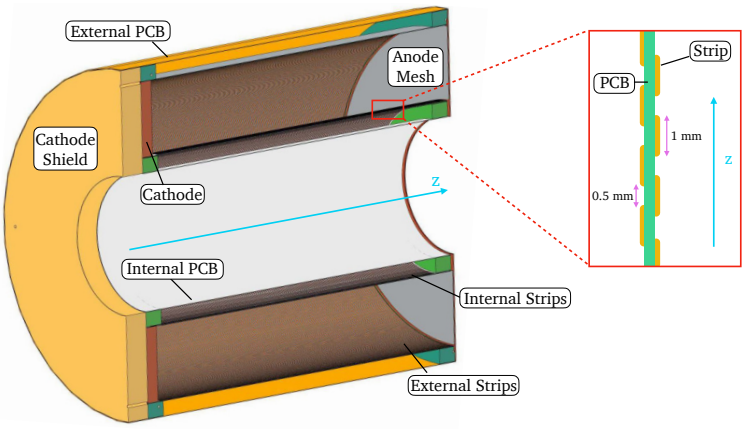

Figure 4.4.: Structure of the TPC's field cage. The inset shows the double layer of strips at each side of a PCB in the inner and outer radius of the active area. See text for details.

The main considerations to define the strip configuration are related to uniformity of the field and electrical protection against sparks. For instance, the two-layered PCB minimises field distortions in the inter-strip regions in the vicinity of the field cage. In the same way, the distance between the strips and the grounds can impact the uniformity of the electric field within the drift region. Figure 4.5 shows the potential lines produced by a smaller gap (5 mm) and the 11 mm separation from the ground.

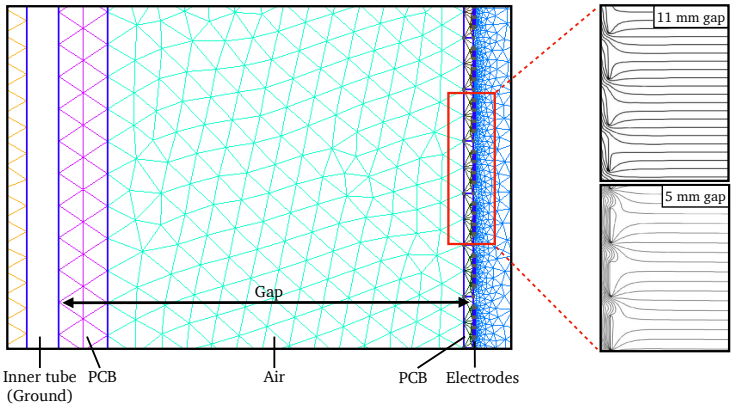

Figure 4.5.: Left: Triangular mesh. Insets: Contour lines produced by two different gap sizes (5 mm and 11 mm).

The distortion of the electric field near the strips is shown in Fig. 4.6. In this figure, each count corresponds to a node in the mesh where the field is calculated exactly. Similarly, each histogram

specifies the relative distortion within the radial boundaries specified, zero being exactly at the strips edge. As it can be observed, the field lines become less than 5% distorted within less than 1 mm away from the strips.

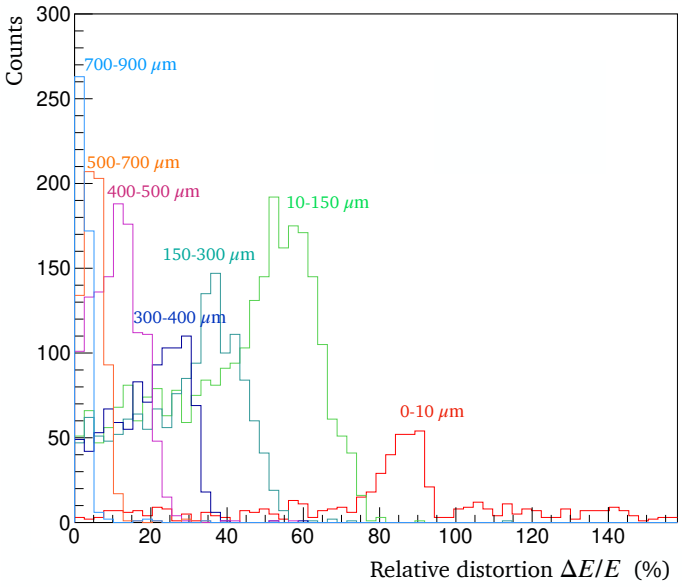

Figure 4.6.: Relative distortion of the electric field for different radial distances from the inner boundary of the field cage. See text for details.

4.1.2. Anode Side

One of the main challenges of the PUMA TPC is the field adjustment between the anode and the field cage. The homogeneity of the electric field near the pad plane is particularly relevant to avoid tracks distortions, electron loses and dead channels. In the case of PUMA, the anode is grounded and extended towards the outer structure of the field cage. The advantage is that the edge effects are shifted away of the active region and into the field cage inner layer structure, as seen in Fig. 4.7.

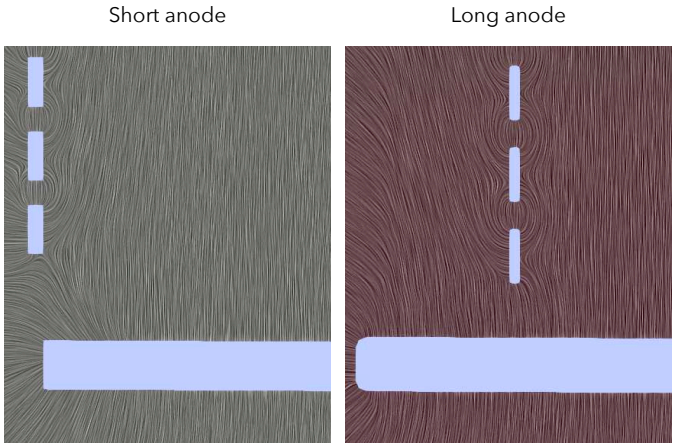

Figure 4.7.: Field lines produced by different anode lengths.

4.1.3. Cathode Side

The high tension applied to the cathode (-6 kV to obtain an operational field of 200 V/cm) presents . A thick cathode provides, on the one hand, stability for the mechanical elements (gas and high voltage connections) as well as the possibility of machining a larger radius of curvature.

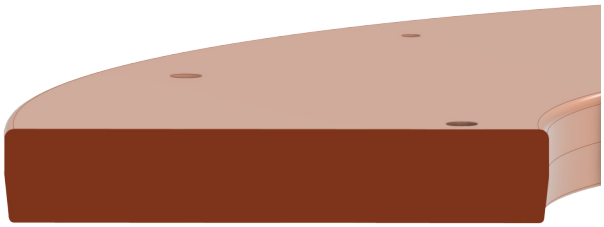

Figure 4.8.: Cathode shape of the PUMA TPC.

The proposed configuration is simulated and the results are shown in the following.

4.1.4. Electron drift simulation

A quantitative approach is developed to determine the drift direction of electron clusters in the experimental setup proposed. To that end, the software Garfield++[151] is used. This toolkit, based on the ROOT framework, is designed to simulate the tracks of particles in a gaseous medium. Once the gas composition is set, the program loads the collision rates corresponding to the selected gas from the database Magboltz [152] and modifies them to comply with the chosen extrinsic parameters (temperature and pressure).

The electrostatic field calculated with Elmer FEM, as well as the magnetic field map simulated for the design of the PUMA solenoid [28] are used as inputs. Additionally, a gas mixture of Ar/CF4/iso: 85/13/2 is used at ambient temperature and 1 atm pressure. Under these conditions, the drift velocity of the electrons is v_d=6.1 cm/µs, the transverse diffusion is 16.5 µm/$\sqrt{\text{cm}}$ and the longitudinal diffusion is 218.1 µm/$\sqrt{\text{cm}}$. In this case, Garfield++ transforms the 2D solution of the electrostatic field into 3D following the axial symmetry of the setup.

A point-like cloud of 1000 electrons is systematically created at different initial positions within the active volume of the TPC (x_i, y_i, z_i) and drifted following the Monte Carlo method: Each electron is tracked microscopically, where at each step there is a certain collision probability. Iteratively, the new electron energy and position is calculated. The final position of each group of electrons (x_f, y_f) when they arrive to the anode (z_f), is saved. Figure 4.9 shows the 2D distribution of the final position of the electron clusters, initially released at six different initial positions: The radial internal edge, external edge and middle at full drift length (x_i=68.5, y_i=285) mm, (x_i=90, y_i=285) mm and (x_i=119.5, y_i=285) mm, respectively, and the same radial positions, but for a short drift length: (x_i=68.5, y_i=10) mm, (x_i=90, y_i=10) mm and (x_i=119.5, y_i=10) mm, respectively.

Both simulations released at a radial distance of 90 mm show centred clouds that only differ in the size, product of the transverse diffusion which makes the cluster corresponding to the longer drift distance to be ∼10 times larger. In addition to the diffusion, the electrons released at the radial boundaries of the TPC show a collective deviation of <200 µm for the 'worst case scenario', where the electrons travel the full drift length of 285 mm.

To have a consistent metric of the electron cluster's deflection at different initial positions within

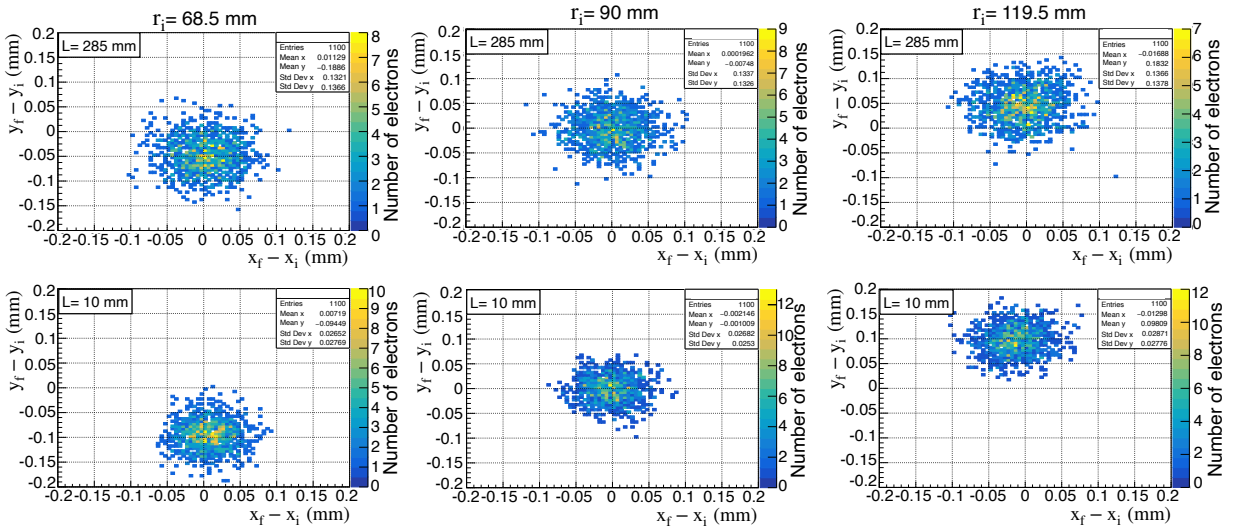

Figure 4.9.: Deflection of the electron cluster for different drift lengths along the radial direction of the TPC.

the sensitive volume of the TPC, the transverse deviation Δr given by

$$\Delta r = \sqrt{(x_f - x_i)^2 + (y_f - y_i)^2},$$

is used. Figure 4.10 shows the deflection of the electrons Δr with respect to the central position from which they were released, where each curve corresponds to a given drift length and the horizontal axis is the radial distance from the center of the TPC. The inner and outer radial boundaries of the field cage are specified with vertical red lines.

As it can be observed, the full drift region shows a deviation of $<$100 µm in more than 70% of the TPC volume, while the remaining percentage, at the edges of the cage, shows a deviation smaller than 200 µm. These values are to be compared with the pads size in the anode plane (see Sec. 5.2), which have an average value of 3×3 mm^2. Therefore, the impact of the deviation of the tracks due to the (ideal) field cage structure is negligible.

Simulations considering structural imperfections or realistic elements are detailed in the following.

4.1.5. Resistor Chain Homogeneity

The strips are interconnected through a chain of 200 resistors of 1 MΩ and imperfections in the resistors can then modify the expected field uniformity. To assess their influence, simulations including realistic resistors, with 0.1%, 0.5% and 1% precision have been carried out. In this case, a random value following a flat distribution is assigned within the corresponding tolerance to each resistor, and the corresponding potential drop is computed. Following the same method as in the previous section, the deflection Δr is calculated for the full drift length at the radial positions of 68.5 mm, 90 mm and 119.5 mm, corresponding to the radial boundaries and center of the TPC. Figure 4.11 shows the deviation as a function of the tolerances simulated, where the first points - at zero - correspond to the case of ideal resistors.

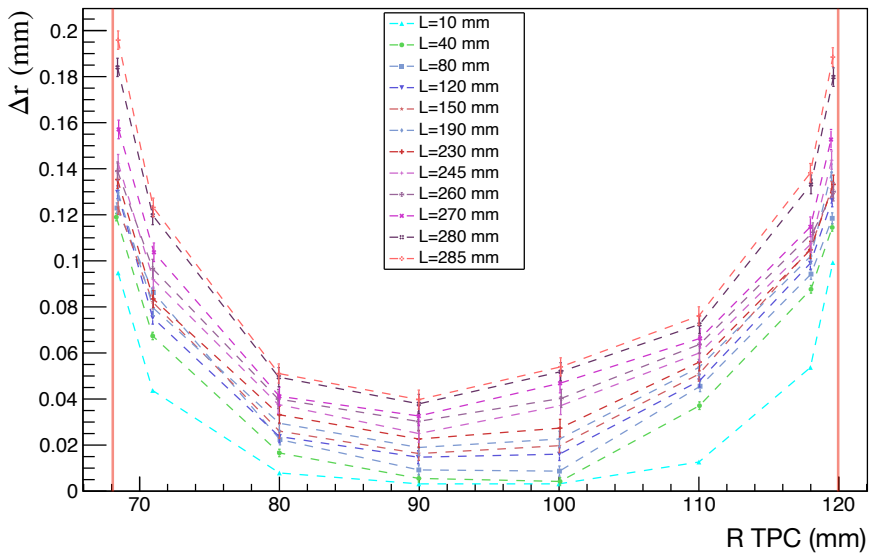

Figure 4.10.: Deflection of electron clusters for different drift lengths along the radial direction of the TPC. The vertical red lines correspond to the radial boundaries of the TPC.

The edges of the field cage, closer to the resistors, show a higher deviation as it was evident in Fig. 4.9, and the larger tolerance variation show a slight influence, where the variation with respect to the perfect resistors at 1% precision is less than 10%, while it increases up to 23% considering resistors with 5% tolerance. The center radial region of the TPC (green points) is not affected by this effect at these tolerance ranges.

4.1.6. Magnetic Field Homogeneity

The 4 T magnetic field in the PUMA experiment fulfils two different purposes: On the one hand, to trap axially the ions and antiprotons in the Penning traps and, on the other hand, to curve the track of the pions traversing the TPC in order to identify their charge due to the Lorentz force. For both these goals, the B field has been designed to have a uniformity better than 0.2% in the traps region and better than 5% within the full drift volume of the TPC [28]. Inhomogeneities and misalignments between the electric and magnetic field can lead to distortions, as detailed:

Fields Alignment

When the fields are not parallel, there is a distortion in the clusters, leading to inaccurate tracks reconstruction.

Figure 4.12 shows the deflection of electron's clusters in the middle region of the drift area. As observed, the alignment with a precision better than 0.1° would be desirable to ensure a deflection of less than 500μm due to the E×B effect.

Lorentz Angle

According to the Langevin equation (2.2), any non-parallel component between the electric and magnetic fields, modifies the electrons' drift velocity direction and magnitude, and its impact is therefore gas dependent. To drift velocity is then computed for the three candidate gases using Garfield++ as a function of the angle between the electric and 4 T magnetic field. For this calculation,

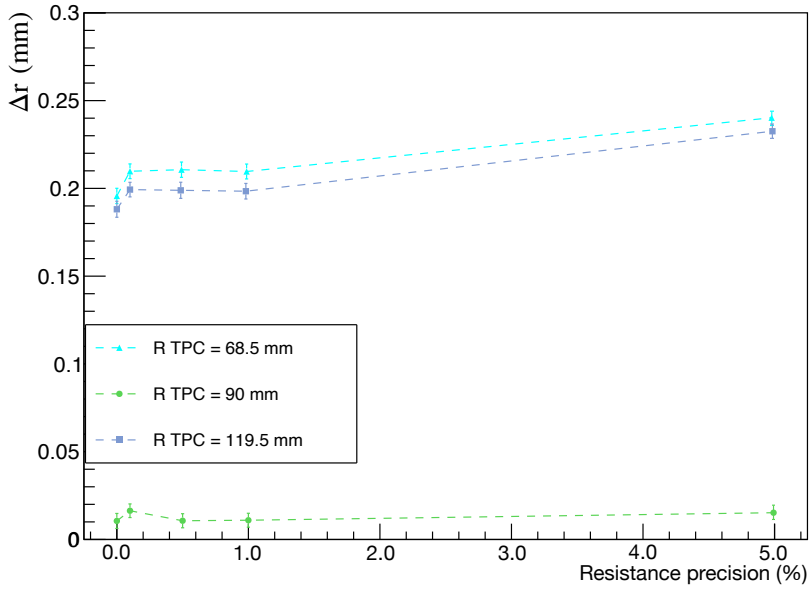

Figure 4.11.: Deviation as a function of the resistor's precision.

the expected nominal electric field of 200 V/cm was used. Figure 4.13 shows the components of the drift velocity v_E, v_B and $v_{E\times B}$, parallel to the electric field, to the transverse magnetic field and transverse to both, respectively.

As observed in this figure, the three gas mixtures show a similar behaviour in orders of magnitude. An angle of 0.1 rad, (5.7°) leads to a component of the drift velocity in the transverse magnetic field direction which is 1% of v_E. However, considering the constrain obtained of 0.1° found the previous section, this effect is negligible for the gas mixtures considered.

4.2. Electric Protection Design

The cathode is a disk at -6 kV placed in a compact space surrounded by ground: Internally, by the PUMA ultra high vacuum tube and, externally, by the bore of the 4 T magnet. As such, the field strength in this area presents a risk of sparks and care needs to be taken in order to ensure a stable and safe operation of the detector.

4.2.1. Breakdown Voltage

The phenomena of breakdown is attained when the electric field strength in a certain medium is sufficiently high as to produce a discharge. This process was investigated by F. Paschen, who developed an empirical law to determine the breakdown voltage in gases V_d, depending on their pressure p and the gap between the electrodes d, modelled by Eq. (4.1) [153]

$$V_b = \frac{Bdp}{\ln(Apd) - \ln\left(\ln\left(1+\frac{1}{\gamma_{se}}\right)\right)}, \tag{4.1}$$

where A and B are gas dependent constants determined experimentally, and γ_{se} is the secondary Townsend coefficient. This coefficient is the number of secondary electrons produced per electron in the primary avalanche [154].For air, as an example, A=112.5 (kPa cm)$^{-1}$ and B=2737.5 V (kPa cm)$^{-1}$. The breakdown voltage of air at 1– 4 bar as a function of the spacing between electrodes is

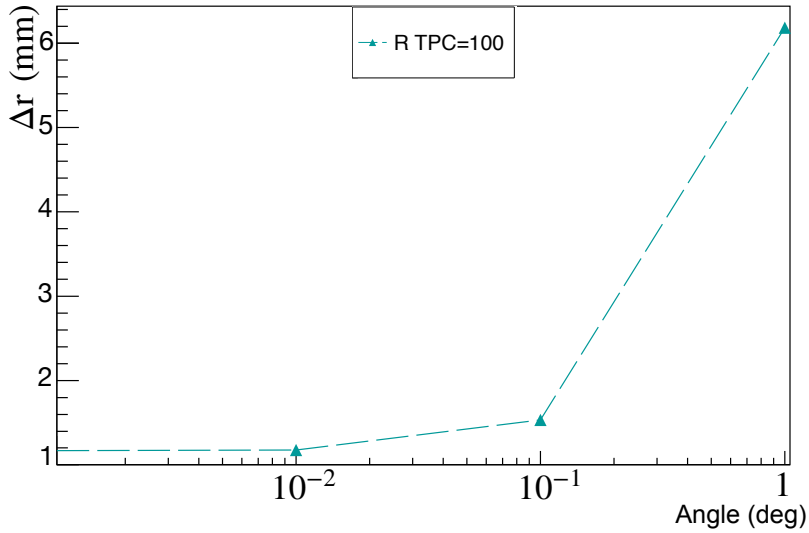

Figure 4.12.: Deflection Δr as a function of the E$\times$B angle, for the full drift length of 285 mm with a 4 T magnetic field and 200 V/cm electric field and a Ar/CF4/iso: 85/13/2 gas mixture.

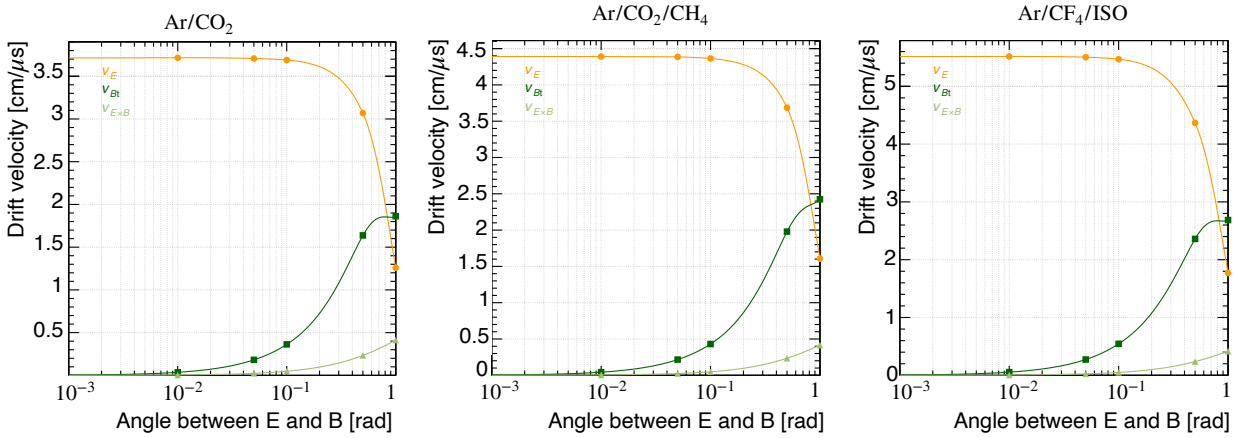

Figure 4.13.: Drift velocity as a function of the Lorentz Angle for the three candidate gas mixtures.

shown in Fig. 4.14. At very low pressures, the breakdown voltage is high since the mean free path of electrons is longer than the gap distance. As a consequence, the electrons reach the ground before encountering atoms to ionize. In contrast, at a high pressure the mean free path is so small that electrons cannot reach the necessary acceleration to ionize an atom before colliding. The minimum breakdown voltage at one bar in air is reached for a gap in the range of 6 to 8 μm.

Corona Discharge

This type of discharge involves a partial arc between two electrodes (instead of a full short). The main disadvantage of the corona discharge is that even though it is will not produce an instant failure of the detector, the partial discharges over time degrades the insulation system, diminishing the detector's lifetime. To minimize corona, sharp edges are to be avoided and insulations should be as thick as possible [156].

To mitigate this risk, a study of the field strength in unwanted areas where air or the gas mixture might be present is carried out.

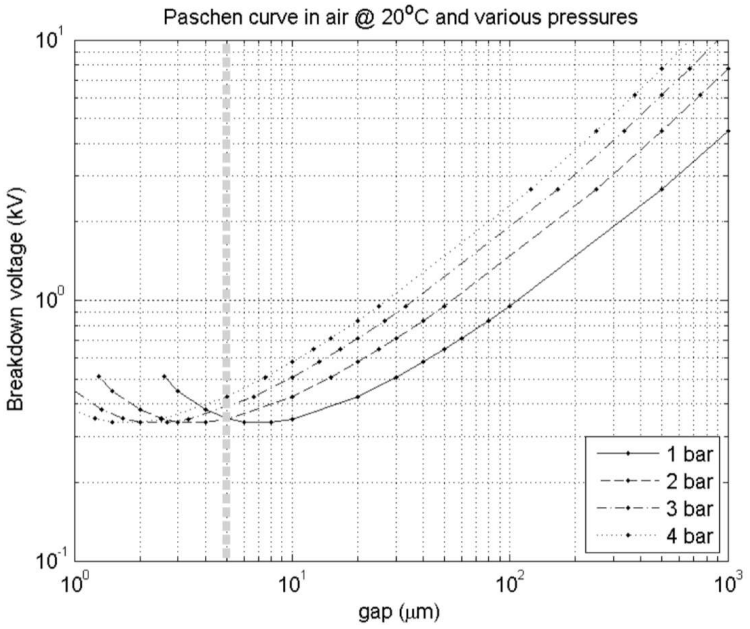

Figure 4.14.: Paschen curves of air at different pressures, as a function of the gap between electrodes. Figure reused with permission by [155] ©2008 IEEE.

4.2.2. COMSOL Simulations

The critical areas were identified and a study of the field strength and risk of discharge was performed with the electric currents package of the multi-physics software COMSOL. Figure 4.15 shows the cross-section of the 3D simulated section of the field cage, identifying the components included. The materials and electrical properties are summarised in table 4.1. The critical regions are:

- The air encapsulated in the O-Rings groove.
- The air encapsulated in the screws.
- The conductive edges of the resistors.
- The air encapsulated in regions where the epoxy might not completely cover the cathode.
- The HV connector region.

Table 4.1.: Materials electrical parameters.

Part	Material	Conductivity (S/m)	Permittivity (F/m)
O-Rings	Fluorinated Ethylene Propylene (FEP)	1×10^{-7}	2.1
Screws	Polyetheretherketone (PEEK)	1×10^{-14}	3.3
HV housing	Brass	1.6×10^{7}	
Metallic shield	Aluminium	3.7×10^{7}	
Cathode	Copper	5.9×10^{7}	
Insulation	Epoxy	6.1×10^{-11}	5.4
-	Air	3×10^{-15}	1

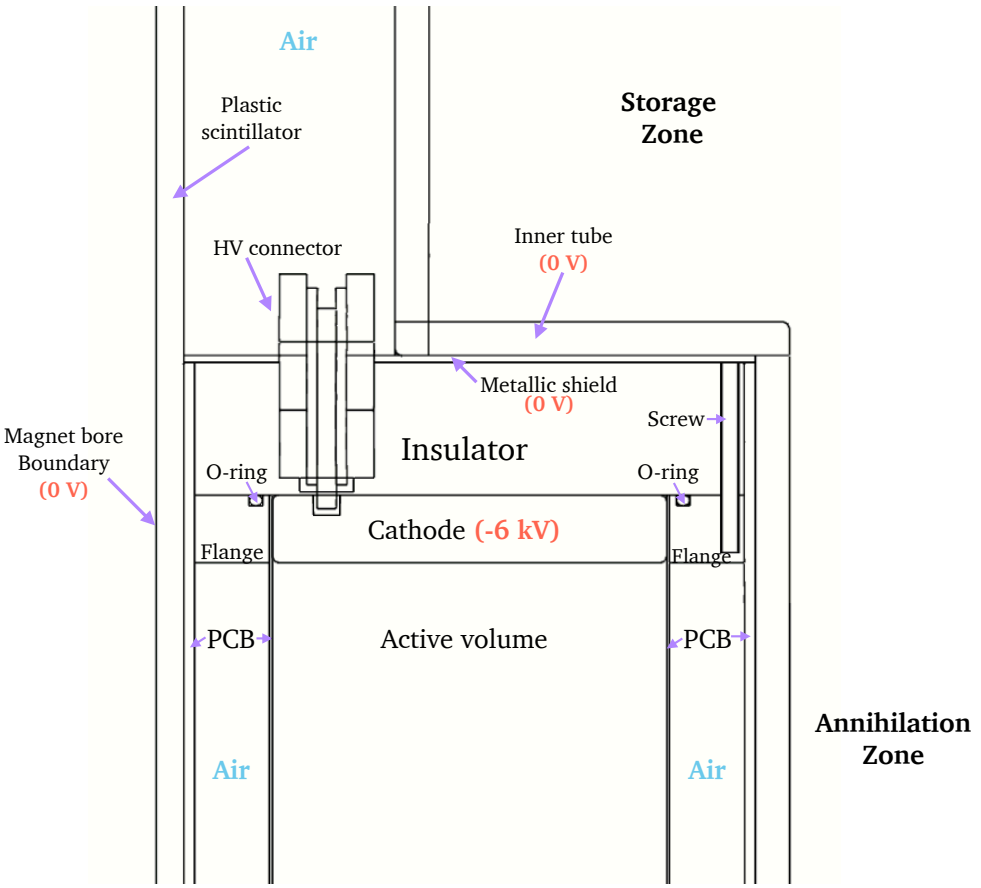

Figure 4.15.: Cross sectional view of the field cage components simulated in COMSOL for the discharge study.

Air encapsulated in the screws

When inserting screws to assemble the field cage, air can be trapped within the threads and create discharges in the high field region. The simulation in this case consists of inserting a non-metallic[1] M4 screw as sketched in Fig. 4.15 with a layer of air of variable thickness surrounding it. The results of the simulation are shown in Fig. 4.16.

The left hand side of Fig. 4.16 shows a 2D representation of the field strength obtained considering a layer of air of five different thicknesses surrounding the screw. The drop of the curves corresponds to the field inside the screw, while the peaks are the interfaces among both media. The highest fields are seen at the side of closest approach to the cathode (right peaks). These values are then compared with the electric field strength corresponding to the breakdown of air following the Paschen model up to an air gap of 1 mm. Higher values are considered to be unlikely to occur. As it can be observed, the expected breakdown is in the order of at least twice as much as the field strength foreseen in this area, leaving a prudent safety margin.

Air encapsulated in the O-Ring groove and in the epoxy-cathode interface

Similarly to the previous case, the air contained in the space between the O-rings and the groove is studied (see Fig. 4.17). By comparing the electric field strength with the breakdown voltage from the Paschen curves of Fig. 4.14, it is observed that the maximum field strength is below 2.5 kV/mm,

[1]The screw is made out of a high purity polymer called PEEK, specially suitable for assemblies in high voltage.

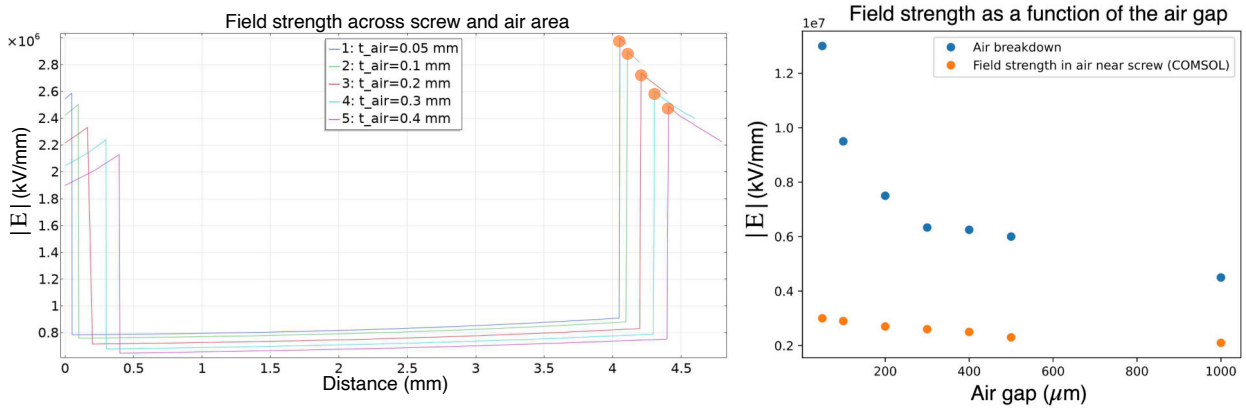

Figure 4.16.: Left: Electric field strength across the simulated screw for different air gaps surrounding it. Right: Comparison of the field strength required for breakdown in air according to the Paschen model (blue) with respect to the field strength obtained in the most critical points (marked with orange in both figures).

while the Paschen field strength needed to produce a breakdown ranges between 4.5 kV/mm (for a 1 mm gap) to ∼13 kV/mm (for a 50 μm gap).

In order to not have the rounded cathode close to the tube in air, the copper piece is surrounded by epoxy which provides a high dielectric strength. The right-hand side of Fig. 4.17 shows the result of the simulation in the air trapped between the cathode, the epoxy and the PCB. In this case, the electric field strength in gaps lower than 0.5 mm remain at least one order of magnitude below the breakdown voltage. The closest approach to the breakdown voltage is at 0.5 mm, where the breakdown voltage becomes 4 kV/mm and the simulation shows that the field strength is $\lesssim$ 3 kV/mm, which is nonetheless safe of discharges. For larger gaps the discrepancy increases once more.

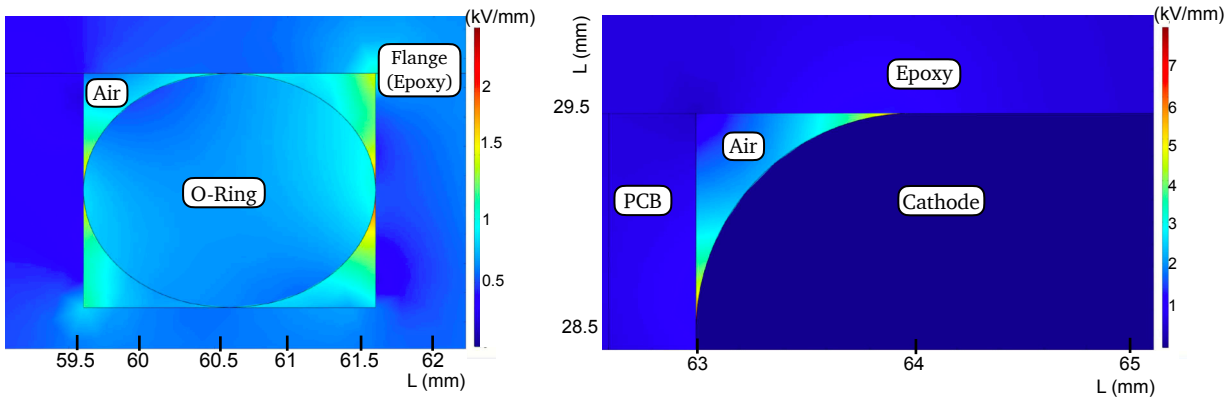

Figure 4.17.: Left: Electric field strength in the area of the O-ring. Right: The same result in the air trapped in the interface between the epoxy and the PCB.

The High-Voltage connector region

The left-hand side of Fig. 4.18 shows the positioning of the high voltage connector[2] within the cathode and with respect to surrounding grounds. The output of the simulation is shown on the

[2]The connector part is a Lemo EHP.1S.405.CTL.

right-hand side of the same figure. It is observed, in this case, that the high field strength is rapidly quenched within the housing of the connector due to the built-in insulator, posing no risk for the setup.

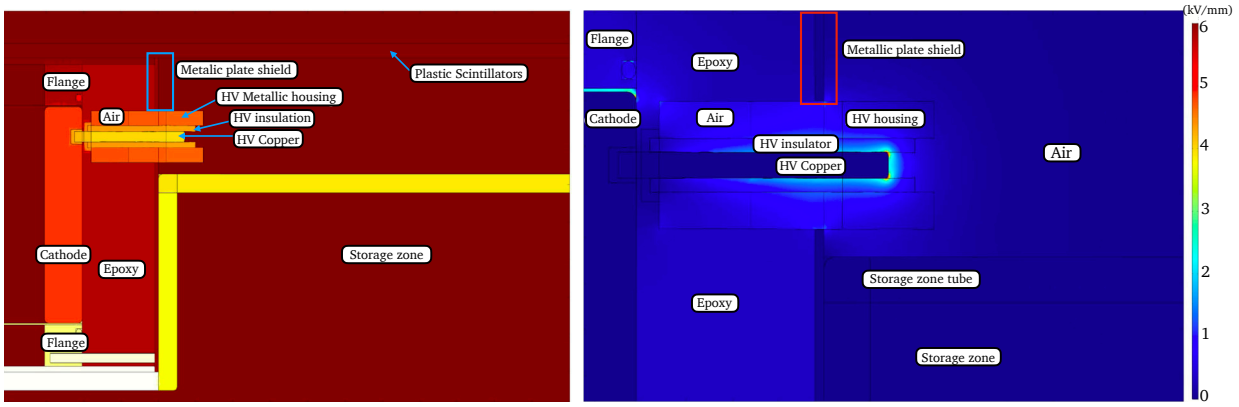

Figure 4.18.: Left: Positioning of the high voltage connector in the TPC. Right: Field strength in the region.

Resistors' edges

The sharp conductive edges of the resistors near the cathode at a distance of 11 mm to the ground, might be a source of discharges. In this case, a reduced version of the field cage that captures the essence of the region of concern is simulated and shown in Fig. 4.19. The ground is placed at a distance of 11 mm from the high voltage, at -6 kV. Additionally, the conductive strips in both sides of the internal PCB are included. Finally, a set of four resistors[3] of $2 \times 1.25 \times 0.5$ mm^3 are placed on top of consecutive strips, away from the boundaries of the simulated region in order to avoid inaccuracies in the calculation due to artificial edge effects.

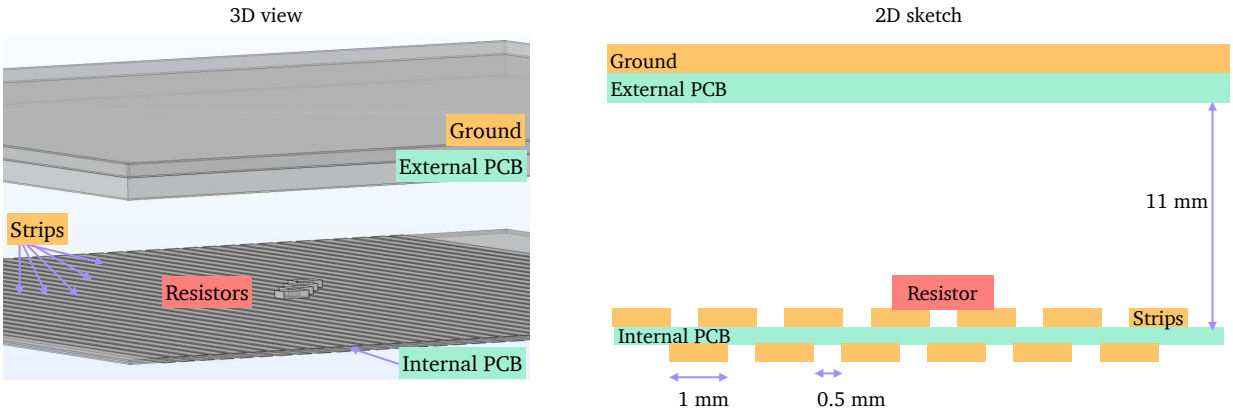

Figure 4.19.: Left: 3D view of the setup in COMSOL to study the discharge probability due to the edges of the resistors. Right: 2D sketch with dimensions included. See text for more details.

The mean field strength around tip of the edge of the resistors is extracted. As a first step, a mesh size analysis is made: the same simulation is performed for different mesh sizes until convergence of the results is achieved, as shown in Fig. 4.20.

[3]Based on a high reliability 1MΩ Panasonic resistor, ERA series model.

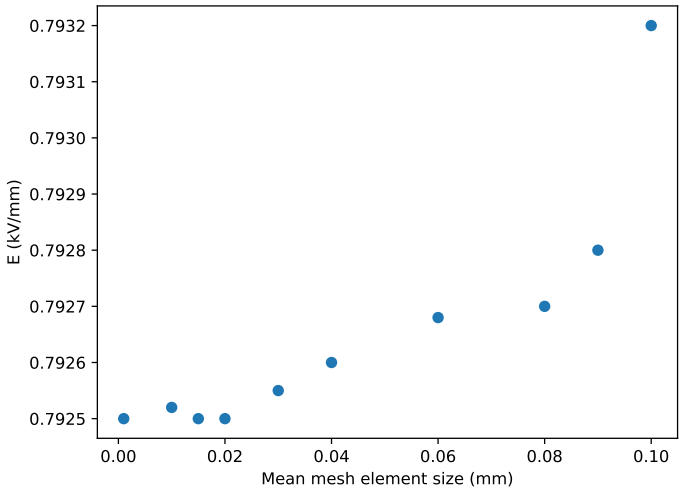

Figure 4.20.: Field strength obtained at the resistor's edges for different mesh sizes.

To increase the safety of the region, the resistors will be sprayed with Polyurethan to create a 100 μm insulating layer. This material has a high dielectric strength that suppresses the possible sparks that might emerge. With this addition, the maximum electric field strength obtained in this air gap is 0.049 kV/mm.

5. TPC Construction

The output of the TPC simulations converged into the technical design of the detector. The PUMA TPC is being built at CERN by the micro-pattern gas detector (MPGD) group of CERN [157]. Details of the process and full setup are given in the following.

5.1. Cathode and Field Cage

The cathode is a 10 mm thick copper plate with 1 mm round corners and a 1-100 μm gold-plating (see Fig. 5.1). The gold plating provides higher conductivity and less degradation of the surface over time than copper. Additionally, the round corners ensure a field strength below the breakdown voltage of air (as seen in Ch. 4).

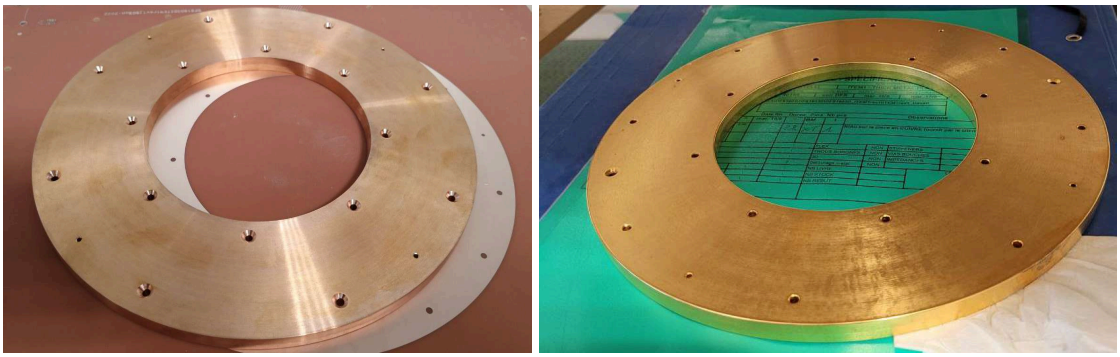

Figure 5.1.: Cathode of the TPC. Left: Raw material (copper). Right: Cathode after the gold-coating procedure.

The cathode provides the entrance of four gas entrance and exits to the active zone (and additional four at the anode side) and it is shielded from the ground at the inner and outer radius through a 16 mm tick PCB layer, shown in the technical drawing of Fig. 5.2. The cathode is screwed into the PCB with 16 M4 screws embedded into the plate (only two are shown in the figure).

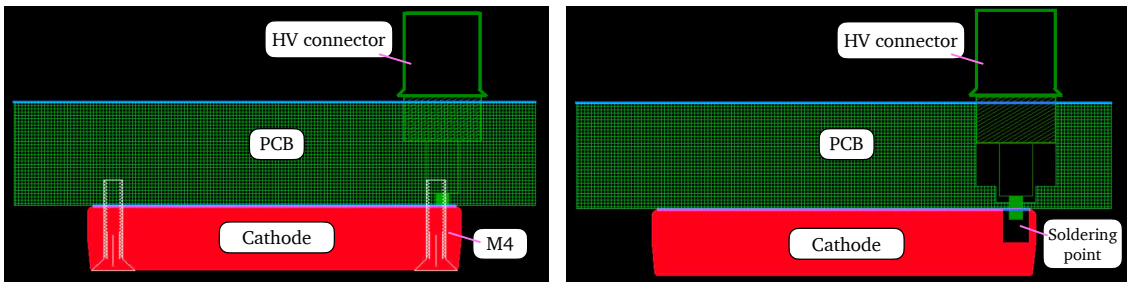

Figure 5.2.: Drawing of the cathode assembly with the shielding PCB (left) and the high voltage connection (right).

The field cage structure consists of 200 field shaping strips 1 mm wide with 40 μm rounded edges and 500 μm interstrip, printed at each side of a flexible PCB.The strips on both sides are connected through vias, and the degraded potential is achieved by a resistor chain (1 MΩ each) soldered on the outer side of the active volume. The scheme is shown on the left side of Fig. 5.3 while the manufactured strips are displayed in the middle figure. The first strip of the field cage is connected to the cathode, rendering both at the same potential. An identical resistor chain is installed in case of failure of one of them. A current readout of 10 nA provides sufficient resolution as to determine wether a resistor works at 80% of its nominal operation. The resistors soldered into the PUMA field cage is shown in the right-hand side of the same figure.

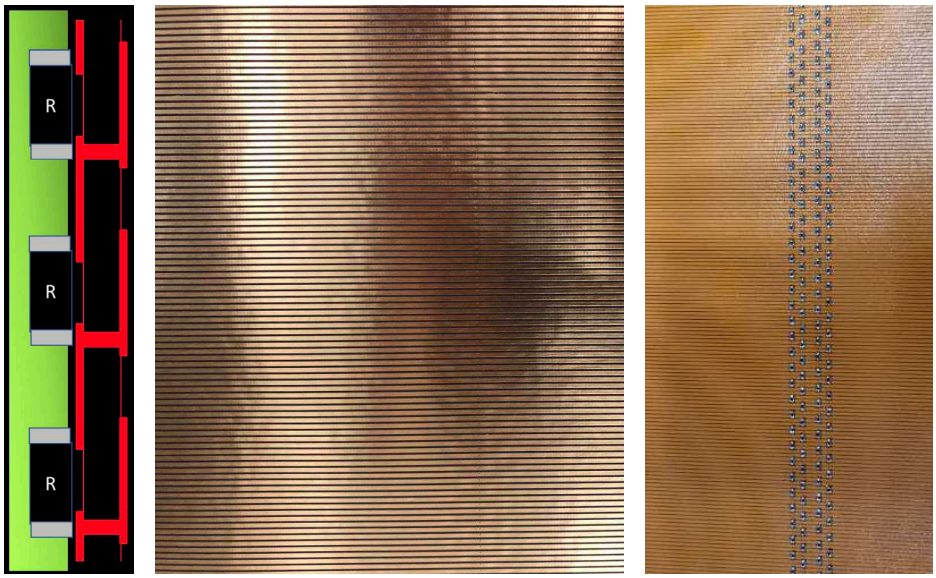

Figure 5.3.: Left: Strips and resistors scheme. Middle: TPC Field cage foil from the sensitive volume side. Right: Detail of the soldered resistor chains on the opposite side of the foil.

5.2. Pad Plane

5.2.1. Layout

A study of the geometry of the pads is performed in order to optimize the identification of the charge of the pions. To that end, three different possibilities are studied. On the one hand, the option of identically square pads of 3×3 mm^2 of area (see left side of Fig. 5.4). The second and third alternative consists of $\sim$10 mm^2 pads. The difference between these two lies in how the azimuthal and radial widths vary. The middle plot of Fig. 5.4 shows a layout identified as "radial extension", corresponding to pads that are square in the outer ring and become elongated in the radial direction towards the inner ring. In contrast, the right-hand side of the same figure displays the "azimuthal extension" layout, corresponding to square pads at the inner ring which become wider in the azimuthal direction towards the outer radius of the TPC.

The simulation is run for 1500 events and the 2D projection of the tracks in the pad plane are analysed by fitting a circle, in the same manner as explained in Sec. 3.2. The result is shown in Fig. 5.5.

It is observed that all three options converge to an efficiency of 95% at R= 120 mm. The trend shows that the radial extension geometry performs systematically better than the others. The reason is the increased granularity in the angular direction with respect to the other two geometries. In

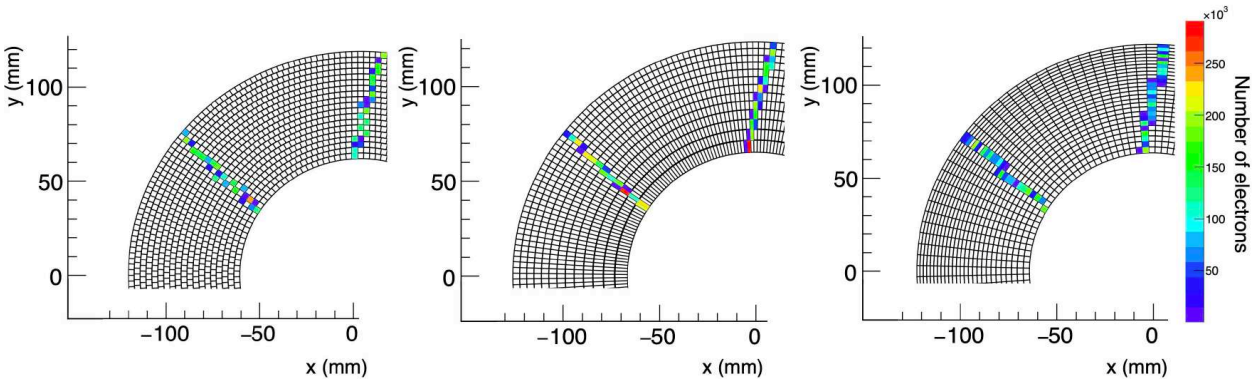

Figure 5.4.: Pad geometries studied with two tracks simulated. The pads area is kept constant in all cases. Left: Square pads. Middle: Pads with radial extension. Right: Pads with azimuthal extension.

contrast, the azimuthal extension is the least efficient of the three, for the same reason. The efficiency obtained with the square geometry is a middle ground between the two.

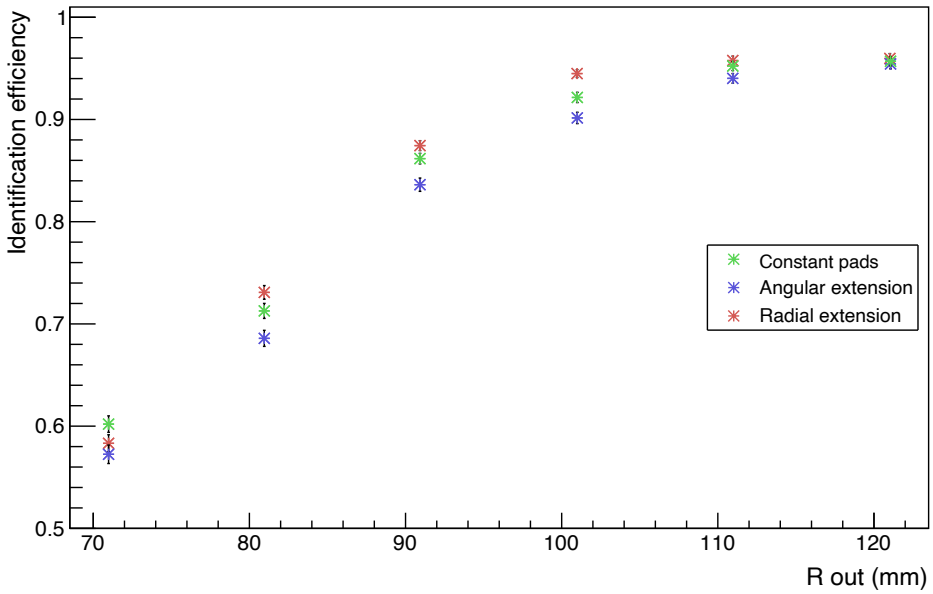

Figure 5.5.: Efficiency for accurately detecting the charge of the pions as a function of the external radius of the TPC.

Considering this study, either option would be suitable for the PUMA TPC (since its outer radius is 120 mm). However, considering the trend and production feasibility, the "radial extension" geometry is chosen.

5.2.2. Mapping

The final design of the pad plane consists of a total of 4096 channels distributed in 16 sectors. Each sector is formed of 256 channels and read by a single front-end electronics card "A Readout Card" (ARC) containing four 64 channels STAGE chips [158], see Sec. 5.3. The dead-time of the system is driven by the chip with the highest number of channels hit. Since each sector of the TPC is read

exactly by one card, the distribution of the channels within the layout of the pad plane is optimized in order to obtain the minimum number of channels occupied by a single chip.

The upper part of figure 5.6 shows the three different distributions per sector simulated. For each event, the number of active channels per chip is recorded and the maximum of the group is saved and stored in a histogram. The output is shown in the lower side of Fig. 5.6.

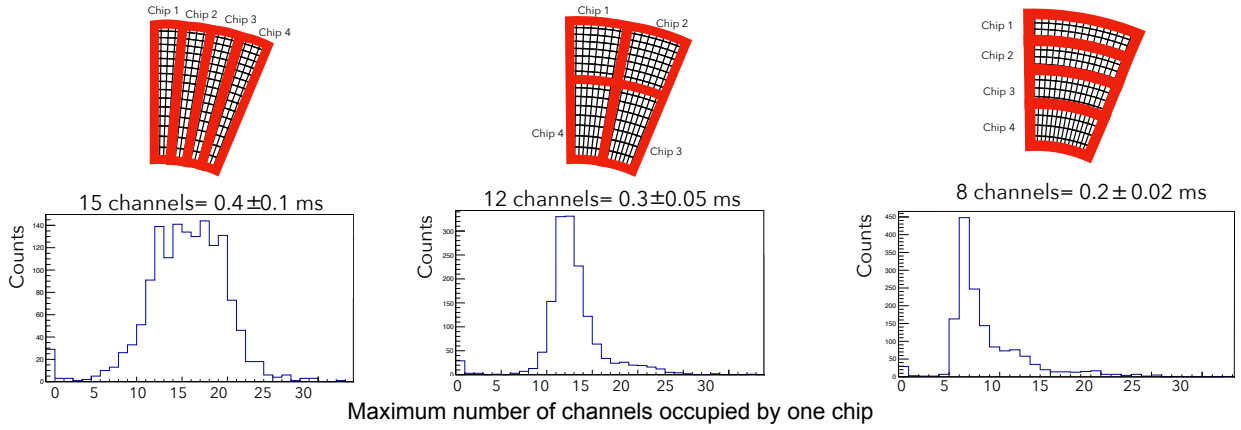

Figure 5.6.: Possible mappings of a TPC sector to the front-end electronics chips for a single card.

In the left radial distribution it is observed that the highest number of channels occupied in a single chip is 15±5 channels, corresponding a dead time of 0.4±0.1 ms. The right-hand side distribution (azimuthal) the mean number of maximum occupied channels decreases to 8, or 0.2±0.02 ms. Finally, for a compromise between both (middle distribution), a mean dead time of 0.3±0.05 ms is obtained.

Because the expected maximum event rate corresponds to 100 Hz, any of these possibilities are suitable for the PUMA TPC. The middle distribution is finally chosen as it is easier to produce than the "angular" option, while still keeping a low dead-time in views of possible upgrades of the experiment that would entail higher event rates.

5.2.3. Manufacturing

The anode consists of a composite sandwich structure where the top layer is a 50 μm Diamond-Like Carbon (DLC) with a resistance of 10 MΩ/□[1], used to protect the pad plane from discharges. The DLC, which is at ∼500 V, is enclosed in a Faraday cage via the Micromegas mesh and the anode pads. The grounded mesh extends below the field cage internal PCB structure. Three additional layers alternating copper, glue and epoxy make up the charge sharing section and three more layers are used to map the pad plane to the connectors in the backplane.

The manufacturing steps of the anode require, first, the cutting and drilling of the holes of the PCB. After that, the excess debris from the holes is removed by desmear. In this chemical process, the resin remaining is softened with water-based solutions [159] and subsequently the chemical bonds are broken with paramanganate. Finally, a neutraliser is used to remove the permanganate. Once the PCB is cleaned, lithographic techniques are used to etch and print the circuit one layer at a time. The left-hand side of Fig. 5.7 shows the mask of the backplane, where the holes are vias for the pins of the connectors which need to be etched out.

The middle picture of Fig. 5.7 shows the back plane of the anode side. The printed layout in radial position of the 32 140-pin connectors for data transfer are observed, each of which is mapped to 128 channels. Additionally, the four 3 mm holes for the entrance/exit of the gas are placed, as well

[1]This unit is commonly used to describe the surface resistivity across any given square area of a material.

as two points for measuring the current in the mesh. Additional holes for mechanical support are placed in the inner and outer radius.

The segmentation of the pad plane according to the study shown in subsection 5.2.1 is shown on the right hand side.

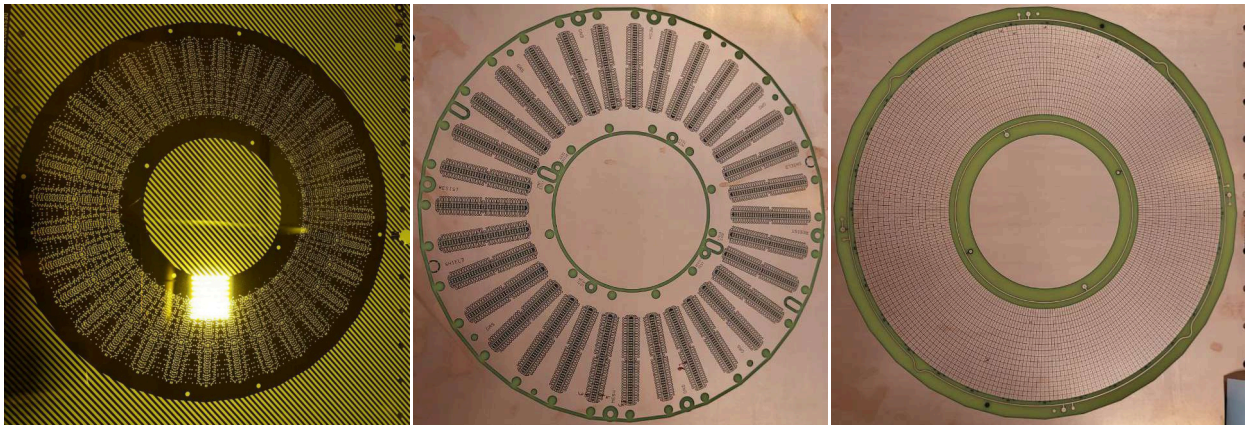

Figure 5.7.: Anode side of the PUMA TPC. Left: Mask. Middle: Back plane. Right: Segmented pad plane

5.3. TPC Electronics

5.3.1. Front-End Electronics

The signal is collected in 16 Front-End Cards, one shown in Fig. 5.8. Each card consists of 4 ASICs with 64 channels each. Upon reception of an external trigger (from the plastic scintillator's barrel) the signal is sampled in a 511-bucket switched capacitor array (SCA) analog memory and converted to digital format with a 25 MHz 12-bit multi-channel analog-to-digital converter (ADC).

The system will operate with the latest generation of the AFTER ASIC, called STAGE [158], developed at IRFU (CEA Saclay). STAGE allows a digitization of the signals at an adjustable frequency of 1-100 MHz and choice of peaking time from 50 ns to 100 μs. Additionally, STAGE provides the possibility of self-trigger, with a discriminator in each channel for multiplicity building that allows only hit channels to be read-out, accordingly reducing dead-time. Another advantage is that the charge sensitive preamplifier (CSA) has an adjustable gain to support the dynamic range of 120 fC to 10 pC for event latex rates of up to 1 kHz, which is adjustable for each channel.

The signal transportation from the pad plane to the front-end electronics is carried out via 1.3 m long, high speed (propagation delay of 4.2 ns/m) micro coaxial ribbon cables of 75 Ω at 59 pF/m.

The rms noise per channel as a function of the input capacitance of the STAGE chip is given in Fig. 5.9, for a 120 pC dynamic range. Using a peaking time of 230 ns and an input total capacitance of 80 pF[2], gives a noise level of 1200 electrons rms. Hence thresholds of above $5 \times \sigma_{\mathrm{rms}} = 6000$ electrons gives a significant operational margin to use the multiplicity trigger in the ARC electronics.

5.3.2. Back-end Electronics

Outputs, numeric data, clock, and trigger are optically carried to the Trigger and Data Concentrator Module (TDCM) and the switch. The back-end consists of a TDCM, seen on the right-hand side

[2]A capacitance of 80 pF corresponds to 1.3 m long of low-capacitance cables.

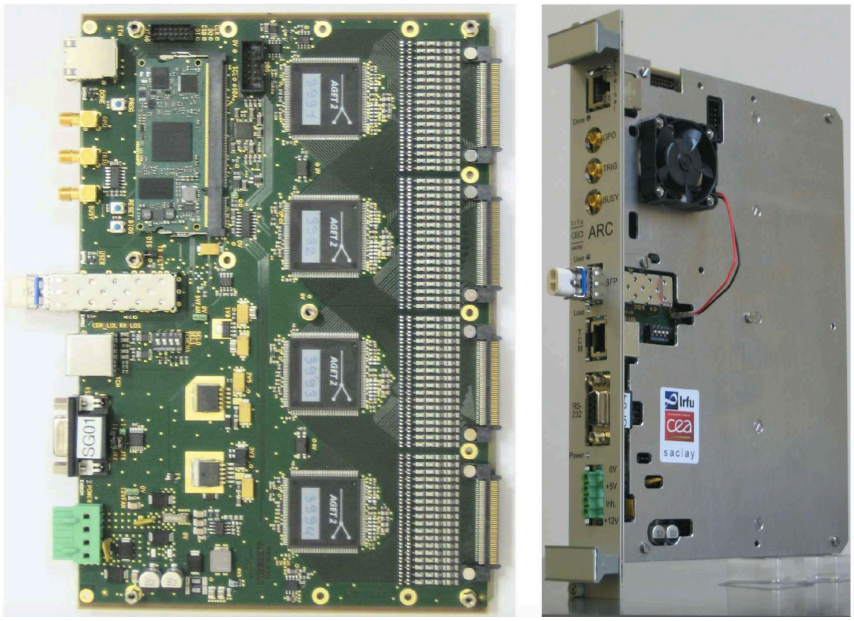

Figure 5.8.: Left: Front-end card containing four AGET chips. Right: ARC with an electromagnetic shield and cooling system.

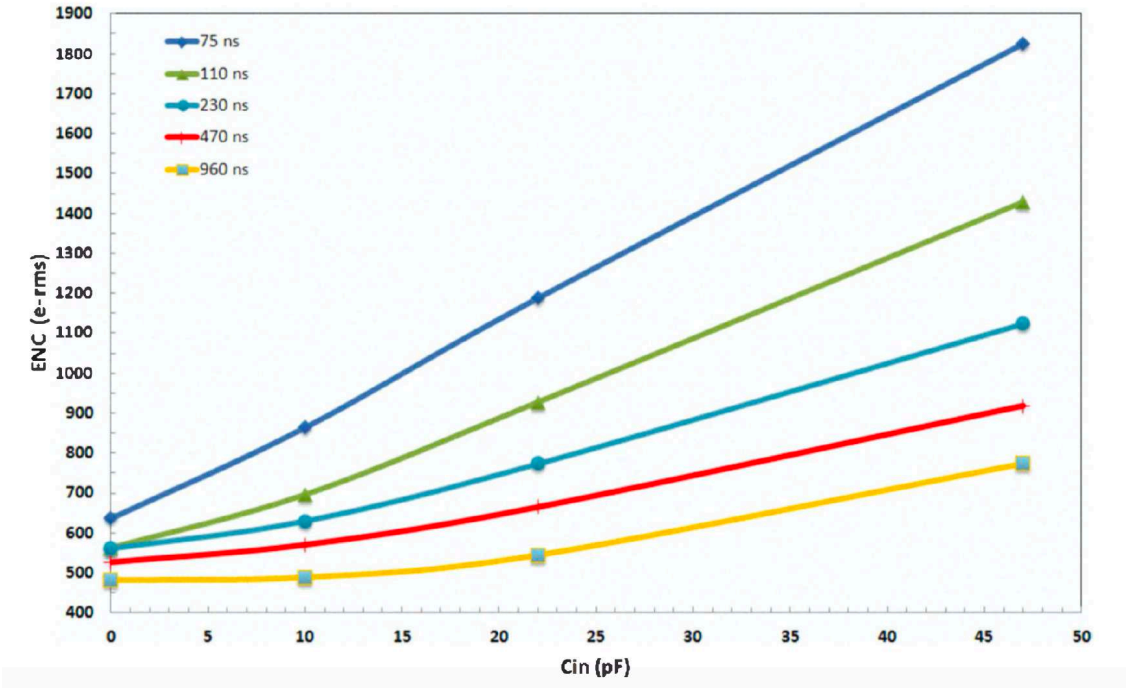

Figure 5.9.: ENC vs. input capacitance for different peaking times in the 120 fC dynamic range of the AGET chip. Figure reused with permission by [158] ©2011 IEEE.

of Fig. 5.10, which distributes a primary reference clock to the set of front-end cards as well as a common trigger signal and global synchronization of the front-end. The TDCM is composed of two mezzanine cards (custom made board that can house up to 16 small form factor pluggable optical

transceivers (SFP)) that are plugged into the carrier board of the back-end unit, a Field Programmable Gate Arrays (FPGA) module (the Mercury ZX1 commercially available from Enclustra [160]), and a main carrier board designed to carry the FPGA module and the mezzanine cards.

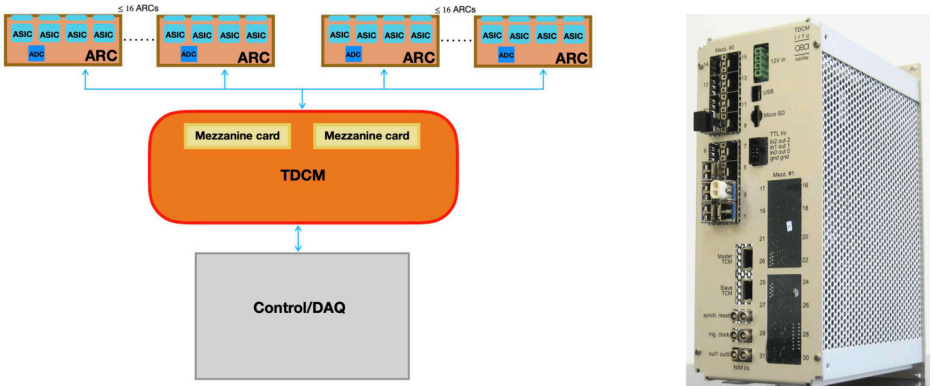

Figure 5.10.: Left: Diagram of the TPC electronics. Right: Back-end module (TDCM) of the TPC electronics.

One TDCM module is enough for the PUMA TPC since it can host up to 8000 channels (16 front end boards per mezzanine card). A diagram of the electronics system for the TPC is shown on the left side of Fig. 5.10.

5.4. Mechanics and Plastic Barrel

The TPC will be fixed mechanically to the beam tube with no extra degree of freedom, and the full trap-TPC-plastic barrel system will be aligned to the magnetic field together. Both PCB plates holding the anode and cathode of the TPC are shaped in a 32-faced polygon to support the plastic scintillator bars. Two wheels at either end of the setup will accurately set the plastic scintillators in position (see Fig. 5.11).

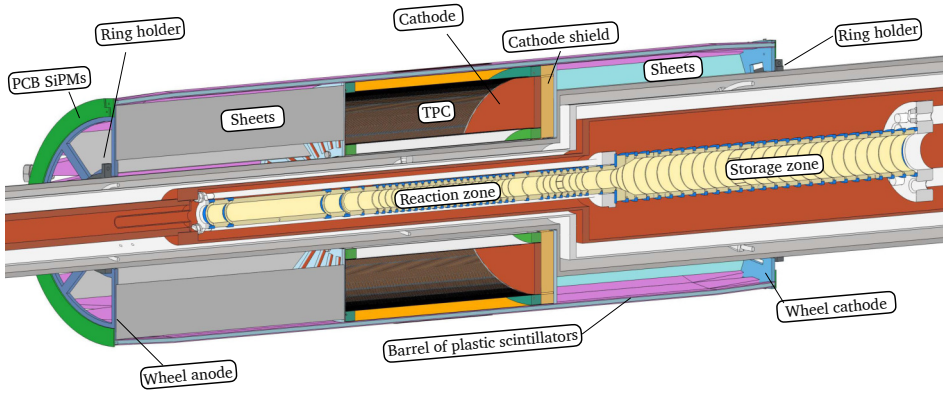

Figure 5.11.: TPC and Plastic scintillators assembled in the beam tube.

The wheels are 3D printed and have radial grooves on the inner side, where sheets of aluminium are slid and glued. The same grooves are added to two additional thin (0.5 mm) plates screwed to the TPC's backplanes. In this way, the wheles and the TPC remain mechanically fixed through the sheets.

The barrel of 1 m long plastic scintillators are held together with lids on top of the wheels and a 200 μm layer of kapton will cover the full barrel. The plastics are read-out via silicon photomultipliers

(SiPMs) attached to PCBs to the wheels and provide the trigger to the TPC. The characterization of the barrel is out of the scope of this work and is part of the Master thesis of C. Xanthopoulou (TU Darmstadt, 2022).

At the time of the submission of the present PhD thesis manuscript, the TPC is being built but is not yet finalized.

Part II.

Antiprotonic atom decay

6. The Formation and Decay of Antiprotonic Atoms

In this part of the thesis, a review of the formation and decay of exotic atoms, and antiprotonic in particular, is presented. Based on these physics principles, a cascade code is used to compute the X-rays and annihilation probabilities of tin and calcium isotopes for different Skyrme densities parametrizations and capture states in order to estimate the sensitivity of PUMA.

6.1. Exotic Atoms

The exotic atoms consist of a negatively charged particle bound to an atom by the Coulomb interaction in exchange of (at least) one electron. In particular, one can distinguish among muonic atoms and hadronic atoms (where the exotic particle is either π^-, K^-, Ξ^- or $\bar{\mathrm{p}}$). The difference lies in that the hadronic atoms interact with the nucleus via the strong force, in addition to the electromagnetic attraction. Exotic atoms were predicted in 1940 [161, 162] and observed for the first time in photographic emulsions by detecting Auger electrons, product of the heavy particle's transitions [163] (see Sec. 6.1.2). Muonic [164], kaonic [165], pionic [166] and antiprotonic [167] atoms have been observed and extensively studied. Furthermore, atomic sigma hyperons have also been observed [168].

Exotic atoms provide an excellent tool to probe the nucleus. Because of the large mass difference between electrons and the mentioned particles, the Bohr-like radius

$$a_0' = \hbar / e^2 \mu,$$

(where μ is the reduced mass of the particle-atom system) is >200 times closer to the nucleus than the Bohr radius of an electron, a_0. In particular, the muonic and antiprotonic atoms Bohr radius are 28.8 fm and 57 fm, respectively.

This feature has been used with muonic atoms, for instance, to provide an answer to the long-standing question of the proton radius puzzle [169] where it was measured to be 0.842±0.001 fm, 5σ smaller than some of the previous measurements that were already in tension. Additional experiments [170–172] and re-evaluation of previous data [173, 174] agree with the muonic measured value.

In the case of kaons, precision studies of the hadron-nucleus interaction in kaonic atoms are performed to constrain low-energy QCD in the strangeness sector through scattering length determination [175], with implications in astrophysics [176] and physics beyond the standard model [177].

Additionally, the X-ray spectroscopy of pionic decays has provided the most accurate measurement of the mass of π^-, giving a value of 139.57077±0.00018 MeV/c^2 [178].

Historically, antiprotonic atoms have served as a test-bench to study antiprotons themselves: Indeed, the first observation of antiprotonic atoms was in the context of measuring the antiproton mass [167].

The first experiment that used antiprotons as probes was performed at the Brookhaven National Laboratory (see Sec. 1.3.3). However, their systematic use was made possible after the development of a stable antiproton beam in the 1980s, at the LEAR facility at CERN [179]. Nowadays, antiprotonic atoms are used to study different phenomena. As an example, antiprotonic He was used (among others) to set an upper limit to the interaction strength of potential new long range interactions

among nucleons [180]. In another recent experiment [181], antiprotonic He was used to study high-resolution laser spectroscopy applications in superfluids, with implications in the detection of cosmic-rays antiprotons or antideuterons.

The process by which a heavy negatively charged particle interacts with the atomic nucleus can be divided into three main steps:

- The capture of the particle by the ion or atom in a highly excited state.
- The de-excitation (or cascade) of the particle through the atomic energy levels via emission of Auger electrons (higher levels) and X rays (lower levels).
- The absorption of the particle due to the strong force interaction and further production of mesons. Muons can either decay or be captured by the nuclei [182].

Each of these steps, specified for antiprotons, are sketched in Fig. 6.1 and detailed in the following.

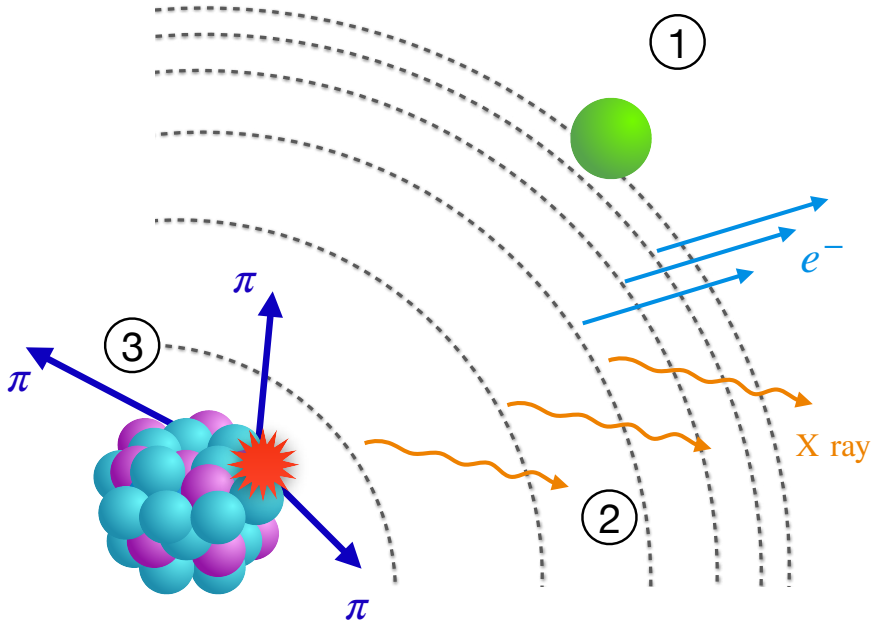

Figure 6.1.: Steps in the antiproton-nucleon interaction: 1. The capture of the antiproton. 2. The de-excitation via emission of Auger electrons and X rays. 3. The annihilation with a nucleon, followed by the emission of pions.

6.1.1. Capture

When the energy of a negatively charged particle X^- is similar to the energy of the valence electron of an atom, the particle is captured in an Auger process by ejecting the valence electron. The energy level of the capture corresponds to

$$n_X \approx n_{e^-} \sqrt{\frac{\mu}{m_{e^-}}}$$

where n_e is the energy level of the ejected electron and μ is the reduced mass of the X^-–atom system.

The pioneering model to describe the capture of negative heavy particles in matter was developed by Fermi and Teller [162]. In this model, the particle is treated classically under the assumption that it sustains a continuous energy loss by the interaction with a cloud of electrons, considered

a degenerate Fermi gas. This assumption is based on the fact that the wavelength of the exotic particle is much shorter that the electrons' in the energy range where the capture occurs [183]. As an example, a muon with an energy of 10 eV would have a wavelength of 0.03 a_0.

Under these assumptions, the average energy loss of the negatively charged particle per unit time is given by

$$-\frac{dW}{dt} = \int \frac{2\ \mathrm{d}^3 k_\mathrm{i}}{(2\pi)^3} v_\mathrm{rel} \Delta E \frac{\mathrm{d}\sigma}{\mathrm{d}\Omega_\mathrm{cm}} \mathrm{d}\Omega_\mathrm{cm} \tag{6.1}$$

where v_rel corresponds to the relative velocity between the electron and the negatively charge particle, $\mathrm{d}\sigma/\mathrm{d}\Omega_\mathrm{cm}$ is the center-of-mass differential cross section for the collision [184] and ΔE is the X^- kinetic energy transferred per collision. This model served as a basis of multiple semiclassical [185–188] and quantum mechanical [189–191] calculations aimed at tackling the capture process.

Direct experimental evidence of this part of the interaction is technically difficult, as the energy of the Auger electrons ejected at capture and while the particle traverses the electron cloud (in the order of a few tens of eV) is too small for detection [192]. Instead, the X-rays from lower energy transitions are measured and compared to quantum mechanical calculations for different initial distributions of angular momentum, which are then adjusted accordingly to best agree with the experimental values [193–195].

By simply counting the number of substates available at each orbital l at a fixed energy level n, one obtains a statistical distribution

$$P(l) = (2l + 1),$$

in which the particle can be captured.

A more general parametrization is the modified distribution

$$P(l) = (2l + 1)e^{\alpha l},$$

where α is a free parameter. A positive value indicates a bigger capture probability in higher l orbitals, whereas negative values correspond to a dominant population in lower angular momentums and α=0 recovers the statistical distribution. Measurements of X-ray data indicate that the value of α is constrained to the range $0 < \alpha \leq 0.2$, where the variation corresponds to a dependence on Z and the chemical compounds in which the interaction occurs [185, 196, 197].

Despite the impossibility of measuring the initial distribution, calculations show that the angular momentum distribution at capture is essentially not modified as the particle traverses the electron cloud upon reaching the K electron shell [184, 193]. This level corresponds to $n_{\bar{p}} \sim 43$ in the case of the antiproton.

6.1.2. Cascade

After traversing the electron cloud, the remaining de-excitation steps, starting from $n_X = 14$ for muons up to $n_X = 43$ for antiprotons, can be fully described with quantum mechanical calculations [198].

For atoms with Z>2[1], the two leading decay mechanisms are Auger and radiative dipole transitions, in which the widths are related to the transition energy ΔE by [201]:

$$\Gamma_A \propto \Delta E^{-1/2}, \tag{6.2}$$

$$\Gamma_R \propto \Delta E^3. \tag{6.3}$$

From these widths it is observed that the Auger transitions are favoured in the higher states of the cascade, where the transition energies are small, while the radiative transitions are dominant in the

[1] In antiprotonic hydrogen atoms a dominant process is the Stark mixing, in which the antiproton feels the electric field of neighbouring atoms, producing transitions towards lower l for a given n level [199, 200].

lower states. In order for the Auger de-excitation to occur, however, two additional conditions need to be met:

1. There have to be electrons available to eject.
2. The transition energy ΔE has to be larger than the ionization energy of the electron to be ejected [202, 203].

The first point is relevant in isolated systems, which is the case for PUMA. As there are no available electrons in the surroundings that can be picked-up to refill the hole of an ejected electron, the atomic shells become progressively empty until no electrons are left. The cascade continues, then, via the emission of X rays.

As the shells are successively emptied, the ionization energies of the inner electrons increase while the screening of the nuclear charge is reduced [204]. In the case the second condition is not met, the auger de-excitation is interrupted and continues via radiative emission until the transition energy of a subsequent state becomes large enough to allow, once again, for an Auger ionization.

Because the Auger transitions do not change the shape of the angular momentum [184] and as a result of the radiative transition electric dipole selection rule of the angular momentum ($\Delta l = \pm 1$, due to conservation of angular momentum of the emitted photon), the cascade tends to converge to the circular states ($n, l = n - 1$) quickly [198].

As the particle approaches the lower energy levels, the strong interaction from the nucleus modifies the purely electromagnetic cascade. This process detailed in the following.

6.1.3. Annihilation

The X-ray widths and energies of the last observable lines are distorted by the strong force, and the antiproton's annihilation with a nucleon takes place. This mechanism occurs at the overlap between the matter density and the wave function probability density, which gives a classical solution for the annihilation site of the antiproton.

The calculation of the shifts and widths is possible by considering a phenomenological optical potential, which is assumed to depend linearly on the nuclear density distribution [183, 205–207], consistent with existing X-ray data [208]

$$V(r) = \frac{2\pi}{\mu} \left[a_{n\bar{p}} \rho_n(r) + a_{p\bar{p}} \rho_p(r) \right], \tag{6.4}$$

where μ is the reduced mass of the antiproton-nucleon system, $a_{p\bar{p}}$ is the proton-antiproton scattering length and ρ_p is the proton density. The same variables with the subindex n correspond to the neutron, instead. With this assumption and treating the strong interaction as a perturbation of the electromagnetic interaction, the shifts and widths can be calculated as

$$\Gamma = 4 \frac{\pi}{\mu_{\mathrm{N\bar{p}}}} \mathrm{Im}\left(a_{\mathrm{N\bar{p}}}\right) \int \mathrm{d}r \rho(r) \left|\psi_{\bar{\mathrm{p}}}(r)\right|^2,$$

$$\varepsilon = 2 \frac{\pi}{\mu_{\mathrm{N\bar{p}}}} \mathrm{Re}\left(a_{\mathrm{N\bar{p}}}\right) \int \mathrm{d}r \rho(r) \left|\psi_{\bar{\mathrm{p}}}(r)\right|^2,$$

where the subscript N indicates either a proton or a neutron and $\psi_{\bar{p}}$ is the antiprotonic wave function. The scattering length's values are extracted by fitting the X-ray data. Experiments performed with oxygen isotopes [209] indicate scattering lengths consistent with $a_{N\bar{p}}$= (1.53 ± 0.27) + i (2.50 ± 0.25) [205] . However, later analysis of X rays [206] and experiments [210] found a better agreement with $a_{N\bar{p}}$=(2.4 ± 0.3) + i (3.4 ± 0.3).

6.1.4. Final-State Interactions (FSI)

The re-interaction of the residual nucleus with a pion after the antiproton's annihilation is a non-negligible process (estimated to happen 80%-90% of the cases [69, 70]). As a result of this interaction, a pion can be often absorbed or undergo charge-exchange ($\pi^0 \rightarrow \pi^{\pm}$, $\pi^{\pm} \rightarrow \pi^0$), affecting the charged pion multiplicity of an event and the accurate charge identification. For this reason, an event-by-event analysis would not provide accurate information of the annihilated nucleon. Instead, a statistical treatment of the data, proposed by M. Wada and Y. Yamazaki [211] would allow for the reconstruction of the annihilation ratios by considering the charge exchange and absorption probabilities, $\lambda^{\pm}, \omega^{\pm}$, expected to be in the range 0.1-0.2. This analysis is based on a phenomenological four-parameter model developed by S. Wycech [212].

The treatment of FSI for PUMA is out of the scope of this work. However, the development of a neural network that treats FSI with this method is currently ongoing by members of the PUMA collaboration [213]. The objective of PUMA is to reach an uncertainty below 10%.

6.2. The Cascade Code

The aim of the code is to compute the antiprotonic transition rates as the antiproton cascades down towards the nucleus of a pre-defined atom and annihilates with a nucleon. The computation saves the X-ray intensities, annihilation probability, antiprotonic population and the evolution of the 1s, 2s and 2p electron configurations at each step of the cascade.

An initial version of the cascade code was written in FORTRAN 77 by R. Seki, and later on modified by T. Koike. A version adapted to FORTRAN 90 was implemented by R. Seki.

6.2.1. Physics principles

The antiproton's transition probability between an initial state (n_i, l_i) and a final state (n_f, l_f), assuming that the energy of the final state $E_f < E_i$, is described by Fermi's golden rule [214]

$$\Gamma_{n_i,l_i \rightarrow n_f,l_f} = \frac{2\pi}{\hbar} |\langle n_f, l_f | H | n_i, l_i \rangle|^2 \rho(E_f),$$

where $\rho(E_f)$ is the density of final states that satisfies conservation of energy and H is the Hamiltonian of the system.

In the case of an electric dipole transition E_1, where the selection rules require $\Delta l = \pm 1$, this transition rate for the antiproton is given by

$$\Gamma^{\mathrm{rad}}_{n_i,l_i \rightarrow n_f,l_i \pm 1} = \frac{4}{3} \frac{\alpha}{Z^2 \mu^2} \left(\Delta E_{n_i n_f}\right)^3 |\langle n_f l_f | \, r | n_i l_i \rangle \times (l_i 010 | l_f 0)|^2 C_{\mathrm{F-M}},$$

where α ~1/137 is the fine structure constant, $|(l_i 010 | l' 0)|$ corresponds to the coupling of the angular momenta described by the Clebsch-Gordan coefficients. The term $C_{\mathrm{F-M}}$ is the Fried-Martin factor [215], given by

$$C_{\mathrm{F-M}} \equiv \left(\frac{A + Z^{\bar{p}}_{eff} m_{\bar{p}}}{A + m_{\bar{p}}} \right)^2,$$

corresponding to a correction due to the center-of-mass motion of the nucleus.

The factor $Z^{\bar{p}}_{eff}$ corresponds to the effective charge seen by the antiproton, which depends on the number of electrons present and the antiproton's distance to the nucleus [204].

The Auger transition rates, corresponding to the emission of one of the bound electrons in the state (n', l') to the continuum l due to the de-excitation of the antiproton are calculated. In this case, the transition rates are [216]

$$\Gamma_{\mathrm{A}} = \frac{q^4}{3\hbar^2}\left|\langle n_f^{\bar{p}}, l_f^{\bar{p}}|\langle n_f^e, l_f^e|\frac{r_<}{r_>^2}|n_i^e, l_i^e\rangle|n_i^{\bar{p}}, l_i^{\bar{p}}\rangle\right|^2 \times \left|\langle l_1 100\,|l_2 0\rangle\langle l' 100|\,l0\rangle\right|^2 \times k,$$

where the superscripts $\bar{p}$ and e correspond to the antiproton and electron, respectively, and k is the number of electrons in the shell. Additionally, $r_<(r_>)$ is the smaller (larger) of r_1 and r_2, the radial variables of $\bar{p}$ and e, respectively.

These rates are written explicitly in the code. As an example, the K-Auger transition rate for ejecting a 1s-electron reads

$$\Gamma^{1\text{ s}-\mathrm{Aug}}_{n_i,l_i\to n_f,l_i\pm1} = \frac{16}{3}\frac{\pi\alpha c}{a_0}\left(\frac{m_e}{M^*}\right)^2\left(\frac{Z_e^*}{Z}\right)^2\frac{y^2}{(1+y^2)}\frac{\exp\left[y\left(4\tan^{-1}y-\pi\right)\right]}{\sinh(\pi y)}\left(R^{n_i,l_i}_{n_f,l_i\pm1}\right)^2,$$

where

$$\left(R^{n_i,l_i}_{n_f,l_f}\right)^2 = |\langle n_f l_f|r|n_i l_i\rangle \times (l_i 010 \mid l_i \pm 1\ 0)|^2\, C_{\mathrm{F-M}}.$$

The variable y corresponds to

$$y \equiv \frac{Z_e^*}{a_0 k_e},$$

where k_e is its kinetic energy at ejection, a_0 is the Bohr radius and Z_e^* is the effective charge seen by the electron. This value is the charge experienced by an electron in a given shell, considering the presence of the nucleus, other electrons and the antiproton. In the neutral atom case, it can be computed with Hartree-Fock calculations [217, 218]. In this code, because the cascade begins after the antiproton has traversed the electron cloud, the effective charge used is the corresponding to the electron shell in neutral Z-1 atom.

In addition to the radiative and Auger rates, the strong absorption widths are included to account for the strong interaction and annihilation probability of the antiproton. This rate is given by

$$\Gamma_s = 4\frac{\pi}{\mu_{\mathrm{N\overline{p}}}}\,\mathrm{Im}\left(a_{\mathrm{N\overline{p}}}\right)\int \mathrm{d}r\rho(r)\left|\psi_{\overline{\mathrm{p}}}(r)\right|^2,$$

as already introduced in Sec. 6.1.3.

To summarise, the transition rates considered that impact the evolution of the antiprotonic cascade are: The radiative transition rate Γ^{rad}, the Auger transition rates corresponding to the removal of the 1s, 2s and 2p electrons: $\Gamma^{1\text{ s}-\mathrm{Aug}}, \Gamma^{2\text{ s}-\mathrm{Aug}}$ and $\Gamma^{2\text{ p}-\mathrm{Aug}}$, respectively, and the strong absorption rates Γ_{str}.

The rate equation in the antiproton sector can therefore be written as

$$\frac{dN_\alpha(t)}{dt} = -\left[\sum_{\alpha'}\Gamma^{\mathrm{rad}}_{\alpha\to\alpha'} + \Gamma^{1\mathrm{s}-\mathrm{Aug}}_{\alpha\to\alpha'}\sum_j f_{1\mathrm{s}(j)}(t) + \Gamma^{2\mathrm{s}-\mathrm{Aug}}_{\alpha\to\alpha'}\sum_j f_{2s(j)}(t) + \Gamma^{2\mathrm{p}-\mathrm{Aug}}_{\alpha\to\alpha'}\sum_j f_{2\mathrm{p}(j)}(t) + \Gamma^{\mathrm{abs}}_{\alpha}\right]N_\alpha(t), \quad (6.5)$$

where α indicates all the possible (n,l) states and $f_{1s(j)}(t), f_{2s(j)}(t)$ and $f_{2p(j)}(t)$ correspond to the electron population in the 1s, 2s and 2p, respectively. Their evolution is determined by the following rates:

- 1s: The electron pick-up rate $\Gamma^{\mathrm{pick.}}_{1s}$ (refilling from neighbouring atoms), the auger electron refilling from shells 2s and 2p ($\Gamma^{\mathrm{KLL}}_{(2s,2s)}$, $\Gamma^{\mathrm{KLL}}_{(2s,2p)}$, $\Gamma^{\mathrm{KLL}}_{(2p,2p)}$, illustrated in Fig. 6.2), the radiative refilling rate from the 2p→1s transition and the electron depletion due to the antiprotonic Auger transition $\Gamma^{1\mathrm{s}-\mathrm{Aug}}_{\alpha\to\alpha'}$.

- 2s: The electron pick-up rate $\Gamma_{2s}^{\text{pick.}}$ (refilling from neighbouring atoms), the depletion from Auger transitions towards the K-shell $\left(\Gamma_{(2s,2s)}^{\text{KLL}} \text{ and } \Gamma_{(2s,2p)}^{\text{KLL}}\right)$.
- 2p: The electron pick-up rate $\Gamma_{2p}^{\text{pick.}}$ (refilling from neighbouring atoms), the depletion from Auger transitions towards the K-shell $\left(\Gamma_{(2s,2p)}^{\text{KLL}} \text{ and } \Gamma_{(2p,2p)}^{\text{KLL}}\right)$ and depletion due to the radiative decay towards the K shell Γ^{rad}.

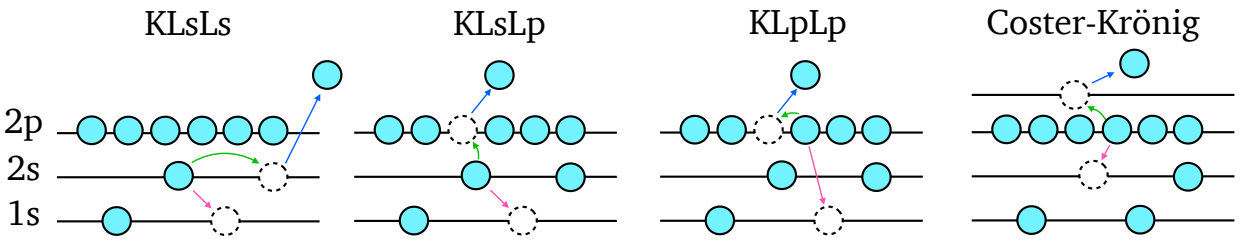

Figure 6.2.: Auger transitions in the electron sector included in the code. The pink arrow depicts a decay to a lower level. The green line corresponds to the energy transfer to the second electron, which is ejected from the atom (blue arrow).

With these considerations, the rate equations in the electron sector are [219]

$$\begin{aligned}\frac{df_{1s(i)}(t)}{dt} =&\Gamma_{2p\to 1s}^{\text{rad}}(1-f_{1s(i)}(t))\{\sum_i f_{2p(j)}(t)\} + \Gamma_{(2s,2s)}^{\text{KLL}}\{1-f_{1s(i)}\}f_{2s(1)}(t)f_{2s(2)}(t)\\ &+\Gamma_{(2s,2p)}^{\text{KLL}}(1-f_{1s(i)}(t))\{\sum_j f_{2s(j)}(t)\}\{\sum_j f_{2p(j)}(t)\}\\ &+\Gamma_{(2p,2p)}^{\text{KLL}}(1-f_{1s(i)}(t))\{\sum_j f_{2p(1)}(t)\}\{\sum_j f_{2p(2)}(t)\},\end{aligned} \tag{6.6}$$

$$\begin{aligned}\frac{df_{2s(i)}(t)}{dt} =&\Gamma_{2s}^{\text{pick.}}(1-f_{2s(i)}(t)) - \Gamma_{(2s,2s)}^{\text{KLL}}\{\sum_i(1-f_{1s(j)}(t))\}f_{2s(1)}(t)f_{2s(2)}(t)\\ &-\Gamma_{(2s,2p)}^{\text{KLL}}\{\sum_j(1-f_{1s(j)}(t))\}\{\sum_j f_{2s(j)}(t)\}f_{2p(i)}(t),\end{aligned} \tag{6.7}$$

$$\begin{aligned}\frac{df_{2p(i)}(t)}{dt} =&\Gamma_{2p}^{\text{pick.}}(1-f_{2p(i)}(t)) - \Gamma_{2p\to 1s}^{\text{rad}}\{\sum_j(1-f_{1s(j)})\}f_{2p(i)}(t)\\ &-\Gamma_{(2s,2p)}^{\text{KLL}}\{\sum_j(1-f_{1s(j)}(t))\}\{\sum_j f_{2s(j)}(t)\}f_{2p(i)}(t)\\ &-\Gamma_{(2p,2p)}^{\text{KLL}}\{\sum_j(1-f_{2p(1)}(t))\}f_{2p(1)}(t)f_{2p(2)}(t).\end{aligned} \tag{6.8}$$

6.2.2. Inputs

For a given isotope, the input is provided in a single file essentially consisting of the initial conditions of the cascade. The parameters are:

- N: Energy level where the calculation of the cascade begins.

- α: Free parameter that determines the initial l distribution of the $\bar{p}$.
- F1S00A(B): Initial population probability of electron A and electron B in the 1s orbital.
- F2S00A(B): Initial population probability of the electrons (A and B) in the 2s orbital.
- F2P00A(B,C,D,E,F,G): Initial population probability of the electrons (A, B, C, D, E, F) in the 2p orbital.
- XFILL: Radiative electron refilling rate of the transition 2p$\rightarrow$1s.
- XKLSLS, XKLSLP, XKLPLP: Auger refilling rates in the 1s, 2s and 2p orbitals, respectively.
- XPKS, XPKP: Pick-up rate in the 2s and 2p orbitals.
- XCK: Coster-Krönig rate.

Additional isotope-specific parameters are hard-coded:

- The atomic mass, in MeV.
- The atomic number Z.
- The electron configuration of the neutral atom.
- The effective charge seen by the electrons of the atom with charge Z-1. This is an approximation to account for the screened nuclear charge due to the $\bar{p}$ presence.

6.2.3. Cascade Code Flowchart

Fig. 6.3 shows a scheme with the main functions of the code. Each of these is described :

- Main: Initializes the cascade by calling the main functions. Declaration and definition of the matrix where the calculations are stored.
- DIST: Computes the initial antiprotonic population distribution according to $P(l) = (2l+1)e^{\alpha l}$, where $l \epsilon$ [0, l=N_0-1].
- TRR: Computes the $\bar{p}$ transition rates from n_i, l_i to all possible n_f, l_f as described in eq. (6.5).
- ECONF: Computes the evolution of the 1s, 2s and 2p electron configuration according to eqs. (6.6), (6.7) and (6.8) by considering the refilling rates and transition rates of the $\bar{p}$.
- TXIN: Produces the four output files: XPOP.DAT, EPOP.DAT, XRAY.DAT and NABS.DAT.

6.2.4. Outputs

The outputs of the code consist of four files: The X-ray transition spectrum, XRAY.DAT, consisting of transitions Δn_1 ($n \rightarrow n-1$) to Δn_5 ($n \rightarrow n-5$); the 1s, 2s and 2p electron configuration evolution at each antiprotonic transition step (EPOP.DAT); the antiprotonic population evolution at each (n, l) state (XPOP.DAT) and the annihilation probability at each (n, l) (NABS.DAT).

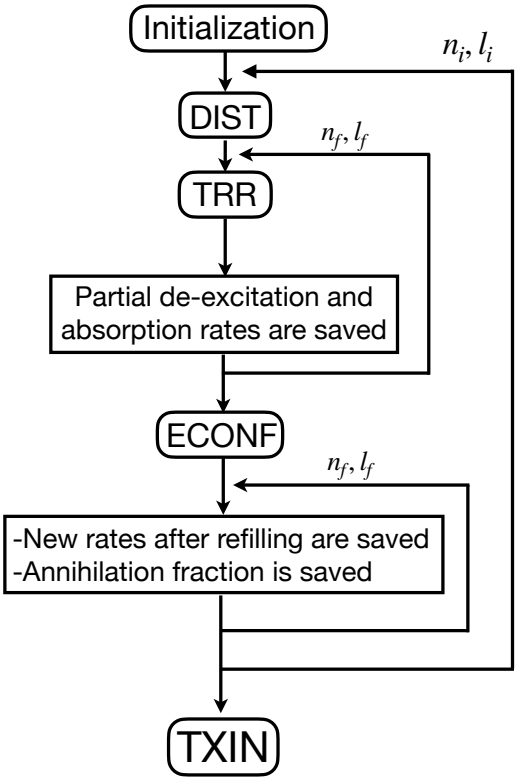

Figure 6.3.: Flowchart of the cascade code.

6.3. Code Benchmarks

The initial study with the cascade code consists of producing benchmarks with existing data. To that end, the X-ray spectra of ^{176}Yb, ^{124}Sn, ^{48}Ca and ^{40}Ar measured at LEAR was used[2].

The choice of ^{176}Yb is based on the comprehensive study done by R. Schmidt *et al.* [64] who used a cascade code based on a work by M. Leon [184] to deduce the capture parameters of the antiproton as well as the neutron density diffusion parameter (see below). In his work he reported the input parameters he used for his cascade calculations to reproduce the X-ray yields.

One important milestone that will be measured at PUMA is the isotopic chain of tin, which makes the existing data of ^{124}Sn [220] a natural choice to test the code.

Finally, a benchmark of ^{48}Ca and ^{40}Ar provides information about the suitability of the code in the lighter mass region of the nuclear chart. Importantly, the existing X-ray spectrum of ^{40}Ar was measured at low pressure [204, 221], where the electron refilling is highly suppressed, as it will be the case of the antiprotonic atoms produced at PUMA.

6.3.1. ^{176}Yb

Context

The benchmark of ^{176}Yb is based on the results shown by R. Schmidt *et al.* [64]. In the mentioned work, the X-ray spectrum of antiprotonic ^{176}Yb was measured and correlated with the X-ray yield resulting from the cascade code. As a result, the capture parameter α that agrees best with the data

[2]The datapoints of the plots shown throughout this section are explicitly shown in Appendix A.

was deduced in addition to the diffuseness of the neutron density t_n. The proton density parameters c_p and t_p (half-density radius and diffuseness, respectively) were obtained from the model *'a'* of Ref. [222] and the difference c_n-c_p=0.13 fm was derived from HFB calculations of ^{208}Pb [223]. Furthermore, the scattering length $a = (1.53 + i\ 2.5)$ fm calculated by C. Batty [205] was used, and the electron configuration of the lower shells 1s, 2s and 2p were assumed to be filled.

The measurement was performed at CERN with antiprotons of 414 MeV/c provided by LEAR, which were stopped in a ^{176}Yb target of 324 mg/cm^2 thickness. Afterwards, the emitted X rays were detected with two germanium detectors.

The reported value of α, with the cascade calculation started at the energy level N=20, is α=0.092$\pm$0.008. Similarly, the difference of the neutron and proton density diffuseness was best adjusted to $t_n - t_p$=(0.71$\pm$0.01) fm.

Calculations

To benchmark the experimental data and numerical findings, the adjusted and fixed parameters were used as input. In addition, the strong absorption widths were calculated numerically [224] by introducing the neutron and proton two-parameter Fermi distributions as well as the scattering length. These widths were then included in the cascade code, as shown in Fig. 6.4.

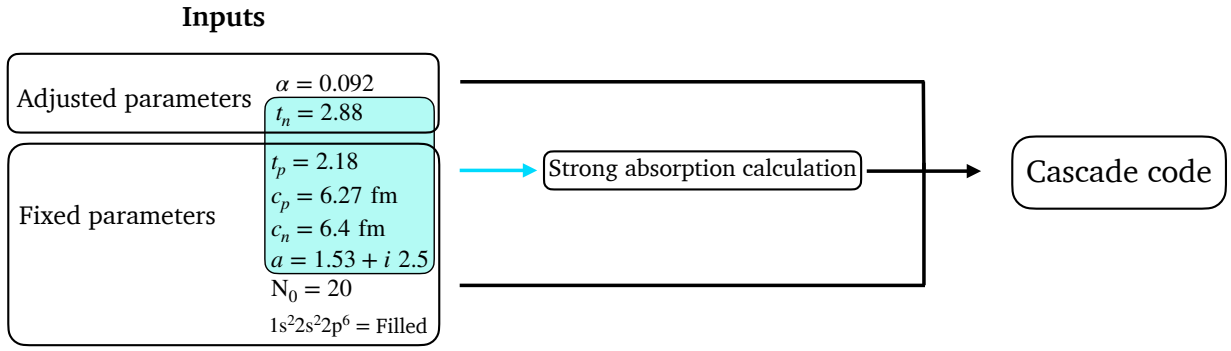

Figure 6.4.: Inputs and flowchart calculation for ^{176}Yb. The shadowed parameters were used to calculate the strong absorption widths.

The comparison between the experimental X-ray yields; the calculated spectrum by Schmidt *et al.* and the benchmark are shown in Fig. 6.5. The numerical values of the calculated data from Schmidt *et al.* were scanned with a plot digitizer software [225] and an uncertainty of 1% was assigned to the extracted X-ray relative intensities. Both calculations show good agreement (within 91%) for the X-ray yields, justifying the assumption of a statistical population of the angular momentum at N=20.

Each curve (Δn=1, 2, 3, 4 and 5) displays the relative X-ray yields normalized to the transition 12$\rightarrow$11. The sharp drop of intensity in the transition 9$\rightarrow$8 corresponds to the high probability of absorption of the antiproton when lying on the n=9 orbital, competing favourably compared to the X-ray decay.

This effect is further seen in Fig. 6.6, where the antiprotonic population probability at each step of the cascade is shown. The left figure shows its evolution as the Δn de-excitation progresses (curves) as a function of the angular momentum quantum number l. On the right figure, the rapid development of the cascade towards circular states (n, $l = n - 1$) is emphasized. Additionally, the inset displays the total population probability at each n level (red curve) together with the total annihilation probability (blue curve). The small annihilation probability of $\sim$ 10% at the beginning of the cascade corresponds to the antiprotonic population at low l, where the overlap of the antiprotonic s- and p- wave functions with the nucleus is the largest. Unlike the large percentage of antiprotonic

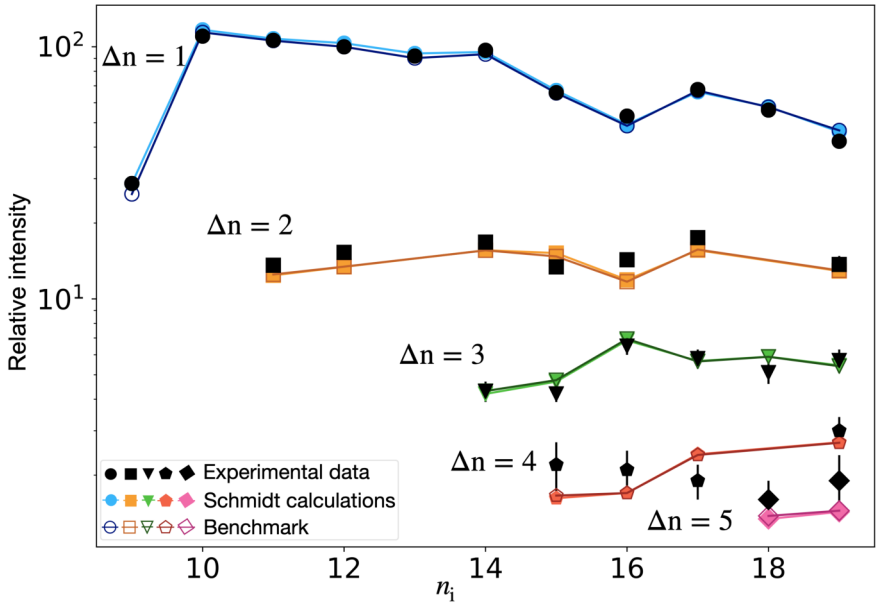

Figure 6.5.: Benchmark of the cascade code with antiprotonic ^{176}Yb with initial parameters N_0=20 and α=0.092. The black markers show the experimental X-ray yields. Each curve corresponds to the transitions $n_i \rightarrow n_i - \Delta_i$, normalized to the transition Δn=12→11.

annihilations at the circular levels, these annihilations occur in the interior of the nucleus and need to be accounted for as a correction factor in the data analysis of PUMA.

The 40% drop of the initial antiprotonic population (red curve in the insert of Fig. 6.6) is related to the increase at lower levels (n=11 to n=15), where it spreads through transitions $\Delta n \geq 2$.

6.3.2. ^{124}Sn

Context

A similar approach was used to benchmark the code with the experimental values of ^{124}Sn measured by R. Schmidt *et al.* [220]. The same experimental method and setup as in the case of ^{176}Yb was used. The proton half-density radius and diffuseness parameters were measured from muonic X-rays [226] to be $c_p = 5.532$ and $t_p = 1.995$, respectively. Based on HFB calculations using the SkP force [227], the neutron half-density radius was chosen $c_n = c_p$. The best fitting value of α was found to be α=0.162±0.017 while the density diffuseness parameter difference was adjusted to $t_n - t_p$=0.19±0.12 [228]. The calculated X-ray yield was not published in this case, therefore the comparison is performed against the experimental values.

Calculations

Using the reported parameters as inputs of the cascade code, the experimental X-ray yields are compared to the numerical output in Fig. 6.7. In this calculation, no initial energy level N_0 was reported. The benchmark run was produced with N_0 =20, where the results show an excellent agreement with the experimental values for Δn=1, Δn=2 and Δn=3 with a systematic discrepancy of 70% with $\Delta n = 4$. This discrepancy could be related to the unknown initial N_0 that yield the reported alpha by Schmidt *et al.* (α=0.162±0.017). Further analysis is performed to obtain the initial conditions that best fit with the data by correlating N_0 and α and a comparison of the α value found is presented (see Sec. 6.4).

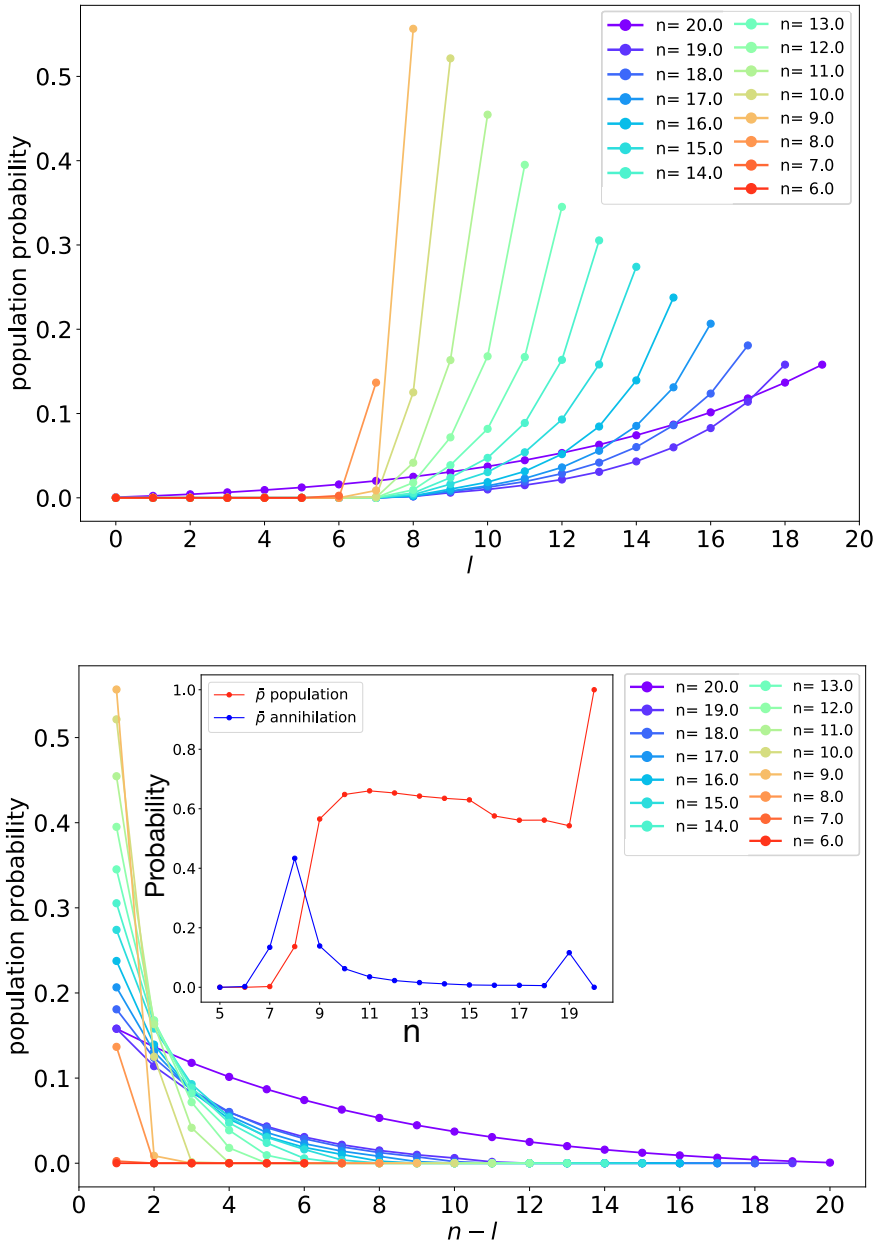

Figure 6.6.: Top: Antiprotonic population at each step of the cascade in ^{176}Yb, as a function of the angular momentum. Bottom: The same quantity as a function of $n - l$. The inset shows the evolution of the population (red) and annihilation probability (blue) as a function of the cascade level n. In these cases, the probabilities are summed over the quantum number l.

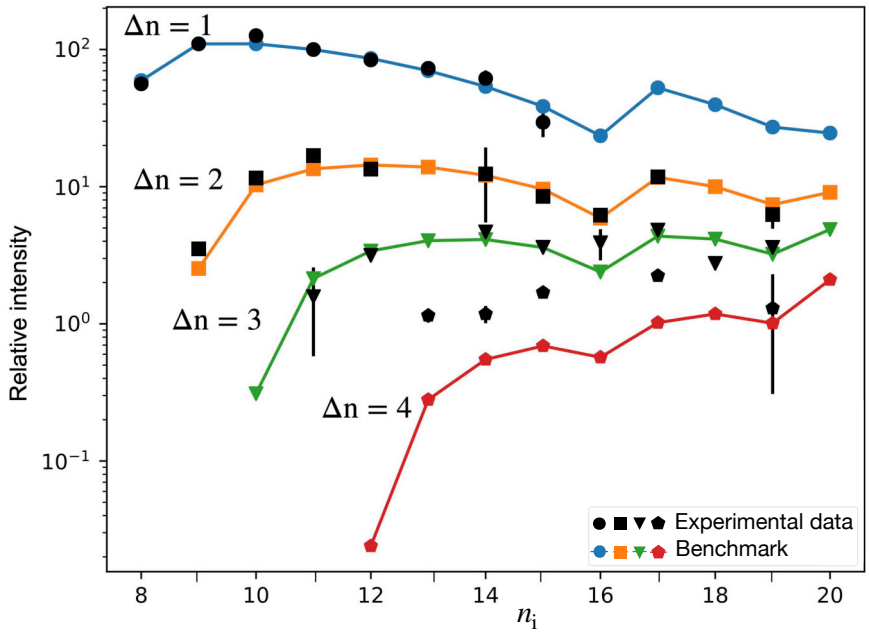

Figure 6.7.: Benchmark of the cascade code with antiprotonic ^{124}Sn. The initial parameters of the cascade are N_0=20 and α=0.162. The black markers show the experimental X-Ray yields. Each curve corresponds to the transitions $n_i \rightarrow n_i - \Delta_i$, normalized to the transition Δn=10$\rightarrow$9.

6.3.3. ^{48}Ca

Context

This benchmark is done with respect to the measurements performed at LEAR and cascade calculations done by is Hartmann *et al.* [229]. The experimental setup consists of a beam of antiprotons with an initial momentum of 106 MeV/c impinging on a target of 46.9 mm/cm^2 thickness. Once again, the antiprotonic X-rays were detected with high-purity-Ge detectors. In this case, however, due to the low charge of the Ca isotopes, the transition energies are smaller than those of Yb and Sn. As a consequence, less transitions were detected with respect to the previous cases (see Fig. 6.8) and an average of the X-ray yields measured with antiprotonic ^{40}Ca, ^{42}Ca, ^{43}Ca, ^{44}Ca and ^{48}Ca is reported together with a mean α=0.129$\pm$0.019, with the cascade started at N_0=20.

The proton and neutron half-densities used for ^{48}Ca were taken equal to 3.56 fm and the proton-density diffusion t_p=2.18 fm. Furthermore, the neutron-density diffusion was fitted to the X-ray data, obtaining $t_n - t_p$=0.46$\pm$0.13 fm.

Calculations

The cascade calculation was performed with ^{48}Ca. The X-ray yield calculated is shown in Fig. 6.8. The calculated values by Hartmann *et al.* were also scanned with a plot digitizer tool [225]. The error assigned in this case (4%) is higher than for ^{176}Yb. The reason is that a shift of this percentage was observed at the normalised transition: The tool was calibrated within 1% error according to the axis, but expected value of this transition (100) was shifted by 4%.

The yields of the three types of transitions $\Delta n1$, $\Delta n2$ and $\Delta n3$ obtained are within 90% agreement with the experimental values, as well as with the calculated values from Hartmann *et al.*, and in this case, too, the calculations are further analysed in Sec. 6.4.

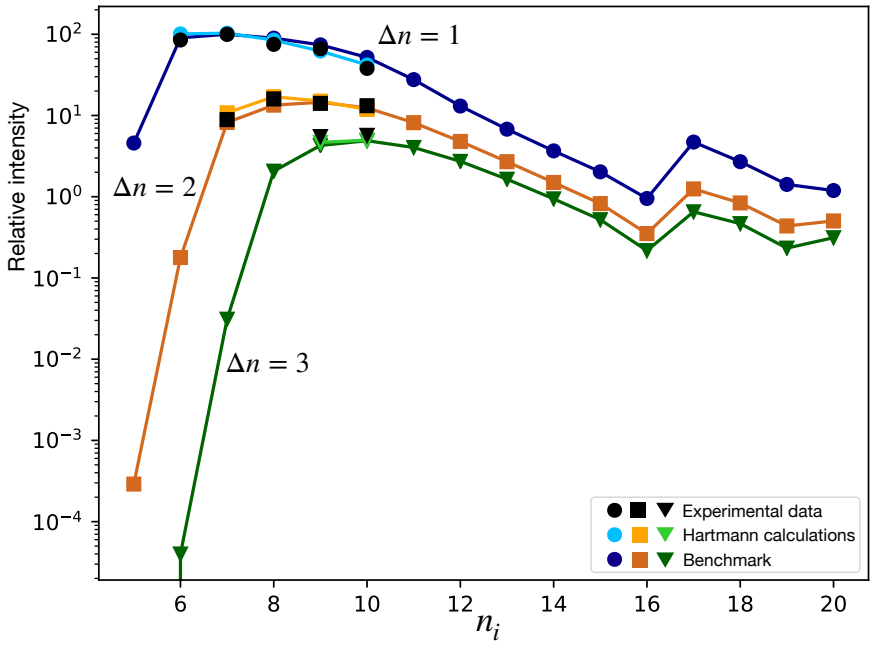

Figure 6.8.: Benchmark of the cascade code with antiprotonic ^{48}Ca with initial parameters N_0=20 and α=0.129. The black markers show the experimental X-Ray yields. Each curve corresponds to the transitions $n_i \rightarrow n_i - \Delta_i$, normalized to the transition 7→6.

6.3.4. ^{40}Ar

Context

A final benchmark of the code consists of comparing the X-ray spectrum of antiprotonic Argon at low pressure. The ionization of antiprotonic atoms in diluted noble gases (Ar, Xe and Kr) was studied at LEAR [204, 221]. The main objective of the experiment was to correlate the X-ray spectrum with the depletion of the electron shells, as it was deduced that a pressure lower than 100 hPa was sufficient to remove the refilling of electrons. The available data consists of only the circular transitions, shown in Fig. 6.9.

It was deduced in [221] that the antiproton has enough energy to remove all the electrons via Auger transitions by the time it reaches the level n=40, except for the ones in the K-shell, with calculated ionization energies of 3.5 keV and 3.8 keV. The observed suppression of the lines in the transitions 17→16 (ΔE=3.52 keV) and 16→15 (ΔE=4.25 keV) was interpreted as a signature of electron shell depletion, as these two transitions are the first ones that overcome the ionization energy of the 1s electrons. However, in a later study of the same data [204] with Multiconfiguration Dirac-Fock calculations (MCDF) [230], the ionization energies of these electrons were deduced to be 3659 eV and 3947 eV. As a consequence, the energy of the transition 17→16 is not sufficient to remove the first electron, unless at least four additional electrons in the subsequent shells are present: in this case the binding energy of the 1K-shell electrons drops to 3309 eV (see Table 6.1).

Calculations

A first calculation to estimate the suitability of the code to reproduce this spectrum consisted of using the effective charges as seen by the electrons, $Z_{eff.}$, reported by Gotta *et al.* [204] as input in order to compare the electron ionization energies (see Table 6.1). From the table it is observed a discrepancy of 0.4% in the ionization energy of the 1s level when only one electron is present, while

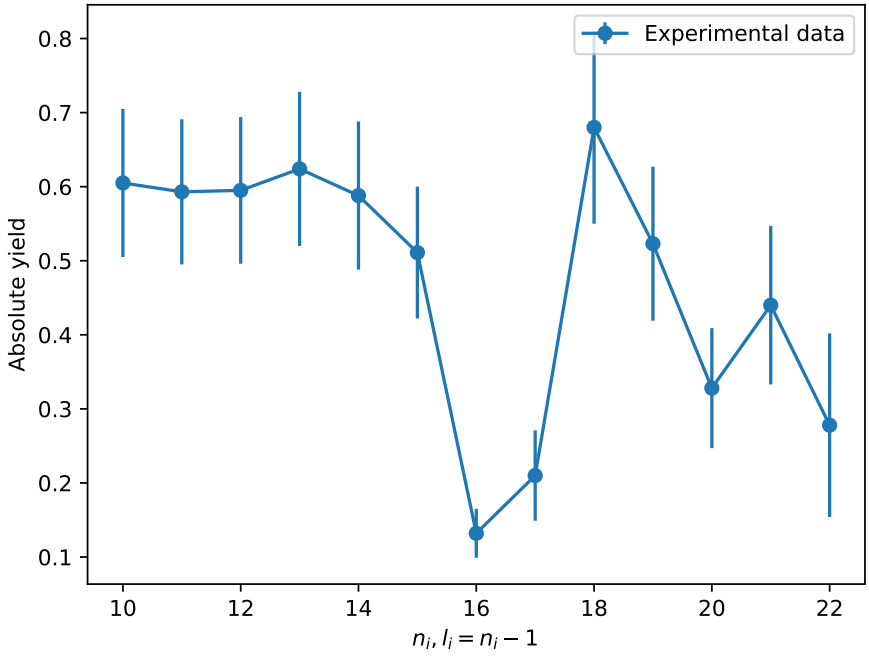

Figure 6.9.: Measured X-ray spectrum of circular states (Δn=1) of antiprotonic ^{40}Ar in a low-pressure gas. Data from [221].

Table 6.1.: Effective charges for different electron configurations and corresponding binding energies of the levels 1s and 2s.

e^- config.		$1s^1$		$1s^2$		$1s^22s^2$		$1s^22s^22p^2$	
Levels	Source	MCDF[a]	Code[b]	MCDF[a]	Code[b]	MCDF[a]	Code[b]	MCDF[a]	Code[b]
1s	Eff. charge	17		16.6		16.6		16.5	
	Bind. E (eV)	3947	3930	3659	3740	3490	3740	3309	3704
2s	Eff. charge					15.4		14.9	
	Bind. E (eV)					806	745	628	755

a. Calculations reported in Gotta *et al.* [204].
b. Binding energies calculated with the cascade code.

it increases up to 11% for the same electron level in the $1s^22s^22p^2$ configuration. In particular, the ionization energy obtained with the code is systematically above the transition energy between the levels 17→16 (ΔE=3.52 keV). On the other hand, it is possible to observe the suppression of the line corresponding to the transition 16→15 (ΔE=4.25 keV), shown in Fig. 6.10.

In this case there were no studies of the antiproton capture, hence the initial conditions are unknown. An initial test run with similar parameters was performed. The initial energy level was kept at N=20 as in the previous two cases, while α was set to 0.1. The neutron and proton half density radius and diffuseness parameters were extracted from HFB calculations with the SIII force.

The code is able to reproduce the X-ray suppression for the transition 16→15, although the same kind of benchmark as for the previous atoms is not possible due to the lack of experimental data. More refined calculations that can accurately reproduce the ionization energy of each electron would be required.

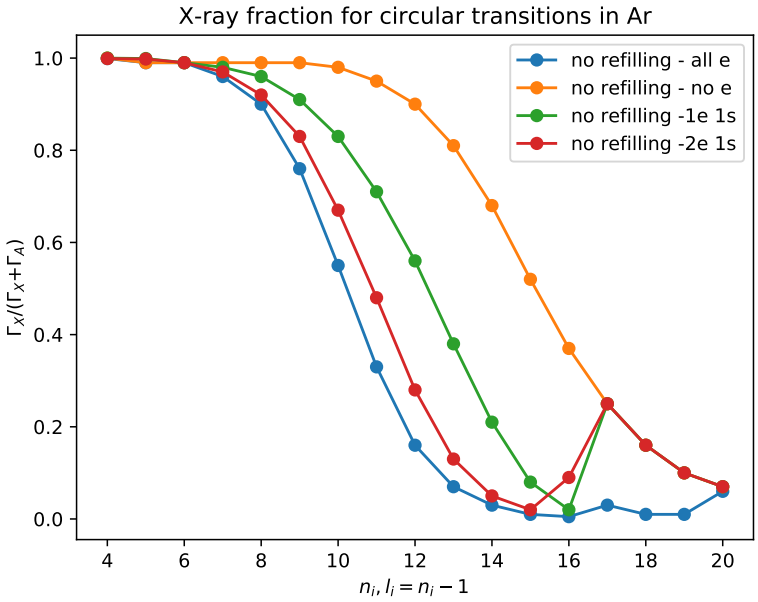

Figure 6.10.: Fraction of radiative circular transitions (Δn=1) of antiprotonic ^{40}Ar calculated with the cascade code.

6.4. Capture Parameters Correlation

The sensitivity of the cascade calculations to the capture parameters is evaluated. The method consists of finding the best agreement among the experimental X-ray spectra (X_{obs}) and the calculated spectra (X_{exp}) with a given set of initial conditions (N, α) by minimizing the χ^2, given by

$$\chi^2 = \frac{(X_{exp} - X_{obs})^2}{m\sigma^2},$$

where σ corresponds to the experimental uncertainties and m is the number of degrees of freedom, corresponding in this case to the number of experimental data points.

The results obtained for ^{176}Yb, ^{124}Sn and ^{48}Ca are shown in Fig. 6.11. For a fixed initial N_0, each red mark corresponds to the appropriate α such that the χ^2 is minimum.

A similar correlation is observed in every case, where the minimum χ^2 is found at lower N_0 as α increases. This means that angular momentum distributions closer to captures in circular states are preferred for lower N_0. This behaviour is expected as the antiproton population tends towards circular states during de-excitation, as explained in Sec. 6.1.2.

It is chosen to fit the points with quadratic functions with parameters p_0, p_1 and p_2 fulfilling

$$\alpha(N) = p_0 + p_1 N + p_2 N^2.$$

The fitted parameters with their errors are given in Table 6.2.

Additionally, in Table 6.3, the α minimum χ^2 found at N=20 are compared to the values reported.

As it can be observed, the calculated χ^2 values of both ^{124}Sn and ^{176}Yb lie within 7.1% of the reported ones. Furthermore, the associated α of ^{176}Yb id within the error reported by Schmidt *et al.*. In the case of Sn, its associate α has a discrepancy of less than 17%. Calcium, on the other hand, shows a higher discrepancy overall, obtaining a difference of 62% in the value of α, which is rooted in the fact that the experimental data is an average of other Ca isotopes as well, as opposed of pure

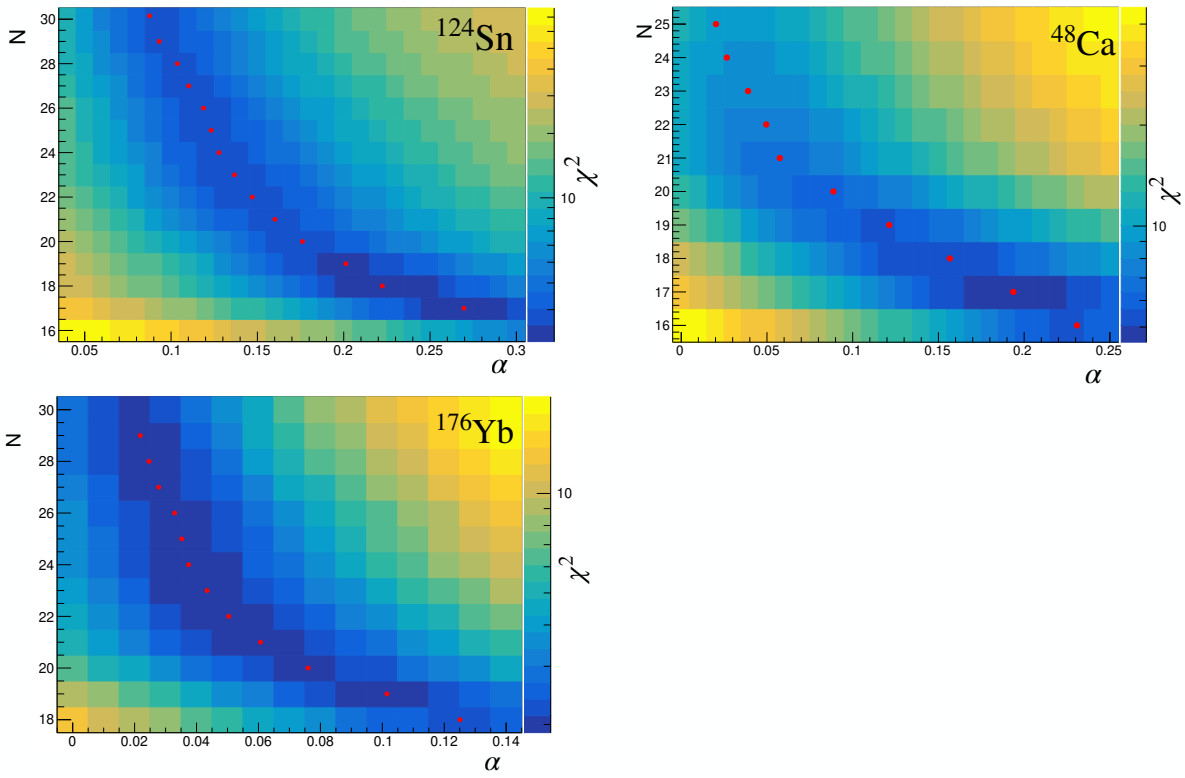

Figure 6.11.: χ^2 minimization of ^{124}Sn (top left), ^{48}Ca (top right) and ^{176}Yb (bottom left).

Table 6.2.: Fitted parameters, where p_0 corresponds to the constant term, p_1 is the linear term and p_2 is the quadratic term.

	^{176}Yb	^{124}Sn	^{48}Ca
p_0	0.76±0.07	0.87±0.07	1.60 ± 0.085
p_1	-0.053±0.006	-0.053±0.006	-0.125 ± 0.008
p_2	0.0009±0.0001	0.0009±0.0001	0.0024 ± 0.0002

^{48}Ca. The found correlations provide a meaningful landscape of initial conditions (N_0, α) where to calculate the cascade in Sn and Ca isotopic chains, subject of Ch. 7.

Table 6.3.: Calculated cascade parameters at N_0=20, α and χ^2 compared with reported.

	Calculated		Reported	
	α	χ^2	α	χ^2
^{48}Ca	0.09	6.1	0.129±0.019	1.1
^{124}Sn	0.19	2.9	0.162±0.017	2.7
^{176}Yb	0.08	2.02	0.092±0.008	1.9

7. Sensitivity of Sn and Ca isotopes

In the following, the sensitivity of the PUMA observable to atomic physics inputs is investigated. To that end, cascade calculations are performed with initial parameters $(N_0,\ \alpha)$ that reproduce the experimental X-ray yields within one unit of the global minimum χ^2, in each case. The same regions are kept for the rest of the Sn and Ca isotopes, respectively. Figure 7.1 shows the chosen regions in both cases.

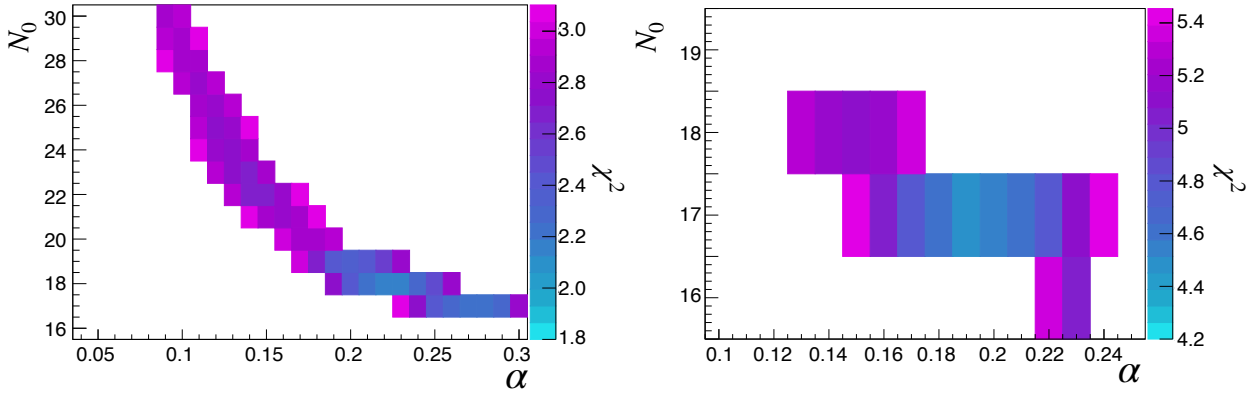

Figure 7.1.: $(N_0,\ \alpha)$ regions chosen to produce the sensitivity calculations for Sn (left) and Ca isotopes (right).

7.1. Annihilation Probability

Each run with initial conditions (N_0, α) calculates the annihilation probability $\omega_{n,l}$ of the antiproton with quantum numbers (n, l), such that the total annihilation density distribution is

$$p_{tot} = \sum_{(n,l)} |\psi_{(n,l)}|^2 r^2 \omega_{(n,l)},$$

where

$$\int p_{tot}(r) dr = 1,$$

and $\psi_{n,l}$ is the radial part of the antiprotonic wave function. The wave function of the antiproton in the center of mass of the antiprotonic atom of charge Z can be described by

$$\psi_{n,\ell}(r) = -\sqrt{\left(\frac{2Z}{na_\mu}\right)^3 \frac{(n-\ell-1)!}{2n(n+\ell)!}} e^{-Zr/na_\mu} \left(\frac{2Zr}{na_\mu}\right)^\ell L_{n-\ell-1}^{(2\ell+1)}\left(\frac{2Zr}{na_\mu}\right).$$

In this case, L_{n-l-1}^{2l+1} are the generalized Laguèrre polynomials, $a_\mu = 4\pi\varepsilon_0\hbar^2/\mu e^2$ is the Bohr radius of the antipoton-nucleus system and

$$\mu = \frac{m_{\bar{p}} m_A}{(m_{\bar{p}} + m_A)},$$

is the antiproton-nucleus reduced mass.
Undere the assumption of a spherical nucleus, the angular part of the wave function does not contribute to the equation since

$$|Y_l^m(\theta,\phi)|^2 = Y_l^{m^*}(\theta,\phi)Y_l^m(\theta,\phi) = 1.$$

The absorption width is then

$$\Gamma = \frac{2\pi}{\mu}\int dr^3 V(\bar{r}) \sum_{(n,l)} |\psi_{n,l}|^2 r^2 \omega_{(n,l)}. \tag{7.1}$$

From eq. (7.1), $V(r)$ is the optical potential, assumed to depend linearly on the densities, as explained in Ch. 6,

$$V(r) = \frac{2\pi}{\mu}\left(\mathrm{a_{\bar{p}N}}\rho_N(r) + \mathrm{a_{\bar{p}p}}\rho_\mathrm{p}(\mathrm{r})\right),$$

Considering the ratio of the absorption widths with either a neutron or a proton, we obtain

$$\frac{\Gamma_\mathrm{n}}{\Gamma_\mathrm{p}} = \frac{\int dr^3 \rho_\mathrm{n}(r) \sum_{(n,l)} |\psi_{n,l}|^2 r^2 \omega_{(n,l)}}{\int dr^3 \rho_\mathrm{p}(r) \sum_{(n,l)} |\psi_{n,l}|^2 r^2 \omega_{(n,l)}} \mathrm{Im}\left(\frac{\mathrm{a_{\bar{p}n}}}{\mathrm{a_{\bar{p}p}}}\right) \tag{7.2}$$

which, as observed, is directly related to the neutron to proton density distributions.

The gamma ratio is non-zero only where the antiproton distribution overlaps with the neutron and proton density distributions. Under the assumption of point-like particles and zero-range interaction, one can interpret the radius of the annihilation as

$$\langle R_{\bar{p}N}\rangle = \int r^2 |\psi_{n,l}(r)|^2 \,\mathrm{Im}\, V_{\bar{p}N}(r) dr.$$

Figure 7.2 show as an example, the proton and neutron density distributions (ρ_p and ρ_n, respectively) calculated with the Skyrme parametrization SIII (see Sec. 7.2), together with the total wave function density $\rho_\mathrm{\bar{p}}^{(\mathrm{f})}$and the overlap among them.

As it can be seen in the figure, the annihilation of the antiproton with a nucleon involves the inner tail of the total antiprotonic probability density, where the overlaps with the proton and neutron densities probe the tail of the density profiles. The ratio of these two distributions (shaded red and yellow areas), and therefore the annihilation ratio, provides a measure of the neutron-to-proton density distributions in this region.

It should be noted that the densities are calculated in the center of mass of the nucleus while the wave function of the antiproton is calculated in the center of mass of the antiprotonic atom, leading to an inconsistency due to the difference of the reference frames. However, this effect is negligible for the heavy isotopes (Sn and Ca) considered in this case.

7.2. Density Distributions

The calculation of the proton and neutron density profiles is performed with the HFBRAD code [231], that solves closed shell approximations assuming spherical nuclei with the Hartree-Fock-Bogolyubov method (HFB), using different Skyrme force parametrizations. The numerical method consists of the direct integration of the HFB equations in the coordinate representation. The Skyrme effective interaction is described by the 2- and 3- body potential [232]

$$V = \sum_{i<j} V\left(\mathbf{r}_i, \mathbf{r}_j\right) + \sum_{i<j<k} V\left(\mathbf{r}_i, \mathbf{r}_j, \mathbf{r}_k\right).$$

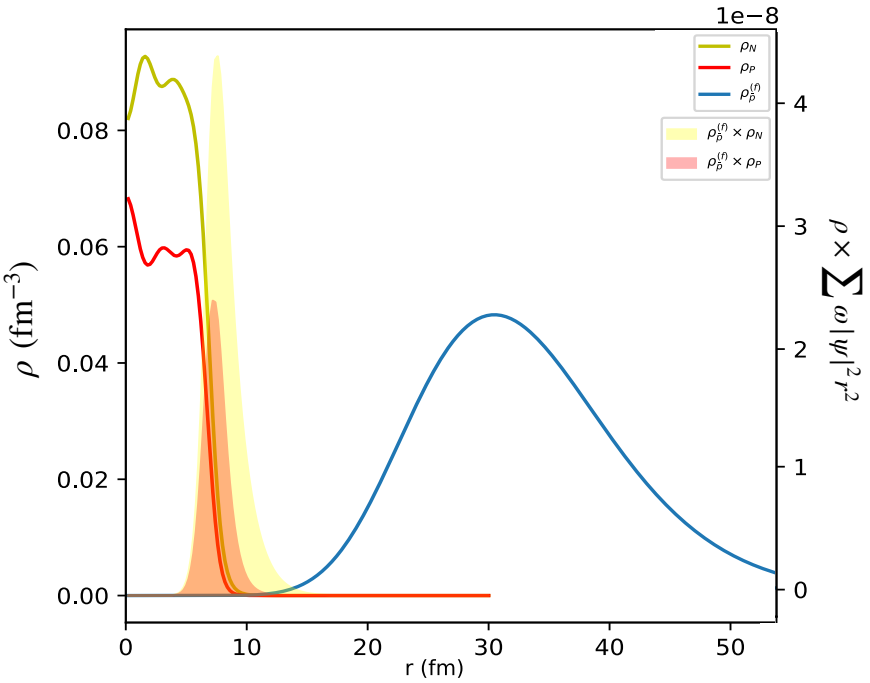

Figure 7.2.: Proton and neutron densities distribution (ρ_P and ρ_N respectively, modelled with SIII), together with the total probability density weighted by each state's contribution $\rho_{\bar{p}}^{(f)}$. The overlap between the antiprotonic density function with ρ_N and ρ_P are the shaded yellow and red areas, respectively.

The 2-body part is parametrized according to [231]

$$\begin{aligned} V_{12} =& t_0 \left(1 + x_0 P_\sigma\right) \delta + \frac{1}{2} t_1 \left(1 + x_1 P_\sigma\right) \left(\mathbf{k}'^2 \delta + \delta \mathbf{k}^2\right) + t_2 \left(1 + x_2 P_\sigma\right) \mathbf{k}' \cdot \delta \mathbf{k} \\ &+ \frac{1}{6} t_3 \left(1 + x_3 P_\sigma\right) \rho^\gamma \delta + i W_0 \left(\sigma_1 + \sigma_2\right) \cdot \left(\mathbf{k}' \times \delta \mathbf{k}\right), \end{aligned}$$

as a short-range expansion of finite range interactions. Here, δ is a short notation for $\delta\left(\mathbf{r}_1 - \mathbf{r}_2\right)$; the terms $\mathbf{k}$ and $\mathbf{k}'$ are the relative momentum operators acting on the wave functions on the right and on the left, respectively and $P_\sigma = (1 + \sigma_\mathbf{1} \cdot \sigma_\mathbf{2})/2$ is the spin-exchange operator. The parameters t_0, t_1, t_2, t_3, x_0, x_1, x_2, x_3 and W_0 depend on choice of the Skyrme force. These are adjusted to experimental binding energies and radii and nuclear matter saturation properties [30].

To ensure that our conclusions are not dependent on the chosen Skyrme interaction, three distinctive Skyrme forces have been chosen for this study: SIII [233], SLy4 [234] and SKI5 [235]. The parametrization SIII is particularly successful in reproducing the spectroscopic properties of spherical nuclei. It additionally reproduces the N-Z dependence of the binding energy [236], although its incompressibility is said to be too large [233]. The parametrization Sly4 was built for astrophysical use, in particular to optimize the description of neutrons stars and the Equation of State. In this case, an incompressibility of 230 MeV of symmetric nuclear matter is set. It was also optimized to reproduce correctly pure neutron matter and a good reproduction of the saturation point of the symmetric infinite nuclear matter with no constraint on the surface properties. Finally, SKI5 was built to optimize the behaviour for the isotope shifts in the Pb region, which was achieved by optimising the term related to the spin-orbit contribution.

The corresponding parameters of each of these forces are shown in Tab. 7.1 and Fig. 7.3 displays the computed proton (left) and neutron (right) density distributions in each case.

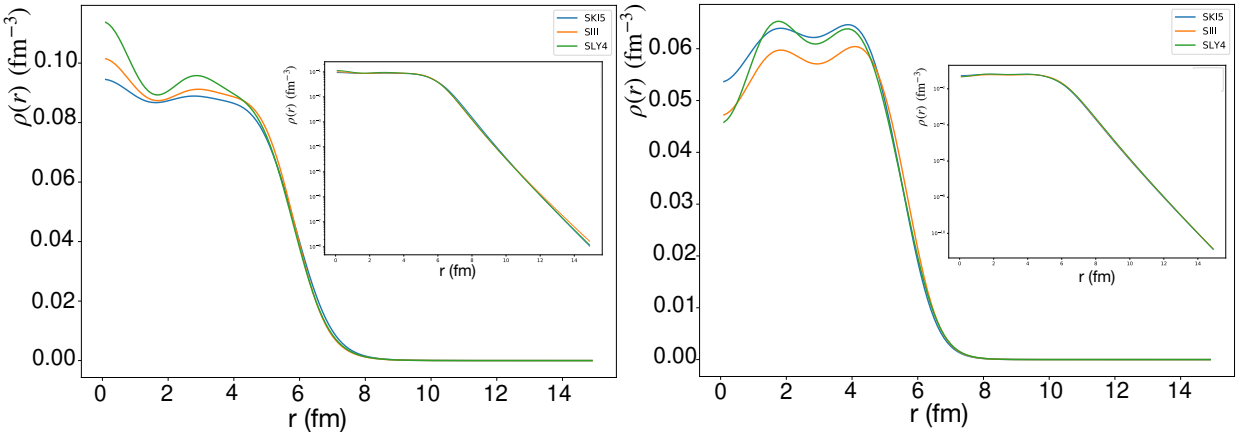

Figure 7.3.: Comparison of the ^{132}Sn neutron (left) and proton (right) densities calculations with the Skyrme parametrizations SIII, SLy4 and SKI5. The inserts show the densities in logarithmic scale.

Table 7.1.: Values of the three different Skyrme parametrizations compared.

	SIII	SLy4	SKI5
t_0	-1128.75	-2488.913	-1772.91
t_1	395.	486.818	550.84
t_2	-95.	-546.395	-126.685
t_3	14000.	13777.	8206.25
x_0	0.45	0.834	-0.1171
x_1	0.	-0.344	-1.3088
x_2	0.	-1.	-1.0487
x_3	0.	1.354	0.34
γ	1.	1/6	1/4
W_0	130.	123.	120.
$t_0\prime$	-248.5	-283.3	-325.3

7.3. Calculations

7.3.1. Annihilation Probabilities

The cascade calculation is run systematically for each pair of $(N_0,\ \alpha)$ shown in Fig. 7.1. For a given run, the annihilation probability $\omega_{n,l}$ at each antiprotonic state (n, l) is saved. Figure 7.4 shows the annihilation probability obtained for every (N_0, α) run at the circular states $(n, l = n - 1)$ and next-to-circular states $(n, l = n - 2)$ of Sn isotopes with a given Skyrme interaction (SIII).

It can be seen in this figure that the annihilation probability peaks at the circular state $(7, 6)$ consistently, and it decays from 0.6 for ^{104}Sn towards 0.45 for ^{132}Sn, in which a higher contribution from the state $(8, 7)$ is observed. The shift towards annihilating in higher energy levels is consistent with increase of the nuclear mass and as a consequence the overlap between the antiproton and nuclear density distributions occurs at a higher radius. The contribution from next-to-circular states amounts to 10% and the slight increase at higher mass is related to the probability of the antiproton not fully converging to the circular states.

In the case of Ca isotopes (Fig. 7.5), the dominant antiprotonic state where the annihilation occurs is the circular level $(5, 4)$. Similarly as before, the increase in the mass of the isotope increases the

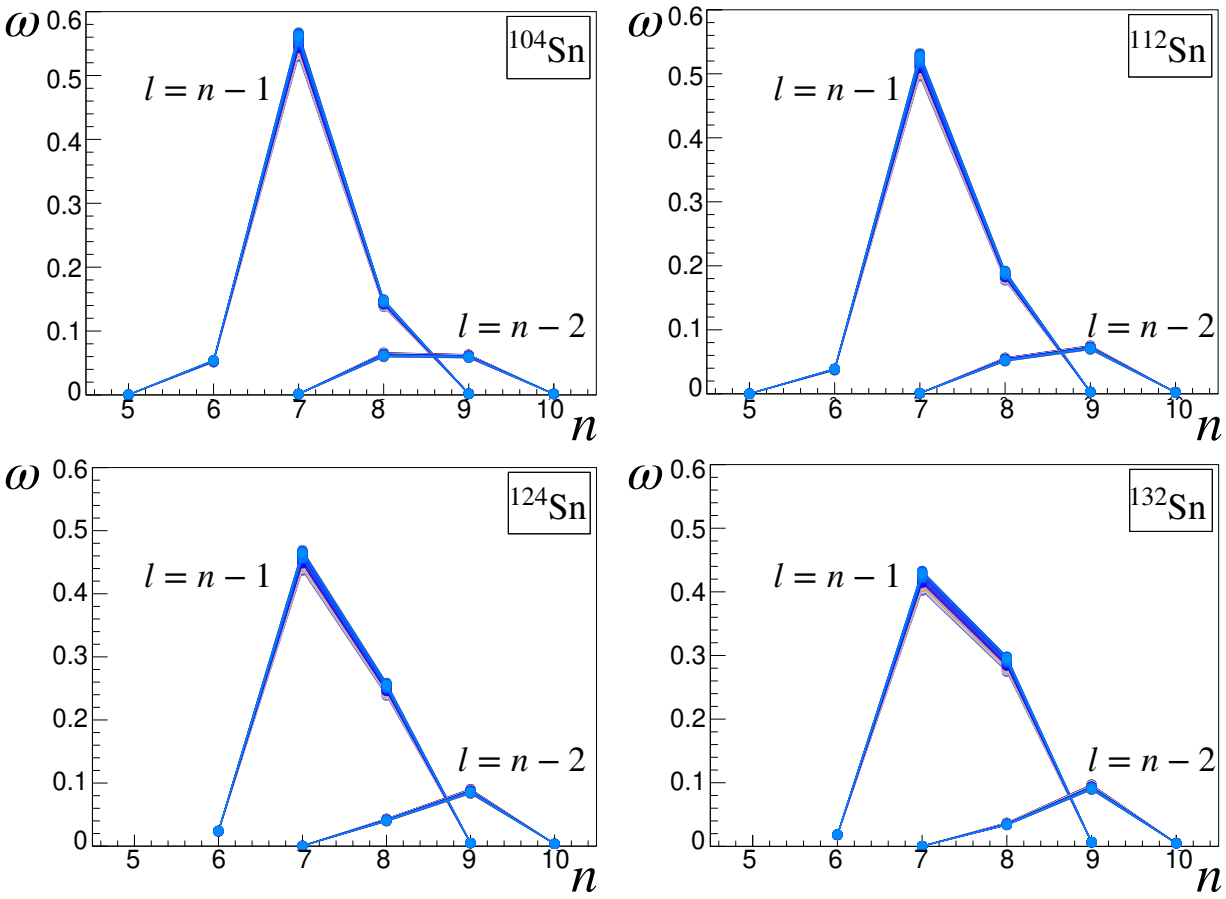

Figure 7.4.: Weight in the circular and l=n-2 states for the Sn isotopes studied for all the (N_0, α) pairs considered. The calculation shown was performed with the SIII parametrization.

probability of an earlier annihilation in the state $(6, 5)$, which amounts to 5% for ^{54}Ca.

It is also important to notice that the variation of the initial parameters (N_0,α) show a stable and consistent output. The largest spread of results is in the order of 10% at the most probable annihilation level in all the computed isotopes, implying an independence of the annihilation process from the initial conditions considered for the capture once the distribution is constrained by the X ray decay pattern.

7.4. Gamma Ratios

The computed weights are used to calculate the neutron-to-proton annihilation ratios. At a first stage, the total antiprotonic probability density is computed. As an example, the density obtained from the calculations with ^{124}Sn with the SKI5 paramterization is shown in Fig. 7.6.

Even though the weights of non-circular states are significantly lower, a closer look at their contribution is performed by computing the overlap between the matter density and antiprotonic density distributions, shown in Fig. 7.7. The left-hand-side figure shows, in logarithmic scale, the antiprotonic states (n, l) of the contributing circular states. Additionally, the figure in the middle adds the next-to-circular states, and finally, the right-hand side plot shows all the contributions. It can be observed in this case, that the antiprotonic states with l<n-2 have a non-negligible contribution that shifts the absorption widths towards the core of the nuclei. The effect that these contributions add to

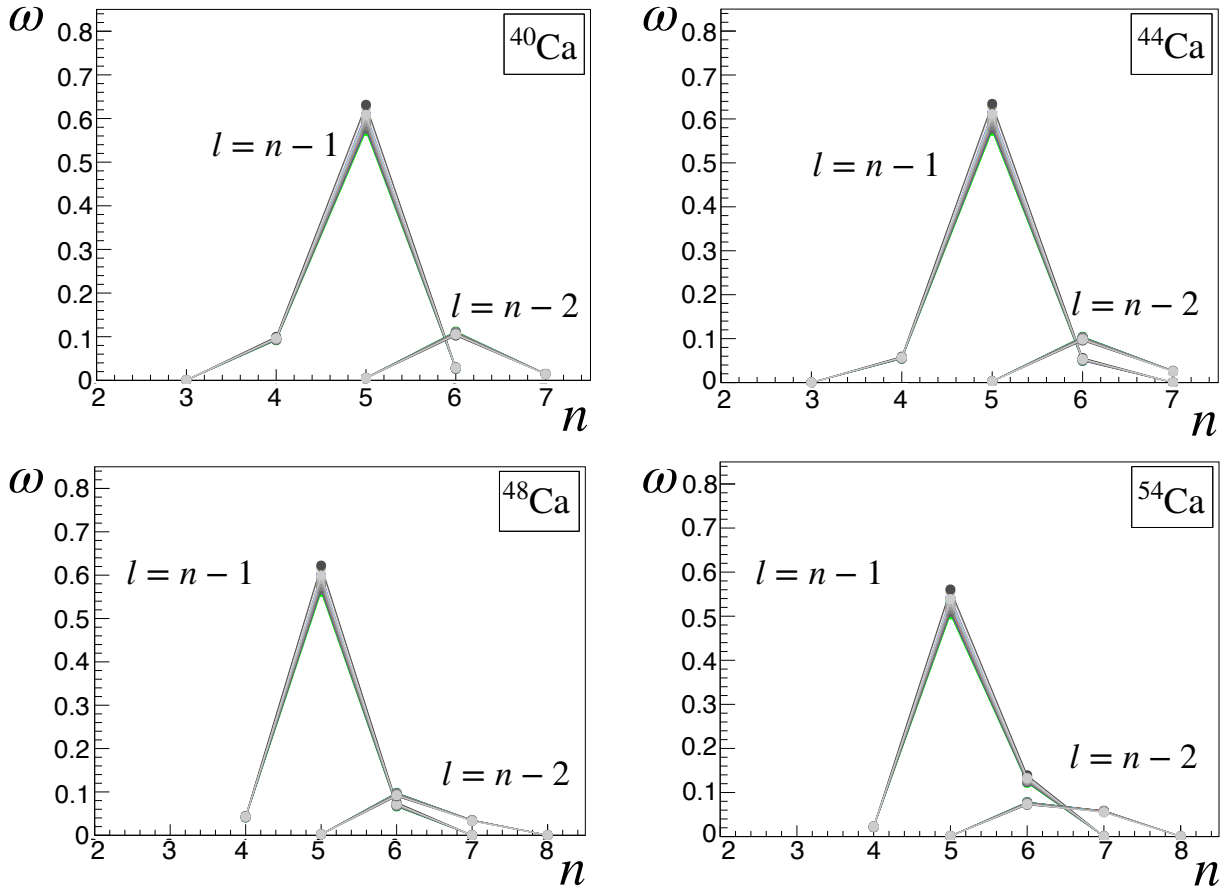

Figure 7.5.: Weight in the circular and l=n-2 states for the Sn isotopes studied for all the (N_0, α) pairs considered. This calculation was performed with SIII.

the computation of the gamma ratios is studied next.

7.4.1. Sensitivity to Skyrme parametrizations

The gamma ratios as defined in eq. (7.2) are computed for the Sn and Ca isotopes, with the neutron and proton density parametrizations SIII, SKY5 and SLy4. Figure 7.8 shows the calculations obtained for ^{104}Sn, ^{112}Sn, ^{124}Sn and ^{132}Sn. The figure on the left displays the gamma ratio calculated with the contributions of the circular states only (∼75% of the total set of states), while the middle figure includes the next-to circular as well. The right figure shows the result for all states with the weighted annihilation probability, namely considering as well the lower l states. Each point represents the gamma ratio obtained for a given set of capture parameters (N_0, α).

The figure shows a clear sensitivity of the gamma ratio to the nuclear surface, evidenced by the increasing values observed for larger isotopic masses. However, it is also observed that the contribution to the annihilation probability of the lower l states (right side), in the range of 10%-12%, shifts and broadens significantly the gamma ratios, losing the sensitivity to the tail. This requires the development of a model that fully describes the capture of the antiproton and cascade through the electron cloud, which is not treated in this model.

A comparison with existing antiproton-nucleon annihilation data [71, 237] is not possible, as the radiochemical method was used to determine the halo factor, which depends on the ratio of produced radioactive daughter nucleus to determine the annihilation ratio (see Sec. 1.3.4). This

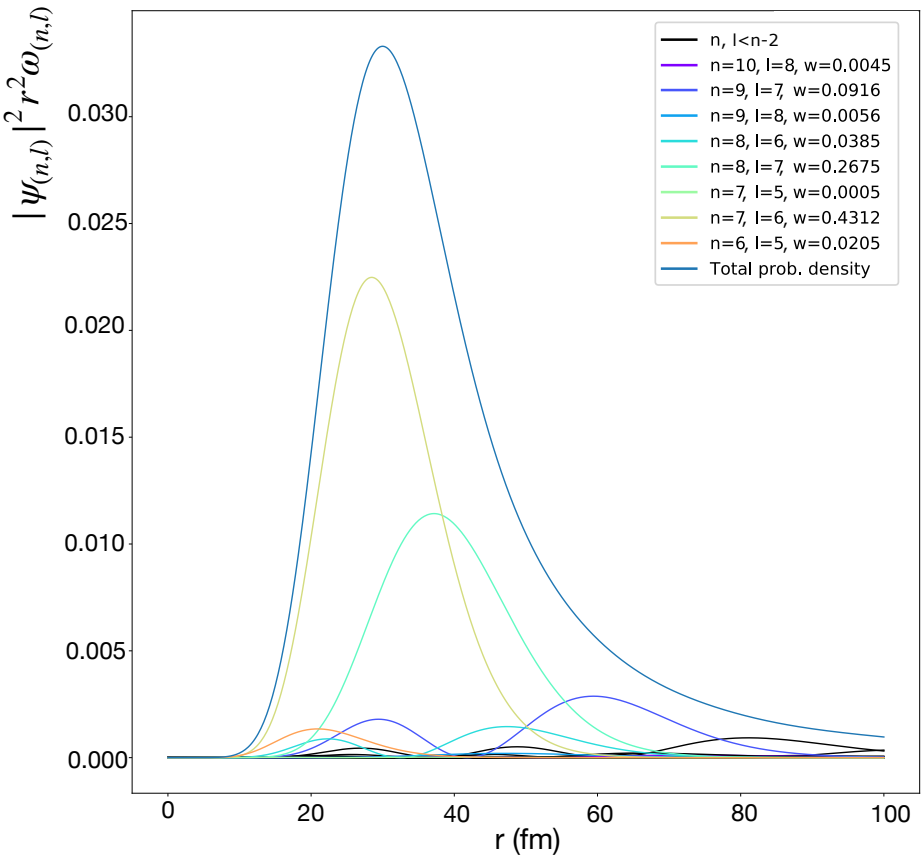

Figure 7.6.: Weighted antiprotonic wave functions with the sum of the weighted contributions.

method, in addition, probes a complementary region ($\sim$ 1 fm farther) to the one proposed by the PUMA experiment.

7.4.2. Sensitivity to neutron skin

To estimate the sensitivity to the diffusion of the neutron density tail t_n, the densities calculated with HFBRAD are fitted with a two-parameter Fermi distribution, given by

$$\rho = \frac{\rho_0}{1 + e^{\frac{r - c_n}{t_n}}},$$

where c_n is the half density radius, $t_n = 4ln(3)d_n$ is the neutron skin, related to the diffuseness parameter d_n, and ρ_0 is a normalization factor with respect to the number of neutrons and protons. The skin term is then increased by 0.1 fm, which corresponds to a variation in the order of 5% to 10% from the fitted values, depending on the isotope mass. The gamma ratio is computed with this new distribution for both Ca and Sn isotopes. Figure 7.9 shows the result obtained with the SIII Skyrme parametrization. The upper half of the figure corresponds to Sn isotopes, while the lower half corresponds to Ca.

On the left-hand side of the figure, the result as a function of the mass (top: Sn, bottom: Ca) is shown. On the right-hand side, the same result is shown as histograms, one per isotope considered. The mean value of each distribution is shown as a vertical, dashed line. The isotopes show a separation that decreases as a function of the mass. The mean value ranges from 7% difference at ^{104}Sn to 0.9% for ^{132}Sn. In the case of Ca, the gamma ratio difference at ^{40}Ca is 12.6 %, which decreases to 4.7%

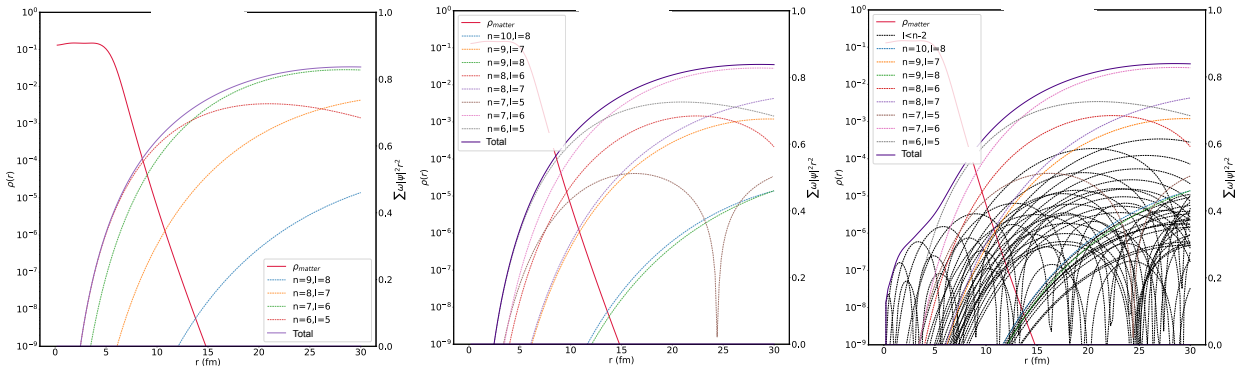

Figure 7.7.: Annihilation probability densities distribution ($\rho \times \rho_{\bar{p}}^{(f)}$) in ^{104}Sn with the SIII Skyrme parametrization. Left: Circular states. Middle: Circular and next-to-circular states. Right: All states.

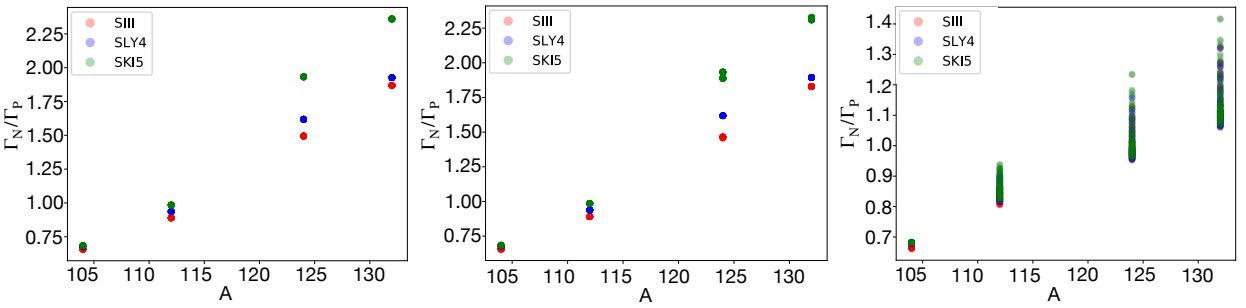

Figure 7.8.: Comparison of three Skyrme parametrizations: SLy4, SKI5 and SIII. Only circular states contributions (left), circular and next-to-circular (middle) and all states (right).

for ^{54}Ca, showing that the proposed method by PUMA is sensitive to small variations of the neutron skin including the expected uncertainties of final states interactions, which are foreseen to be lower than 10%.

As a conclusion, this work has systematically compared X-Ray calculations of Ar, Sn, Ca and Yb with available experimental and numerical data, getting a good control over the cascade code. The benchmarks were used to find proper initial cascade parameters N_0 and α. With these parameters, the calculation of the antiprotonic annihilation states are shown to be independent of N_0 and α and it is observed that 70% of the annihilations occur in circular states.

A first estimation of the sensitivity of PUMA in tin and calcium isotopes is presented. The calculations show that the gamma ratios are sensitive to the isotope mass. A comparison among the Skyrme parameterizations SIII, SLy4 and SKI5 shows that the influence of low angular momentum annihilations is non-negligible. Finally, a study of the neutron skin in tin and calcium isotopes show that the method is sensitive to small diffusiveness variations of 5%-10%.

As an outlook, a full model that allows one to obtain $P(N_0, l)$ should be developed which allows to properly describe the influence of low l levels annihilations. Additionally, the model considering Final State Interactions with the complete estimation of the uncertainties needs to be included (Y. Kubota, S. Wycech, in preparation).

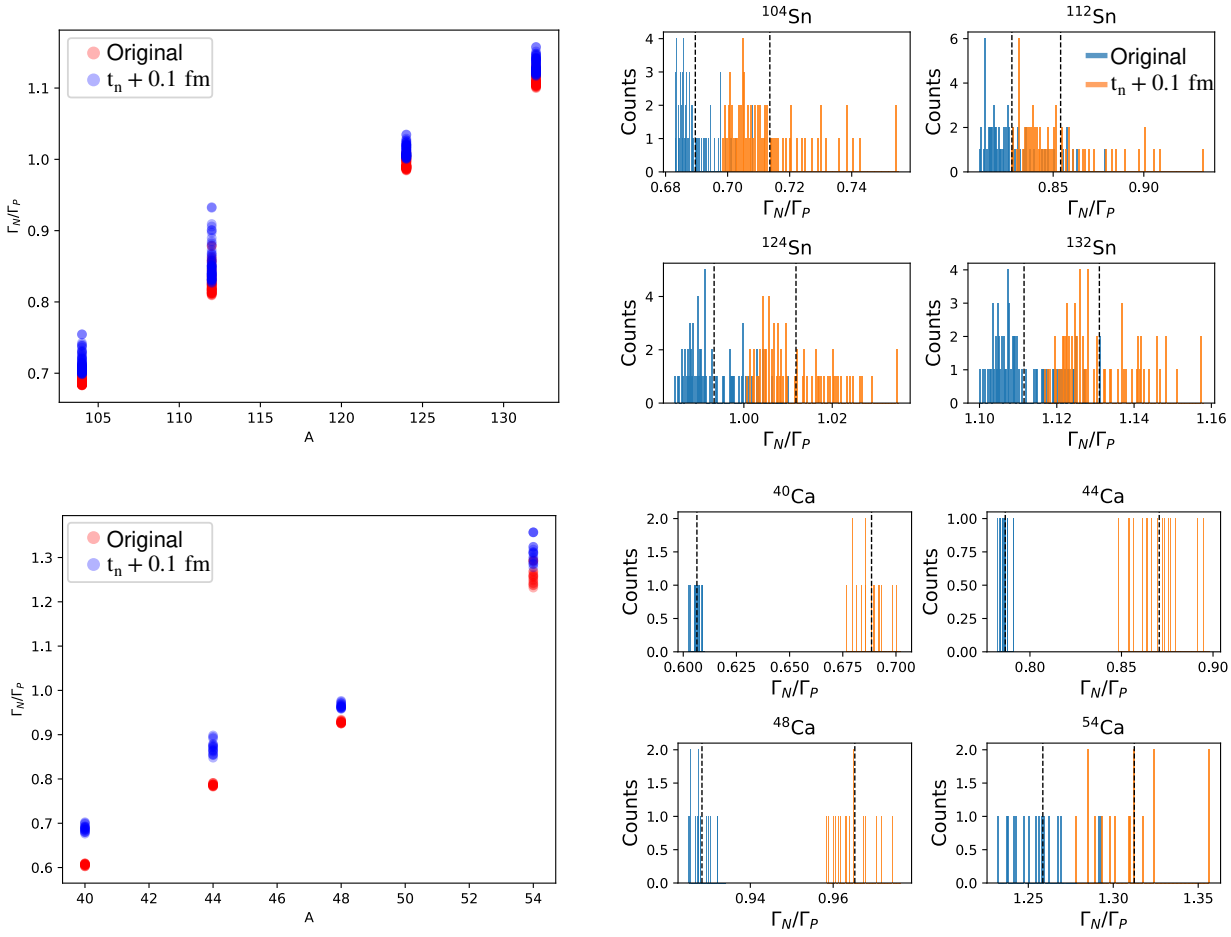

Figure 7.9.: Comparison of the gamma ratios for Sn (top) and Ca (bottom) isotopes with a modified diffusion by 0.1 fm.

Conclusions and Outlook

PUMA is a new experiment at CERN that aims at developing low-energy antiprotons as a tool to probe the isospin structure of the density tail of stable and unstable nuclei. The experiment is currently under construction. The work of this thesis contributes to the core of PUMA: the detection of the annihilation products and the sensitivity of the method.

The simulation, design and development of the Time Projection Chamber (TPC) for the PUMA experiment was performed. Monte-Carlo simulations of realistic events implementing the experimental setup with Geant4 led to the dimensioning of the annular TPC for optimized detection and charge identification of the pions within the 4 T magnet. The simulations also included the drift, amplification and electronic's response expected with low-capacitance, 1 m long cables. As a result of this work, the TPC is chosen to be 300 mm long with an internal, structural radius of 50 mm constrained by the trap, and a sensitive internal radius of 64 mm. The external sensitive radius is 120 mm. This geometry allows for a combined detection and charge identification efficiency of 75%. The overall design of the TPC is tailored to provide a stable operation and long-term reliability within the compact space available inside the magnet's bore of 280 mm diameter, as the detector is hardly accessible once the full setup is assembled. This has an impact on the choices of ionizing gas, drift field, field cage configuration and pad plane design:
An argon based gas mixture for the TPC is chosen due to its low ionization energy and wide availability. Mixtures with Carbon Dioxide and a small percentage of methane have been investigated as they provide an optimal drift field operation at relatively low electric fields of 200-250 V/cm, compared to other widely used mixtures in TPCs.
As the cathode at -6 kV, a few millimetres away from the ground, presents a spark risk and the Finite Element Methods (FEM) softwares Gmsh, ElmerFEM and COMSOL were used to design the field cage in order to minimize discharges and optimize the field uniformity. In this way, a maximum field strength of up to half as the expected breakdown voltage in the critical regions was achieved.
Overall, the anode, cathode and field cage design led to a relative distortion of the electric field close to the shaping electrodes lower than 5% within 0.9 mm away from the field cage strips. Using the Monte-Carlo tracking software Garfield**++**, the drift of the electrons in the TPC was simulated in order to determine electric and magnetic imperfections. The drift volume shows a mean variation of less than 100 μm in 90% of the volume, while less than 200 μm deflection is expected for electrons traversing the full drift length near edges of the TPC.
The background impact and rejection capabilities of PUMA was estimated by introducing the external Geant4 library CRY into the simulation. The realistic cosmic rays showed a rate of two muons per second in the TPC active volume, although 90% do not cross the trap and can be rejected. In this case a rate of only eight particles per minute, which pollute events of multiplicities 1 and 2, are expected.

The PUMA TPC is currently being built and its delivery is planned for end of Sept., 2022. The next steps consist of its validation first with a ^{55}Fe radioactive source and once its correct operation is under control, first measurements with cosmic rays at CERN, where a test bench is deployed, will be performed. The first measurements with antiprotons at ELENA are expected to start taking place during the spring of 2023.

In a second part of the thesis, an existing cascade code was used to estimate the sensitivity of PUMA to the density tails of Sn and Ca isotopes. The code was systematically benchmarked with experimental X-ray yields of ^{124}Sn, ^{48}Ca, ^{40}Ar and ^{176}Yb measured at LEAR, obtaining results also consistent with calculations performed with another cascade code. These benchmarks laid the ground for the choice of meaningful capture parameters: The antiprotonic capture energy level, N_0, and a free parameter, α, that shapes the angular momentum probability distribution, given by $P(l) = (2l + 1)e^{\alpha l}$. Based on these values, the neutron-to- proton annihilation ratios of Sn and Ca isotopes was calculated.
The calculations with the cascade code showed that 70% of the annihilations occur in antiprotonic circular levels, validating the PUMA concept.
Different Skyrme parametrizations were used to describe the densities, and the gamma ratios show a clear dependency with the nuclear mass, as expected. Additionally, a non-negligible contribution from antiprotonic annihilations at low l levels were observed. A small variation of the diffusion coefficient of the densities shows that the gamma ratios are sensitive to small variations of 5%-10%. This study did not include the effect of final state interactions of pions produced at the annihilation with the residual nucleus, which is outside the scope of the present work and which has been studied elsewhere.

An important theoretical next step is the development of a full cascade model, including the decay of the antiproton through the electron cloud. It would also be interesting to integrate the calculation of the absorption widths with custom densities and optical potentials. In this way, other effects such as alpha clustering could be studied and allow for a determination of the experimental sensitivity of PUMA.

To reduce experimentally the uncertainties related to the capture, a coincidence measurement of pions and X rays would be a major upgrade of the PUMA experiment. This would allow to tag pion events together with the annihilation levels, which has never been performed experimentally. A low density or Xenon TPC would be able to detect both. This could be thought of as a future implementation of PUMA, although major modifications in the setup would be required. Indeed, the X-rays would not be able to traverse the penning trap and beamline layers as conceived today.

A. Antiprotonic X-ray transitions

The experimental and calculated values of the X-ray transitions relative intensities, normalized to the transition 12→11 in ^{176}Yb are specified in Tab. A.1 (for the transition Δn_1, Δn_2 and Δn_3) and Tab. A.2 (for the transition Δn_4 and Δn_5).

Table A.1.: Experimental, calculated by Schmidt and calculated in this work X-ray relative intensities (Δn_1, Δn_2 and Δn_3) of ^{176}Yb normalized to the transition n=12→11.

n_i	Δn_1			Δn_2			Δn_3		
	Exp.	Calc.[a]	Calc.[b]	Exp.	Calc.[a]	Calc.[b]	Exp.	Calc.[a]	Calc.[b]
19	42.2±2.2	46.±0.4	46.6	13.7±1.1	12.9±0.1	12.49	5.7±0.6	5.45±0.05	4.3
18	56.1±2.9	57.8±0.5	57.6				5.1±0.5	5.9±0.05	4.7
17	67.7±2.4	66.2±0.6	67.	17.5±0.8	15.6±0.1	13.4	5.8±0.5	5.67±0.05	6.9
16	53.1±2.6	49.2±0.5	48.5	14.3±0.7	11.9±0.1	15.5	6.5±0.5	6.85±0.06	5.6
15	65.8±2.3	67.1±0.6	65.5	13.4±0.6	15.2±0.1	14.7	4.2±0.3	4.7±0.04	5.8
14	96.9±3.	95.3±0.9	93.4	16.8±0.6	15.6±0.1	11.7	4.3±0.4	4.2±0.04	5.4
13	91.9±2.8	94.1±0.9	90.1						
12	100±2.9	100.4±1	100.	15.3±0.7	13.4±0.1	15.7			
11	106.1±3.1	107.7±1	105.7	13.6±0.7	12.4±0.1	12.9			
10	110.2±3.2	116.8±1	114.						
9	28.7±1.1	28.6±0.2	26.						

a: Calculated by Schmidt *et al.*
b: Calculated in this work

The experimental X-ray relative intensities and calculated in this work of ^{124}Sn, normalized with respect to the transition 11→10, is shown in Tab. A.3.

The experimental and calculated values of the X-ray transitions relative intensities, normalized to the transition 7→6 in ^{48}Ca are specified in Tab. A.4

Table A.5 shows the experimental yield of circular transitions in low-pressure ^{40}Ar from Bacher *et. al*.

Table A.2.: Experimental, calculated by Schmidt and calculated in this work X-ray relative intensities (Δn_4 and Δn_5) of ^{176}Yb normalized to the transition n=12→11.

n_i	Δn_4			Δn_5		
	Exp.	Calc.[a]	Calc.[b]	Exp.	Calc.[a]	Calc.[b]
19	3±0.4	2.7±0.02	1.6	1.9±0.5	1.43±0.01	1.3
18				1.6±0.3	1.34±0.01	1.4
17	1.9±0.3	2.42±0.02	1.6			
16	2.1±0.4	1.7±0.01	2.4			
15	2.2±0.5	1.62±0.01	2.7			

a: Calculated by Schmidt *et al.*
b: Calculated in this work

Table A.3.: Experimental and calculated in this work X-ray relative intensities of ^{124}Sn normalized to the transition 11→10.

n_i	Δn_1		Δn_2		Δn_3		Δn_4	
	Exp.	Calc.	Exp.	Calc.	Exp.	Calc.	Exp.	Calc.
19		27.2	6.26±0.7	7.4	3.61±0.33	3.22	1.3±1.	1.01
18		39.6		10.	2.76±0.22	4.15		1.18
17		52.6	11.79±0.8	11.7	4.83±0.3	4.36	2.24±0.15	1.02
16		23.5	6.2±0.9	5.9	3.9±1.	2.39		0.57
15	29.47±6.52	38.5	8.49±0.6	9.6	3.62±0.21	3.6	1.69±0.14	0.69
14	61.55±8.85	53.7	12.4±6.92	12.1	4.68±0.26	4.12	1.18±0.17	0.55
13	72.97±7.26	70.1		13.9		4.04	1.15±0.13	0.28
12	83.95±5.75	86.1	13.42±0.7	14.4	3.16±0.22	3.4		
11	100.±5.61	100.	16.86±1.5	13.5	1.58±1.	2.14		
10	126.26±6.48	110.	11.56±0.77	10.3				
9	110.±5.5	109.9	3.52±0.26	2.53				
8	56.19±2.5	54.9						

Table A.4.: Experimental, calculated by Hartmann and calculated in this work X-ray relative intensities (Δn_1, Δn_2 and Δn_3) of ^{48}Ca normalized to the transition n=7→6

n_i	Δn_1			Δn_2			Δn_3		
	Exp.	Calc.[a]	Calc.[b]	Exp.	Calc.[a]	Calc.[b]	Exp.	Calc.[a]	Calc.[b]
10	38.0$$2.1	41.9±1.6	51.9	13.2±0.7	11.86±0.47	12.4	5.7±0.4	4.67±0.18	4.8
9	66.2±3.4	62.1±2.4	74.	14.1±0.8	15.04±0.60	14.5	5.5±0.5	4.97±0.19	4.2
8	75.1±3.8	84.7±3.3	89.5	16.0±0.9	17.03±0.68	13.4			
7	100.0±5.	103.1±4.	100.	8.9±0.6	10.80±0.43	8.2			
6	85.0±4.3	101.±4.	90.4						

a : Calculated by Hartmann *et al.*

b : Calculated in this work

Table A.5.: Experimental yield of circular transitions in low-pressure ^{40}Ar from Bacher *et. al*.

n_i	Experimental Absolute yield
22	0.27±0.124
21	0.44±0.107
20	0.328±0.107
19	0.523±0.104
18	0.68±0.13
17	0.21±0.061
16	0.132±0.033
15	0.511±0.089
14	0.588±0.100
13	0.624±0.104
12	0.595±0.099
11	0.593±0.098
10	0.605±0.100

B. Academic CV

Removed in this published version.

References

[1] E. Rutherford. “The scattering of α and β particles by matter and the structure of the atom”. In: *Philosophical Magazine* 92.4 (1911).

[2] E. Rutherford. “Collision of α particles with light atoms. IV. An anomalous effect in nitrogen”. In: *Philosophical Magazine* 90.S1 (1919).

[3] J. Chadwick. “The existence of a neutron”. In: *Proc. of the Royal Society of London A* 136.830 (1932).

[4] R. Hofstadter. “Electron Scattering and Nuclear Structure”. In: *Rev. Mod. Phys.* 28 (1956).

[5] B. Frois et al. “High-Momentum-Transfer Electron Scattering from $^{208}\mathrm{Pb}$”. In: *Phys. Rev. Lett.* 38 (1977).

[6] B. Frois. In: *Proceedings of the International Conference on Nuclear Physics* (Florence, Italy). Ed. by P. Blasi and R. Ricci. Tipografia Bologna, (1980).

[7] M.H. Johnson and E. Teller. “Proton Distribution in Heavy Nuclei”. In: *Phys. Rev.* 93.2 (1954).

[8] IAEA. *Live Chart of Nuclides*. `https://www-nds.iaea.org`. Accessed: 2022-07-08.

[9] I. Tanihata et al. “Measurements of interaction cross sections and nuclear radii in the light p-shell region”. In: *Phys. Rev. Lett.* 55.24 (1985).

[10] P.G. Hansen and Björn Jonson. “The neutron halo of extremely neutron-rich nuclei”. In: *EPL* 4.4 (1987).

[11] I. Tanihata. “Neutron halo nuclei”. In: *J Phys G Nucl Part Phys.* 22.2 (1996).

[12] T. Kobayashi et al. “Projectile Fragmentation of the Extremely Neutron-Rich Nucleus $^{11}\mathrm{Li}$ at 0.79 GeV/nucleon”. In: *Phys. Rev. Lett.* 60 (1988).

[13] D. J. Morrissey and B. M. Sherrill. “Radioactive nuclear beam facilities based on projectile fragmentation”. In: *Phil. Trans. R. Soc. A* 356.1744 (1998).

[14] A.V. Dobrovolsky et al. “Study of the nuclear matter distribution in neutron-rich Li isotopes”. In: *Nucl. Phys. A* 766 (2006).

[15] P. Egelhof et al. “Nuclear-matter distributions of halo nuclei from elastic proton scattering in inverse kinematics”. In: *Exotic Nuclei and Atomic Masses*. Springer, 2003.

[16] T. Nakamura et al. “Deformation-Driven p-Wave Halos at the Drip Line: $^{31}\mathrm{Ne}$”. In: *Phys. Rev. Lett.* 112 (14 2014).

[17] N. Kobayashi et al. “Observation of a p-Wave One-Neutron Halo Configuration in $^{37}\mathrm{Mg}$”. In: *Phys. Rev. Lett.* 112 (24 2014).

[18] M.V. Zhukov and I.J. Thompson. “Existence of proton halos near the drip line”. In: *Phys. Rev. C* 52.6 (1995).

[19] E. Ryberg et al. “Effective field theory for proton halo nuclei”. In: *Phys. Rev. C* 89.1 (2014).

[20] R. Kanungo et al. “Possibility of a two-proton halo in 17Ne”. In: *Phys. Lett. B* 571.1-2 (2003).

[21] T. Minamisono et al. “Proton halo of $^{8}\mathrm{B}$ disclosed by its giant quadrupole moment”. In: *Phys. Rev. Lett.* 69 (1992).

[22] G.A. Korolev et al. “Halo structure of 8B determined from intermediate energy proton elastic scattering in inverse kinematics”. In: *Phys. Lett. B* 780 (2018).

[23] A. S. Demyanova et al. “Proton halo in the 13N nucleus”. In: *JETP Letters* 104.8 (2016).

[24] K. Rituparna. “Two-proton halo in 17Ne”. In: *Nucl. Phys. A* 738 (2004). Proceedings of the 8th International Conference on Clustering Aspects of Nuclear Structure and Dynamics.

[25] W. Geithner et al. “Masses and Charge Radii of $^{17-22}\mathrm{Ne}$ and the Two-Proton-Halo Candidate $^{17}\mathrm{Ne}$”. In: *Phys. Rev. Lett.* 101 (2008).

[26] C. Lehr et al. “Unveiling the two-proton halo character of 17Ne: Exclusive measurement of quasi-free proton-knockout reactions”. In: *Phys. Lett. B* 827 (2022).

[27] G. Hagen, T. Papenbrock, and M. Hjorth-Jensen. “Ab Initio Computation of the $^{17}\mathbf{F}$ Proton Halo State and Resonances in $A = 17$ Nuclei”. In: *Phys. Rev. Lett.* 104 (2010).

[28] T. Aumann et al. “PUMA, antiProton unstable matter annihilation - PUMA collaboration”. In: *Eur. Phys. J. A* 58.5 (2022).

[29] T. Aumann and T. Nakamura. “The electric dipole response of exotic nuclei”. In: *Physica Scripta* 2013.T152 (2013).

[30] A. Obertelli and H. Sagawa. *Modern nuclear physics, from fundamentals to frontiers*. Springer, (2021). ISBN: 978-981-16-2288-5.

[31] P. Sarriguren et al. “Nuclear skin emergence in Skyrme deformed Hartree-Fock calculations”. In: *Phys. Rev. C* 76.4 (2007).

[32] N. Fukunishi, T. Otsuka, and I. Tanihata. “Neutron-skin and proton-skin formations in exotic nuclei far from stability”. In: *Phys. Rev. C* 48.4 (1993).

[33] M. Warda et al. “Analysis of bulk and surface contributions in the neutron skin of nuclei”. In: *Phys. Rev. C* 81.5 (2010).

[34] J. Dobaczewski, W Nazarewicz, and TR Werner. “Neutron radii and skins in the Hartree-Fock-Bogoliubov calculations”. In: *Zeitschrift für Physik A Hadrons and Nuclei* 354.1 (1996).

[35] A.D. Martin. “A study of K–mesic atoms”. In: *Il Nuovo Cimento (1955-1965)* 27.6 (1963).

[36] M. Thiel et al. “Neutron skins of atomic nuclei: per aspera ad astra”. In: *J Phys G Nucl Part Phys.* 46.9 (2019).

[37] D. Adhikari et al. “Accurate Determination of the Neutron Skin Thickness of $^{208}\mathrm{Pb}$ through Parity-Violation in Electron Scattering”. In: *Phys. Rev. Lett.* 126 (2021).

[38] V.E. Starodubsky and N.M. Hintz. “Extraction of neutron densities from elastic proton scattering by ^{206,207,208}Pb at 650 MeV”. In: *Phys. Rev. C* 49.4 (1994).

[39] J. Zenihiro et al. “Neutron density distributions of ^{204,206,208}Pb deduced via proton elastic scattering at E_p= 295 MeV”. In: *Phys. Rev. C* 82.4 (2010).

[40] B. Tatischeff, I. Brissaud, and L. Bimbot. “Neutron Radius of ^{208}Pb from 166-MeV Alpha-Particle Scattering”. In: *Phys. Rev. C* 5.1 (1972).

[41] G. Dugan et al. “Elastic scattering of low-energy pions and muons from lead”. In: *Phys. Rev. C* 8.3 (1973).

[42] C.M. Tarbert et al. “Neutron skin of ^{208}Pb from coherent pion photoproduction”. In: *Phys. Rev. Lett.* 112.24 (2014).

[43] T. Aumann et al. “Peeling off neutron skins from neutron-rich nuclei: Constraints on the symmetry energy from neutron-removal cross sections”. In: *Phys. Rev. Lett.* 119.26 (2017).

[44] A. Gardestig, C. J. Horowitz, and Gerald A. Miller. *Comment on "Neutron Skin of ^{208}Pb from Coherent Pion Photoproduction"*. 2015. DOI: 10.48550/ARXIV.1504.08347.

[45] J. Piekarewicz and S.P. Weppner. “Insensitivity of the elastic proton–nucleus reaction to the neutron radius of ^{208}Pb”. In: *Nucl. Phys. A* 778.1-2 (2006).

[46] C.R. Chinn, C. Elster, and R.M. Thaler. “Isospin effects in elastic proton-nucleus scattering”. In: *Phys. Rev. C* 47.5 (1993).

[47] L. Ray and G.W. Hoffmann. “Relativistic and nonrelativistic impulse approximation descriptions of 300–1000 MeV proton+ nucleus elastic scattering”. In: *Phys. Rev. C* 31.2 (1985).

[48] C. A. Bertulani and J. Valencia. “Neutron skins as laboratory constraints on properties of neutron stars and on what we can learn from heavy ion fragmentation reactions”. In: *Phys. Rev. C* 100 (2019).

[49] C.J. Horowitz et al. “A way forward in the study of the symmetry energy: experiment, theory, and observation”. In: *J Phys G Nucl Part Phys.* 41.9 (2014).

[50] C.J. Horowitz and J. Piekarewicz. “Neutron star structure and the neutron radius of ^{208}Pb”. In: *Phys. Rev. Lett.* 86.25 (2001).

[51] M.C. Miller et al. “PSR J0030+ 0451 mass and radius from NICER data and implications for the properties of neutron star matter”. In: *The Astrophysical Journal Letters* 887.1 (2019).

[52] K. C. Gendreau, Z. Arzoumanian, and T. Okajima. “The Neutron star Interior Composition ExploreR (NICER): an Explorer mission of opportunity for soft x-ray timing spectroscopy”. In: *Space Telescopes and Instrumentation 2012: Ultraviolet to Gamma Ray*. Vol. 8443. SPIE. 2012.

[53] Ö. Feryal. “Surface emission from neutron stars and implications for the physics of their interiors”. In: *Reports on Progress in Physics* 76.1 (2012).

[54] B. A. Brown. “Neutron radii in nuclei and the neutron equation of state”. In: *Phys. Rev. Lett.* 85.25 (2000).

[55] J. M. Lattimer and M. Prakash. “Nuclear matter and its role in supernovae, neutron stars and compact object binary mergers”. In: *Physics Reports* 333 (2000).

[56] X. Roca-Maza et al. “Neutron skin of Pb 208, nuclear symmetry energy, and the parity radius experiment”. In: *Phys. Rev. Lett.* 106.25 (2011).

[57] M. Beyer et al. “Light clusters in nuclear matter of finite temperature”. In: *Eur. Phys. J. A-Hadrons and Nuclei* 22.2 (2004).

[58] C.J. Horowitz and A. Schwenk. “Cluster formation and the virial equation of state of low-density nuclear matter”. In: *Nucl. Phys. A* 776.1-2 (2006).

[59] M. Beyer et al. “The α-particle in nuclear matter”. In: *Phys. Lett. B* 488.3-4 (2000).

[60] S. Typel et al. “Composition and thermodynamics of nuclear matter with light clusters”. In: *Phys. Rev. C* 81.1 (2010).

[61] J. Tanaka et al. “Formation of α clusters in dilute neutron-rich matter”. In: *Science* 371.6526 (2021).

[62] C. J. Batty, E. Friedman, and A. Gal. “Strong interaction physics from hadronic atoms”. In: *Physics reports* 287.5 (1997).

[63] D. Gotta. “Precision spectroscopy of light exotic atoms”. In: *Prog. Part. Nucl.* 52.1 (2004).

[64] R. Schmidt et al. “Nucleon density of 172 Yb and 176 Yb at the nuclear periphery determined with antiprotonic x rays”. In: *Phys. Rev. C* 58.6 (1998).

[65] S. Wycech et al. “Antiprotonic studies of nuclear neutron halos”. In: *Phys. Rev. C* 54.4 (1996).

[66] S.J. Orfanidis and V. Rittenberg. “Nucleon-antinucleon annihilation into pions”. In: *Nucl. Phys. B* 59.2 (1973).

[67] C. Ghesquiere. “An inclusive view on $p\bar{p} \to n\pi$ at rest”. In: *Symposium on Antinucleon-Nucleon Interactions, CERN* (1974).

[68] E. Klempt, C. Batty, and .M. Richard J. “The antinucleon–nucleon interaction at low energy: Annihilation dynamics”. In: *Physics Reports* 413.4-5 (2005).

[69] A.S. Iljinov, V.I. Nazaruk, and S.E. Chigrinov. “Nuclear absorption of stopped antiprotons: Multipion-nucleus interactions”. In: *Nucl. Phys. A* 382.3 (1982).

[70] M.R. Clover et al. “Low energy antiproton-nucleus interactions”. In: *Phys. Rev. C* 26.5 (1982).

[71] W.M. Bugg et al. “Evidence for a neutron halo in heavy nuclei from antiproton absorption”. In: *Phys. Rev. Lett.* 31.7 (1973).

[72] M. Wade and V.G. Lind. “Ratio of antiproton annihilations on neutrons and protons in carbon for low-energy and stopped antiprotons”. In: *Phys. Rev. D* 14.5 (1976).

[73] J. Jastrzębski et al. “Signature of a neutron halo in ^{232}Th from antiproton absorption”. In: *Nucl. Phys. A* 558 (1993).

[74] P. Lubiński et al. “Composition of the nuclear periphery from antiproton absorption”. In: *Phys. Rev. C* 57.6 (1998).

[75] J. Cugnon et al. “Geometrical effects in antiproton annihilation on nuclei”. In: *Phys. Rev. C* 63.2 (2001).

[76] A.C. Mueller. “An overview of radioactive beam facilities”. In: *Proceedings of EPAC 2000*. (2000).

[77] S.A. Baird et al. *Design study of the antiproton decelerator: AD*. Tech. rep. 1996.

[78] W Oelert. “The ELENA project at CERN”. In: *arXiv preprint arXiv:1501.05728* (2015).

[79] R. Catherall et al. “The ISOLDE facility”. In: *J Phys G Nucl Part Phys.* 44.9 (2017).

[80] L. S. Brown and G. Gabrielse. “Geonium theory: Physics of a single electron or ion in a Penning trap”. In: *Reviews of Modern Physics* 58.1 (1986).

[81] C.H. Tseng and G. Gabrielse. “Portable trap carries particles 5000 kilometers”. In: *Hyperfine Interactions* 76.1 (1993).

[82] C. Smorra et al. “BASE–the baryon antibaryon symmetry experiment”. In: *Eur. Phys. J.: Spec.* 224.16 (2015).

[83] S. Sellner et al. “Improved limit on the directly measured antiproton lifetime”. In: *New Journal of Physics* 19.8 (2017).

[84] G. Gabrielse et al. “Stacking of cold antiprotons”. In: *Phys. Lett. B* 548.3-4 (2002).

[85] G. Gabrielse et al. “Trapped antihydrogen in its ground state”. In: *Phys. Rev. Lett.* 108.11 (2012).

[86] G. Gabrielse et al. “Antihydrogen production using trapped plasmas”. In: *Physics Letters A* 129.1 (1988).

[87] G.B. Andresen et al. “Trapped antihydrogen”. In: *Nature* 468.7324 (2010), pp. 673–676.

[88] ALPHA Collaboration. http://alpha.web.cern.ch.

[89] AEgIS Collaboration. https://aegis.web.cern.ch/aegis.

[90] J. N. Marx and D. R. Nygren. “The Time Projection Chamber”. In: *Physics Today* 31.10 (1978).

[91] H. Bethe and J. Ashkin. “The Time Projection Chamber”. In: *Physics Today* 31.10 (1978).

[92] R. L. Workman et al. “Review of Particle Physics”. In: *PTEP* 2022 (2022).

[93] D. I. Thwaites. “Bragg’s Rule of Stopping Power Additivity: A Compilation and Summary of Results”. In: *Radiation Research* 95.3 (1983).

[94] I. B. Smirnov. “Modeling of ionization produced by fast charged particles in gases”. In: *Nucl. Instrum. Meth. Res. Sect. A: Accel., Spectr., Detect. Assoc. Equip* 554.1-3 ().

[95] W.R. Leo. *Techniques for Nuclear and Particle Physics Experiments: A How-to Approach*. 1st ed. ISBN 978-3-642-57920-2. Springer-Verlag., (1987).

[96] J. Alme et al. “The ALICE TPC, a large 3-dimensional tracking device with fast readout for ultra-high multiplicity events”. In: *Nucl. Instrum. Meth. Res. Sect. A: Accel., Spectr., Detect. Assoc. Equip* 622.1 (2010).

[97] Y. Ayyad et al. “Next-generation experiments with the Active Target Time Projection Chamber (AT-TPC)”. In: *Nucl. Instrum. Meth. Res. Sect. A: Accel., Spectr., Detect. Assoc. Equip* 954 (2020). Symposium on Radiation Measurements and Applications XVII.

[98] P. Baron et al. “Large bulk-micromegas detectors for TPC applications in HEP”. In: *2007 IEEE Nuclear Science Symposium Conference Record*. Vol. 6. (2007).

[99] D. Bazin et al. “Low energy nuclear physics with active targets and time projection chambers”. In: *Prog. Part. Nucl.* 114, 103790 (2020).

[100] A. Obertelli et al. “MINOS: A vertex tracker coupled to a thick liquid-hydrogen target for in-beam spectroscopy of exotic nuclei”. In: *Eur. Phys. J. A* 50.1 (2014).

[101] K.T. Leung and C.E. Brion. “Experimental investigation of the valence orbital momentum distributions and ionization energies of the noble gases by binary (e, 2e) spectroscopy”. In: *Chemical physics* 82.1-2 (1983).

[102] J.E. Parks et al. “Ionization of the noble gases by protons: Jesse effects as a function of pressure”. In: *The Journal of Chemical Physics* 57.12 (1972).

[103] F. Sauli. *Gaseous Radiation Detectors: Fundamentals and Applications*. Vol. 36. Cambridge University Press, (2014). ISBN: 978-1-107-04301-5, 978-1-139-99044-8.

[104] M. Anderson et al. “The STAR time projection chamber: a unique tool for studying high multiplicity events at RHIC”. In: *Nucl. Instrum. Meth. Res. Sect. A: Accel., Spectr., Detect. Assoc. Equip* 499.2 (2003).

[105] A. Einstein. “Über einen die Erzeugung und Verwandlung des Lichtes betreffenden heuristischen Gesichtspunkt”. In: *Annales der Physik* 322.6 (1905).

[106] A. Einstein. “Über die von der molekularkinetischen Theorie der Wärme geforderte Bewegung von in ruhenden Flüssigkeiten suspendierten Teilchen”. In: *Annales der Physik* 322.8 (1905).

[107] A. Einstein. “Zur Elektrodynamik bewegter Körper”. In: *Annales der Physik* 322.10 (1905).

[108] A. Einstein. “Ist die Trägheit eines Körpers von seinem Energieinhalt abhängig?” In: *Annales der Physik* 323.13 (1905).

[109] R F.R.S. Hon. M.R.S.E. & R.I. Acad. V.P.L.S. Brown. “XXVII. A brief account of microscopical observations made in the months of June, July and August 1827, on the particles contained in the pollen of plants; and on the general existence of active molecules in organic and inorganic bodies”. In: *The Philosophical Magazine* 4.21 (1828).

[110] C. Ramsauer. “Über den Wirkungsquerschnitt der Gasmoleküle gegenüber langsamen Elektronen”. In: *Annalen der Physik* 369.6 (1921).

[111] S.R. Amendolia et al. “Dependence of the transverse diffusion of drifting electrons on magnetic field”. In: *Nucl. Instrum. Meth. Res. Sect. A: Accel., Spectr., Detect. Assoc. Equip* 244.3 (1986).

[112] H. Spieler. *Lecture notes in Radiation Detectors and Signal Processing*. 2001.

[113] D. Rapp and P. Englander-Golden. “Total Cross Sections for Ionization and Attachment in Gases by Electron Impact. I. Positive Ionization”. In: *The Journal of Chemical Physics* 43.5 (1965).

[114] J.S. Townsend. *The Theory Of Ionization Of Gases By Collision*. 1st ed. ISBN 116388510X. Constable and Co., Ltd., (1910).

[115] H. Raether. *Electron avalanches and breakdown in gases*. Butterworths, (1964).

[116] A. Tripathy et al. “Measurement of ion backflow fraction in GEM detectors”. In: *Nucl. Instrum. Meth. Res. Sect. A: Accel., Spectr., Detect. Assoc. Equip* 1013 (2021).

[117] M. Ball, K. Eckstein, and T. Gunji. “Ion backflow studies for the ALICE TPC upgrade with GEMs”. In: *Journal of Instrumentation* 9.04 (2014).

[118] S. Wang et al. “Studies on ion back-flow of Time Projection Chamber based on GEM and anode wire grid”. In: *Nucl. Instrum. Meth. Res. Sect. A: Accel., Spectr., Detect. Assoc. Equip* 940 (2019).

[119] F. Sauli. “GEM: A new concept for electron amplification in gas detectors”. In: *Nucl. Instrum. Meth. Res. Sect. A: Accel., Spectr., Detect. Assoc. Equip* 386.2 (1997).

[120] Y. Giomataris et al. “MICROMEGAS: a high-granularity position-sensitive gaseous detector for high particle-flux environments”. In: *Nucl. Instrum. Meth. Res. Sect. A: Accel., Spectr., Detect. Assoc. Equip* 376.1 (1996).

[121] F. Sauli. “The gas electron multiplier (GEM): Operating principles and applications”. In: *Nucl. Instrum. Meth. Res. Sect. A: Accel., Spectr., Detect. Assoc. Equip* 805 (2016).

[122] A. Bondar et al. “Light multi-GEM detector for high-resolution tracking systems”. In: *Nucl. Instrum. Meth. Res. Sect. A: Accel., Spectr., Detect. Assoc. Equip* 556.2 (2006).

[123] P. Thuiner et al. “Multi-GEM detectors in high particle fluxes”. In: *EPJ Web of Conferences*. Vol. 174. EDP Sciences. (2018).

[124] S. Bachmann et al. “Discharge studies and prevention in the gas electron multiplier (GEM)”. In: *Nucl. Instrum. Meth. Res. Sect. A: Accel., Spectr., Detect. Assoc. Equip* 479.2-3 (2002).

[125] P. Colas, I. Giomataris, and V. Lepeltier. “Ion backflow in the Micromegas TPC for the future linear collider”. In: *Nucl. Instrum. Meth. Res. Sect. A: Accel., Spectr., Detect. Assoc. Equip* 535.1-2 (2004).

[126] P. Bhattacharya et al. “Investigation of ion backflow in bulk micromegas detectors”. In: *Journal of Instrumentation* 10.09 (2015).

[127] A. Bay et al. “Study of sparking in Micromegas chambers”. In: *Nucl. Instrum. Meth. Res. Sect. A: Accel., Spectr., Detect. Assoc. Equip* 488.1-2 (2002).

[128] I. Giomataris et al. “Micromegas in a bulk”. In: *Nucl. Instrum. Meth. Res. Sect. A: Accel., Spectr., Detect. Assoc. Equip* 560.2 (2006), pp. 405–408.

[129] M.S. Dixit et al. “Position sensing from charge dispersion in micro-pattern gas detectors with a resistive anode”. In: *Nucl. Instrum. Meth. Res. Sect. A: Accel., Spectr., Detect. Assoc. Equip* 518.3 (2004).

[130] M.S. Dixit and A. Rankin. “Simulating the charge dispersion phenomena in Micro Pattern Gas Detectors with a resistive anode”. In: *Nucl. Instrum. Meth. Res. Sect. A: Accel., Spectr., Detect. Assoc. Equip* 566.2 (2006).

[131] D. Attié et al. “Characterization of resistive Micromegas detectors for the upgrade of the T2K Near Detector Time Projection Chambers”. In: *Nucl. Instrum. Meth. Res. Sect. A: Accel., Spectr., Detect. Assoc. Equip* 1025 (2022).

[132] K. Gnanvo. *Advanced Micro-Pattern Gas Detectors for Tracking at the Electron Ion Collider*. Letter of intent. 2020.

[133] S. Ramo. “Currents Induced by Electron Motion”. In: *Proceedings of the IRE* 27.9 (1939).

[134] H. Spieler. *Semiconductor Detector Systems*. 1st ed. ISBN 0–19–852784–5. Oxford University Press., (2005).

[135] S. Anvar et al. “AGET, the GET front-end ASIC, for the readout of the Time Projection Chambers used in nuclear physic experiments”. In: *2011 IEEE Nuclear Science Symposium Conference Record*. IEEE. (2011).

[136] S. et al. Agostinelli. “Geant4 - A simulation toolkit”. In: *Nucl. Instrum. Meth.* 506.3 (2003).

[137] R. Brun and F. Rademakers. “ROOT - An Object Oriented Data Analysis Framework”. In: *Proceedings AIHENP’96 Workshop, Lausanne, Sep. 1996, Nucl. Inst. & Meth. in Phys. Res. A* 389 (1997).

[138] C. Santamaria et al. “Tracking with the MINOS Time Projection Chamber”. In: *Nucl. Instrum. Meth. Res. Sect. A: Accel., Spectr., Detect. Assoc. Equip* 905 (2018).

[139] S.F. Biagi. “Monte Carlo simulation of electron drift and diffusion in counting gases under the influence of electric and magnetic fields”. In: *Nucl. Instrum. Meth. Res. Sect. A: Accel., Spectr., Detect. Assoc. Equip.* 421.1 (1999).

[140] T. Zerguerras et al. “Understanding avalanches in a Micromegas from single-electron response measurement”. In: *Nucl. Instrum. Meth. Res. Sect. A: Accel., Spectr., Detect. Assoc. Equip* 772 (2015).

[141] F. James and M. Winkler. “MINUIT User’s Guide”. In: *INSPIRE* (2004).

[142] N. Abgrall et al. “Time projection chambers for the T2K near detectors”. In: *Nucl. Instrum. Meth. Res. Sect. A: Accel., Spectr., Detect. Assoc. Equip* 637.1 (2011).

[143] F. Sauli, L. Ropelewski, and P. Everaerts. “Ion feedback suppression in time projection chambers”. In: *Nucl. Instrum. Meth. Res. Sect. A: Accel., Spectr., Detect. Assoc. Equip* 560.2 (2006).

[144] C. Hagmann et al. “Cosmic-ray shower library (CRY)”. In: *Lawrence Livermore National Laboratory document UCRL-TM-229453* (2012).

[145] C. Hagmann, David Lange, and Douglas Wright. “Cosmic-ray shower generator (CRY) for Monte Carlo transport codes”. In: *2007 IEEE Nuclear Science Symposium Conference Record*. Vol. 2. (2007).

[146] C. Geuzaine and J.F. Remacle. “Gmsh: A 3-D finite element mesh generator with built-in pre- and post-processing facilities”. In: *International journal for numerical methods in engineering* 79.11 (2009).

[147] M. Malinen and P. Råback. “Elmer finite element solver for multiphysics and multiscale problems”. In: *Multiscale Model. Methods Appl. Mater. Sci.* 19 (2013).

[148] N. Gokhale. *Practical Finite Element Analysis*. Finite to infinity, (2008).

[149] Cecil G Armstrong. “Modelling requirements for finite-element analysis”. In: *Computer-aided design* 26.7 (1994), pp. 573–578.

[150] C. Stimpson et al. “The verdict library reference manual”. In: *Sandia National Laboratories Technical Report* 9.6 (2007).

[151] R. Veenhof and H. Schindler. https://garfieldpp.web.cern.ch/garfieldpp/.

[152] S.F. Biagi. “Monte Carlo simulation of electron drift and diffusion in counting gases under the influence of electric and magnetic fields”. In: *Nucl. Instrum. Meth. Res. Sect. A: Accel., Spectr., Detect. Assoc. Equip* 421.1-2 (1999).

[153] F. Paschen. *Ueber die zum funkenübergang in luft: wasserstoff und kohlensäure bei verschiedenen drucken erforderliche potentialdifferenz*. JA Barth, (1889).

[154] D.C. Faircloth. “Technological aspects: High voltage”. In: *arXiv preprint arXiv:1404.0952* (2014).

[155] N. Van Schaik and T. Czaszejko. “Conditions of discharge-free operation of XLPE insulated power cable systems”. In: *IEEE Transactions on Dielectrics and Electrical Insulation* 15.4 (2008).

[156] R. Tarzwell and K. Bahl. “High voltage printed circuit design and manufacturing notebook”. In: *Sierra Proto Express* (2004).

[157] *RD51 collaboration group*. https://rd51-public.web.cern.ch/.

[158] P. Baron and E. Delagnes. “STAGE, a Front End ASIC for Active Time Projection Chamber Data Sheet”. In: *Irfu/CEA Saclay* (2019).

[159] Y.-C. Cheng et al. “Desmearing of FR4 Epoxy Resin Using NMP-Based Sweller”. In: *Journal of electronic materials* 38.11 (2009), pp. 2368–2375.

[160] FPGA solutions Enclustra. *Mercury ZX1 SoC module user manual*. 2018.

[161] S. Tomonaga and G. Araki. “Effect of the nuclear Coulomb field on the capture of slow mesons”. In: *Phys. Rev.* 58.1 (1940).

[162] E. Fermi and E. Teller. “The capture of negative mesotrons in matter”. In: *Phys. Rev.* 72.5 (1947).

[163] W.F. Fry. “The capture and decay of mesons in photographic emulsions”. In: *Phys. Rev.* 83.3 (1951).

[164] V. L. Fitch and J. Rainwater. “Studies of X-rays from Mu-mesonic atoms”. In: *Phys. Rev.* 92.3 (1953).

[165] G. R. Burleson et al. “Observation of K-Mesonic X Rays in Helium”. In: *Phys. Rev. Lett.* 15.2 (1965).

[166] M. Camac et al. “X-rays from mesic atoms”. In: *Phys. Rev.* 88.1 (1952).

[167] A. Bamberger et al. “Observation of antiprotonic atoms”. In: *Phys. Lett. B* 33.3 (1970).

[168] G. Backenstoss et al. “Observations of Σ hyperonic atoms”. In: *Phys. Lett. B* 33.3 (1970).

[169] R. Pohl et al. “The size of the proton”. In: *nature* 466.7303 (2010).

[170] D. Castelvecchi. “Proton-size puzzle deepens”. In: *Nature* (2017).

[171] A. Beyer et al. “The Rydberg constant and proton size from atomic hydrogen”. In: *Science* 358.6359 (2017).

[172] N. Bezginov et al. “A measurement of the atomic hydrogen Lamb shift and the proton charge radius”. In: *Science* 365.6457 (2019).

[173] S. K. Barcus, Douglas W Higinbotham, and Randall E McClellan. “How analytic choices can affect the extraction of electromagnetic form factors from elastic electron scattering cross section data”. In: *Phys. Rev. C* 102.1 (2020).

[174] J.M. Alarcón et al. “Proton charge radius extraction from electron scattering data using dispersively improved chiral effective field theory”. In: *Phys. Rev. C* 99.4 (2019).

[175] F. Napolitano et al. “Kaonic Atoms at the DAΦNE Collider with the SIDDHARTA-2 Experiment”. In: *arXiv preprint arXiv:2201.11525* (2022).

[176] T. Kishimoto. “Kaonic nuclei excited by the (K^-, N) reaction”. In: *Phys. Rev. Lett.* 83.23 (1999).

[177] C. Curceanu et al. “The modern era of light kaonic atom experiments”. In: *Reviews of Modern Physics* 91.2 (2019).

[178] M. Trassinelli et al. “Measurement of the charged pion mass using X-ray spectroscopy of exotic atoms”. In: *Phys. Lett. B* 759 (2016).

[179] T. Walcher. “Experiments at the low-energy antiproton ring (LEAR)”. In: *Annu. Rev. Nucl. Sci.;(United States)* 38.1 (1988).

[180] S. Alighanbari et al. “Precise test of quantum electrodynamics and determination of fundamental constants with HD+ ions”. In: *Nature* 581.7807 (2020).

[181] A. Sótér et al. “High-resolution laser resonances of antiprotonic helium in superfluid 4He”. In: *Nature* 603.7901 (2022).

[182] T. Suzuki, D. F. Measday, and JP Roalsvig. “Total nuclear capture rates for negative muons”. In: *Phys. Rev. C* 35.6 (1987).

[183] M. Leon and R. Seki. “Determination of the neutron halo from antiproton absorption”. In: *Phys. Lett. B* 48.3 (1974).

[184] M. Leon and R. Seki. “Atomic capture of negative mesons”. In: *Phys. Rev. Lett.* 32.4 (1974).

[185] P. Vogel et al. “Muon capture in atoms, crystals and molecules”. In: *Nucl. Phys. A* 254.2 (1975).

[186] M. Leon and R. Seki. “Atomic capture of negative mesons:(I). The Fermi-Teller model”. In: *Nucl. Phys. A* 282.3 (1977).

[187] H. Daniel. “Theory of the Coulomb capture of negative mesonic particles”. In: *Annals of Physics* 129.2 (1980).

[188] H. Daniel. “Dependence of Coulomb capture ratio and x-ray intensities on the mesonic-particle energy spectrum”. In: *Zeitschrift für Physik A Atoms and Nuclei* 302.3 (1981).

[189] H. Daniel. “Coulomb capture of muons and atomic radius”. In: *Zeitschrift für Physik A Atoms and Nuclei* 291.1 (1979).

[190] M.Y. Au-Yang and M.L. Cohen. “Meson Captures in Solids”. In: *Phys. Rev.* 174.2 (1968).

[191] G. A. Baker Jr. “Stopping of π-Minus and K-Minus Mesons on Hydrogen in Nuclear Emulsion”. In: *Phys. Rev.* 117.4 (1960).

[192] F. J. Hartmann et al. “Measurement of the muonic x-ray cascade in Mg, AI, In, Ho, and Au”. In: *Zeitschrift für Physik A Atoms and Nuclei* 305.3 (1982).

[193] Y. Eisenberg and D. Kessler. “On the μ- mesonic atoms”. In: *Il Nuovo Cimento (1955-1965)* 19.6 (1961).

[194] F. J. Hartmann et al. “Measurement of the muonic X-ray cascade in metallic iron”. In: *Phys. Rev. Lett.* 37.6 (1976).

[195] D. Kessler et al. “μ-Atomic Lyman and Balmer Series in Ti, TiO_2. and Mn”. In: *Phys. Rev. Lett.* 18.26 (1967).

[196] K. K. Seung. “Z-Dependent initial population of muon orbital angular momentum states”. In: *Journal of the Korean Physical Society* 20.4 (1987).

[197] J. S. Cohen. “Capture of negative exotic particles by atoms, ions and molecules”. In: *Reports on Progress in Physics* 67.10 (2004).

[198] D. Hartmann F.J. Horváth, Leopold M. Simons, and G. Torelli. *Electromagnetic cascade and chemistry of exotic atoms*. Vol. 52. Springer Science & Business Media, 1990.

[199] M. Leon and H.A. Bethe. “Negative meson absorption in liquid hydrogen”. In: *Physical Review* 127.2 (1962).

[200] E. Borie and M. Leon. “X-ray yields in protonium and mesic hydrogen”. In: *Physical Review A* 21.5 (1980).

[201] L. Ponomarev. “Molecular structure effects on atomic and nuclear capture of mesons”. In: *Annual Review of Nuclear Science* 23.1 (1973).

[202] G.R. Burbidge and A.H. De Borde. “The mesonic auger effect”. In: *Physical Review* 89.1 (1953).

[203] A.H. De Borde. “The Auger Effect and Negative Meson Capture”. In: *Proceedings of the Physical Society. Section A* 67.1 (1954).

[204] D. Gotta et al. “X-ray transitions from antiprotonic noble gases”. In: *Eur. Phys. J. D.* 47.1 (2008).

[205] C.J. Batty. “Optical-model analysis of exotic atom data:(I). Kaonic atoms”. In: *Nucl. Phys. A* 372.3 (1981).

[206] C.J. Batty, E. Friedman, and A Gal. “Density-dependent p-nucleus optical potentials from global fits to p atom data”. In: *Nucl. Phys. A* 592.4 (1995), pp. 487–512.

[207] S. Wycech. “Optical potentials for the antiproton nucleus interactions”. In: *Nucl. Phys. A* 692 (2001).

[208] P.D. Barnes et al. “Strong-Interaction Effects in Antiprotonic Atoms”. In: *Phys. Rev. Lett.* 29.17 (1972).

[209] D. Rohmann et al. “Measurement of the 4f strong interaction level width in light antiprotonic atoms”. In: *Zeitschrift für Physik A Atomic Nuclei* 325.3 (1986).

[210] A. Trzcińska et al. “Neutron density distributions deduced from antiprotonic atoms”. In: *Phys. Rev. Lett.* 87.8 (2001).

[211] M. Wada and Y. Yamazaki. “Antiprotonic radioactive atom for nuclear structure studies”. In: *AIP Conference Proceedings*. Vol. 793. American Institute of Physics. 2005.

[212] S. Wycech. “Nuclear structure studies with low energy p”. In: *AIP Conference Proceedings*. Vol. 793. American Institute of Physics. (2005).

[213] Y. Kubota and Y. Ono. To be published. 2022.

[214] E. Fermi. *Nuclear Physics*. The University of Chicago Press, (1949).

[215] A.D. Fried Z .and Martin. “Center-of-mass effect on electromagnetic transition rates in mesic atoms”. In: *Nuovo Cimento (Italy) Divided into Nuovo Cimento A and Nuovo Cimento B* 10 (1963).

[216] V.R. Akylas and P. Vogel. “Muonic atom cascade program”. In: *Computer Physics Communications* 15.3-4 (1978).

[217] E. Clementi and D.-L._ Raimondi. “Atomic screening constants from SCF functions”. In: *The Journal of Chemical Physics* 38 (1963).

[218] E. Clementi, D.L. Raimondi, and William P. Reinhardt. “Atomic screening constants from SCF functions. II. Atoms with 37 to 86 electrons”. In: *The Journal of chemical physics* 47 (1967).

[219] T. Koike. *Cascade Calculations of Hadronic Atoms*. Workshop to discuss PUMA experiment, RCNP (2018).

[220] R. Schmidt et al. “Nucleon density in the nuclear periphery determined with antiprotonic x rays: Cadmium and tin isotopes”. In: *Phys. Rev. C* 67.4 (2003).

[221] R. Bacher et al. “Degree of ionization in antiprotonic noble gases”. In: *Phys. Rev. A.* 38.9 (1988).

[222] R. Engfer et al. “Charge-distribution parameters, isotope shifts, isomer shifts, and magnetic hyperfine constants from muonic atoms”. In: *Atomic data and nuclear data tables* 14.5-6 (1974).

[223] J. Dechargé and D. Gogny. “Hartree-Fock-Bogolyubov calculations with the D 1 effective interaction on spherical nuclei”. In: *Phys. Rev. C* 21.4 (1980).

[224] R. Seki. Personal communication with R. Seki.

[225] A. Rohatgi. *Web Plot Digitizer*. https://https://apps.automeris.io/.

[226] G. Fricke et al. “Atomic Data and Nucl”. In: *Data Tables* 60.2 (1995).

[227] J. Dobaczewski, H. Flocard, and J. Treiner. “Hartree-Fock-Bogolyubov description of nuclei near the neutron-drip line”. In: *Nuclear Physics A* 422.1 (1984).

[228] R. Schmidt. “Bestimmung der Nukleonendichte in der Kernperipherie mit antiprotonischen Atomen”. PhD thesis. Technische Universität München, 1999.

[229] F.J. Hartmann et al. “Nucleon density in the nuclear periphery determined with antiprotonic x rays: Calcium isotopes”. In: *Phys. Rev. C.* 65 (2001).

[230] A. Levitt. “Solutions of the multiconfiguration Dirac–Fock equations”. In: *Reviews in Mathematical Physics* 26 (2014).

[231] K. Bennaceur and J. Dobaczewski. “Coordinate-space solution of the Skyrme–Hartree–Fock–Bogolyubov equations within spherical symmetry. The program HFBRAD (v1. 00)”. In: *Computer physics communications* 168 (2005).

[232] T. H. R. Skyrme. “The effective nuclear potential”. In: *Nucl. Phys.* 9 (1958).

[233] M. Beiner et al. “Nuclear ground-state properties and self-consistent calculations with the Skyrme interaction:(I). Spherical description”. In: *Nucl. Phys. A* 238 (1975).

[234] E. Chabanat et al. “A Skyrme parametrization from subnuclear to neutron star densities Part II. Nuclei far from stabilities”. In: *Nucl. Phys. A* 635 (1998).

[235] P.-G. Reinhard and H. Flocard. “Nuclear effective forces and isotope shifts”. In: *Nucl. Phys. A* 584 (1995).

[236] N. Tajima et al. “Self-consistent calculation of charge radii of Pb isotopes”. In: *Nucl. Phys. A* 551 (1993).

[237] P. Lubiński et al. “Neutron halo in heavy nuclei from antiproton absorption”. In: *Phys. Rev. Lett.* 73.24 (1994).